IPP-Report

Max-Planck-Institut für Plasmaphysik

Prisiazhniuk, D.

Development and application of poloidal correlation reflectormetry to study turbulent structures in the ASDEX Upgrade tokamak

IPP 2018-09
Mai 2018

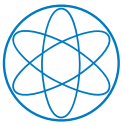

Technische Universität München

Max-Planck-Institut für Plasmaphysik

Development and application of poloidal correlation reflectometry to study turbulent structures in the ASDEX Upgrade tokamak

Dmitrii Prisiazhniuk

Vollständiger Abdruck der von der Fakultät für Physik der Technischen Universität München zur Erlangung der akademischen Grades eines

Doktors der Naturwissenschaften

genehmigten Dissertation.

Vorsitzender:	Prof. Dr. Frank Pollmann
Prüfer der Dissertation:	
	1. Prof. Dr. Ulrich Stroth
	2. Prof Dr. Bastian Märkisch

Die Dissertation wurde am 29.03.2017 bei der Technischen Universität München eingereicht und durch die Fakultät für Physik am 05.06.2017 angenommen.

DEPARTMENT OF PHYSICS

TECHNISCHE UNIVERSITÄT MÜNCHEN

Development and application of poloidal correlation reflectometry to study turbulent structures in the ASDEX Upgrade tokamak

Dmitrii Prisiazhniuk

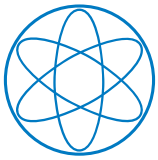

DEPARTMENT OF PHYSICS

TECHNISCHE UNIVERSITÄT MÜNCHEN

Development and application of poloidal correlation reflectometry to study turbulent structures in the ASDEX Upgrade tokamak

Author:	Dmitrii Prisiazhniuk
Supervisor:	Univ.-Prof. Dr. U. Stroth
Advisors:	Dr. A. Krämer-Flecken
	Dr. G. D. Conway
Submission Date:	29.03.2017

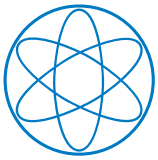

I confirm that this thesis is my own work and I have documented all sources and material used.

Munich, 29.03.2017 Dmitrii Prisiazhniuk

Abstract

One of the key question of high temperature plasma confinement in a magnetic field is how plasma turbulence influences the radial transport of particles and energy. A better understanding of transport processes caused by turbulence would allow to improve the plasma confinement in fusion devices. To this end a deeper understanding of the mechanisms controlling the development, saturation and stabilization of turbulence is needed. From the experimental point of view a main challenge in these investigations is the measurement of plasma parameters on both small temporal (μs) and spatial (mm) scales. In this thesis a new microwave heterodyne poloidal correlation reflectometry diagnostic has been developed and installed at the ASDEX Upgrade tokamak to investigate the cross-correlation of turbulent density fluctuations. This diagnostic yields information on fundamental turbulence parameters such as the perpendicular propagation velocity $v_\perp$, the perpendicular correlation length $l_\perp$ (characteristic size of the turbulent eddies) and the decorrelation time τ_d (characteristic life time of the turbulent eddies) over a wide range of plasma densities. The inclination of the turbulent eddies α in the poloidal-toroidal plane spanned by the magnetic flux surfaces of a tokamak, being a measure of the magnetic field pitch angle, can also be obtained. The turbulence investigations were performed in low confinement mode (L-mode) plasmas for a range of plasma parameters. All measurements were interpreted taking into account the transfer function of reflectometry in the Born approximation. The results are compared with theoretical predictions and simulations.

In the first part of this thesis the inclination and the propagation of turbulent structures are investigated. It is shown that eddies are nearly aligned to the magnetic field line and, therefore, the magnetic field pitch angle can be measured with a precision of about 1°. A small additional declination angle of turbulent structures of the order of $\approx$ 2–3° from the equilibrium magnetic field line is found at the pedestal position. The dispersion relation of propagating density fluctuations is found to be nearly linear between perpendicular wavenumbers $k_\perp = 1$ and 12 cm^{-1} in both the core and edge regions of the plasma. The propagation velocity $v_\perp = v_{E\times B} + v_{ph}$, composed of the background $E \times B$ drift and the intrinsic phase velocity of the turbulence, shows reasonable agreement with $v_{E\times B}$ calculated from neoclassical theory. The extracted turbulence phase velocity from the difference of the measured $v_\perp$ and the neoclassical estimate of $v_{E\times B}$ is significantly smaller than values predicted for linear electron drift

waves in the plasma edge region. This value of the measured phase velocity has been compared with a nonlinear turbulence simulation by the gyrofluid code GEMR, which is found to reproduce small phase velocity.
In the second part of the thesis, the relation between the turbulence structure, the mean plasma parameters and the $v_\perp$ velocity shear is investigated. The measured correlation length varies from 0.6 to 2.0 cm and the decorrelation time from 5 to 50 μs. It is shown that the perpendicular correlation length scales with the drift wave scale $\rho_s = \sqrt{m_i T_e}/eB$, while the decorrelation time is roughly $40/v_\perp$. Furthermore it is shown that an increase of the $v_\perp$ flow shear in the edge region results in an additional decrease of decorrelation time that is in agreement with theoretical expectations.
The last part of the thesis is devoted to the measurement of turbulence parameters between two different confinement regimes: the linear Ohmic confinement and the saturated Ohmic confinement. The perpendicular correlation length and decorrelation time do not change their dependence on plasma parameters between the two regimes. However, a quasi coherent fluctuation, as a feature of the linear Ohmic confinement is found and discussed in terms of a change in the main turbulence driving instability.

The characterization of turbulence structure in the edge of fusion plasma from this work can be used as basis of a detailed comparison with turbulence simulation codes in the future. This will help to test the physical models in these codes and to explain formation of the turbulence and the associated radial transport. To check for possible diagnostic effects, a synthetic PCR diagnostic (e.g. using the Born approximation) can be applied to simulated data in order to enable cross-comparisons of equivalent quantities.

Zusammenfassung

Eine Schlüsselfrage in der Fusionsforschung, basierend auf dem Einschluss des Plasmas durch Magnetfelder, ist die Frage wie die Turbulenz in Hochtemperaturplasmen den nach aussen gerichteten radialen Transport von Teilchen und Energie beeinflusst, was letzt endlich zu einer Verminderung der Energieeinschlusszeit führt. Daher ist ein grundlegendes Verständnis der Prozesse nötig, die zur Stabilisation und Kontrolle der Turbulenz führen. Um diese Frage aus Sicht des Experiments zu beantworten werden Messmethoden benötigt, die es erlauben die Plasmaparameter auf μs- und mm-Skalen zu beobachten. In der vorliegenden Arbeit wurde ein heterodynes Mikrowellen Korrelationsreflektometer am Tokamak ASDEX Upgrade aufgebaut und in Betrieb genommen. Mit dieser Diagnostik sollen kleinskalige Dichtefluktuationen im Plasma beobachtet werden. Die Diagnostik ist in der Lage die fundamentalen Plasmaparameter wie die Geschwindigkeit, die Korrelationslänge und die charakteristische Lebensdauer der Turbulenz über einen weiten radialen Bereich des Plasmas zu untersuchen. Zusätzlich ist durch die Antennenanordnung eine Vermessung des Steigungswinkels der Magnetfeldlinien im Plasma möglich. Die hier vorgestellten Untersuchungen wurden an Plasmen mit kurzer Energieeinschlusszeit, sogenannten L-Mode-Plasmen, durchgeführt. Für die Interpretation der Messungen wurde die Ausbreitung der Mikrowellen im Plasma mittels der Born-Näherung berücksichtigt. Die gewonnenen Ergebnisse werden zusammen mit theoretischen Vorhersagen und Simulationen diskutiert.

Im ersten Teil der Arbeit wird die Bewegung der Turbulenz auf Flussflächen untersucht. Es wird gezeigt, dass die turbulenten Wirbel im wesentlichen entlang der Magnetfeldlinien ausgerichtet sind. Kleinere Abweichungen im Bereich von 2–3° wurden im Bereich des Übergangs vom Plasmarand zum inneren Einschlussbereich beobachtet. Ein linearer Zusammenhang zwischen der Ausbreitung der Dichtefluktuationen im Zentrum als auch am Plasmarand und den Wellenzahlen im Bereich zwischen $k_\perp = 1$ und 12 cm^{-1} wurde festgestellt. Die Wirbel bewegen sich senkrecht zum Magnetfeld auf den magnetischen Flussflächen. Die Geschwindigkeit dieser Bewegung setzt sich aus zwei Komponenten zusammen, aus der $E \times B$ Geschwindigkeit des Plasmas und einer zusätzlichen Phasengeschwindigkeit der Turbulenz. Ein Vergleich mit der neoklassisch berechneten $E \times B$ Geschwindigkeit ist im Plasmazentrum deutet auf eine zu vernachlässigende Phasengeschwindigkeit hin. Am Plasmarand wurden Abweichungen zwischen den experimentellen Messungen und dem Modell von ≤ 0.5 km/s gefunden.

Die gemessene Phasengeschwindigkeit in dieser Region ist allerdings signifikant kleiner als die Vorhersagen für Elektronen-Driftwellen vermuten lassen.
Im zweiten Teil der Arbeit ist der Einfluss des Gradienten der $E \times B$ Geschwindigkeit, sogenannten $E \times B$-Verscherung, auf die Struktur der Turbulenz sowie die Plasmaparameter untersucht worden. Die für die Turbulenzstruktur wichtigen Grössen wie Korrelationslänge und Lebensdauer varrieren zwischen 0.6–2.0 cm und 5–50 μs. Es konnte gezeigt werden, dass die Korrelationslänge mit $\rho_s = \sqrt{m_i T_e}/eB$, der Skalenlänge von Driftwellen, korreliert. Für die Lebensdauer der Turbulenz konnte ein Zusammenhang mit der Geschwindigkeit festgestellt werden, der durch die Gleichung $\tau_{dc} \approx 40/v_\perp$ beschrieben werden kann. Weiter konnte gezeigt werden, dass eine Zunahme der $E \times B$-Verscherung eine Verminderung der Lebensdauer der Turbulenz bewirkt, was mit theoretischen Vorhersagen übereinstimmt.
Der letzte Teil der vorliegenden Arbeit untersucht die Rolle der Turbulenz im Übergang zweier Einschlussszenarien, den Bereich in dem die Energieeinschlusszeit linear mit der Elektronendichte (linear Ohmic confinement, LOC) anwächst und dem Bereich in dem die Energieeinschlusszeit unabhängig von der Elektronendichte in die Sättigung übergeht (saturated Ohmic confinement, SOC). Während des Übergangs wird die Änderung der Korrelationslänge und der Lebensdauer weiterhin durch die oben genannten Zusammenhänge beschrieben. Allerdings wurde eine sogenannte quasikohärente Turbulenzstruktur im LOC–Regime gefunden. Das Auftreten dieser Mode wurde im Zusammenhang mit die Turbulenz antreibenden Plasmainstabilitäten diskutiert.

Zusammenfassend kann gesagt werden, dass die in dieser Arbeit untersuchten Turbulenzeigenschaften für einen späteren Vergleich mit Turbulenzsimulationen herangezogen werden können. Damit ist man in der Lage, Modelle zur Turbulenzentwicklung zu testen, und mit den hier dargestellten Messungen zu vergleichen. Das führt letztendlich zu einem verbesserten und grundlegenderen Verständnis des radialen Transports auf Basis der Turbulenz im Plasma.

Contents

1 Introduction

In the next few decades a significant increase in the world energy consumption is expected due to economic development and population growth [1]. About 90 % of the current energy production relies on fossil fuels such as crude oil, natural gas and coal [2]. The use of fossil fuels leads to three main problems:

1. Short-term finite amount of resources. Reserves of oil, gas and coal were estimated in 2013 to 54, 55 and 115 years, respectively, at the current extraction rate [3].

2. Air pollution. Fossil fuels release CO_2, a greenhouse gas which induces an increase of the world's average temperature on a short timescale [4].

3. Geopolitical and social threats. The rising of the energy costs increases the tension between countries and the level of the poverty.

Thereby it is important to invest into new forms of energy production which are safe, environmentally friendly and inexhaustible. Nuclear fusion is one of the prospective approaches to produce the needed energy. The application of nuclear fusion on earth is based on the fusion of two hydrogen isotopes, deuterium (D) and tritium (T), to form a heavier nucleus (He),

$$^2\mathrm{D} + {}^3\mathrm{T} \rightarrow {}^4\mathrm{He}\,(3.5\ \mathrm{MeV}) + \mathrm{n}\,(14.1\ \mathrm{MeV}). \tag{1.1}$$

Following Einstein's law ($\Delta E = \Delta m c^2$) a decrease in the total mass due to the nuclear rearrangement leads to a release of energy. This energy is shared between a helium He (3.5 MeV) ion and a neutron n (14.1 MeV). The fusion probability cross-section of the D-T reaction is shown in figure 1.1a. A high cross-section is observed at temperatures around 20 keV. At these temperatures particles are fully ionized forming a thermalized plasma. To maximize the number of fusion reactions the D-T plasma has to be confined.

Lawson proposed a criterion for the ignition of the DT reaction [5], where the product of density n, temperature T and energy confinement time τ_E needs to be higher than $nT\tau_E > 3 \times 10^{21} [\mathrm{keV\,s/m^3}]$. Two methods have been proposed to confine D and T such that the criterion is fulfilled. The first one is inertial confinement where small and dense D-T ice pellets are homogeneously heated by lasers resulting in compression and fast

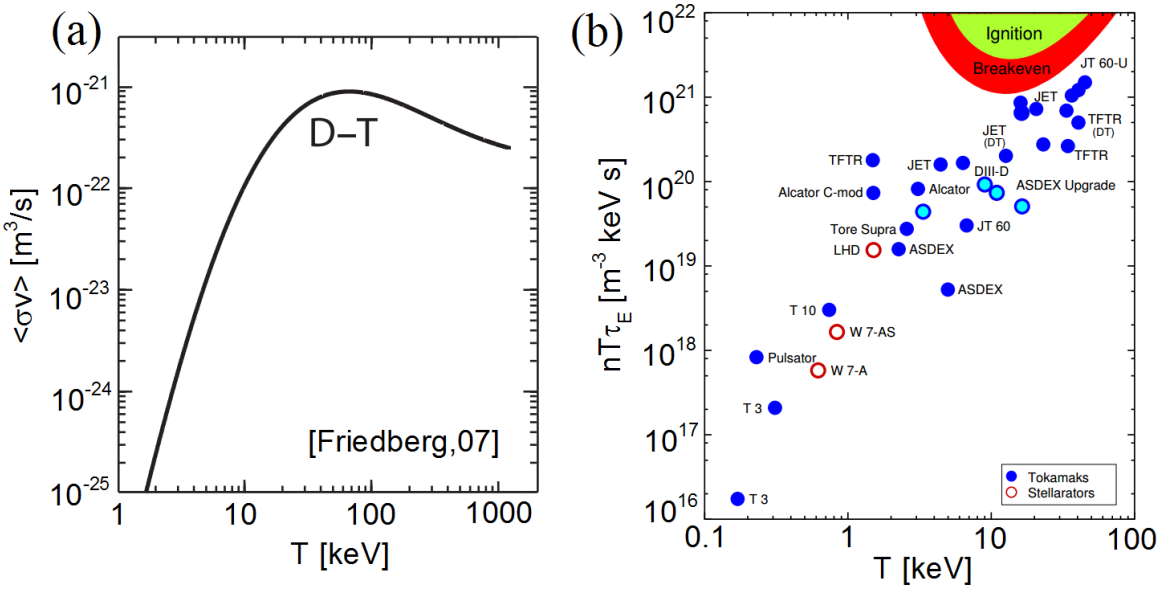

Figure 1.1: (a) The cross-section of the D-T reaction (adapted from [6]). (b) Triple product $nT\tau_E$ in different magnetic confinement experiments.

ignition. The confinement time for inertial fusion is determined by the time of flight of the heated pellet, which is very short. Therefore very high densities of the particles need to be used. The second method is magnetic confinement, where a plasma is confined by a magnetic field for relatively long time. Currently, magnetic confinement is the most promising technique to achieve nuclear fusion. Among the available magnetic confinement devices the most developed are tokamaks and stellarators. Figure 1.1b shows the triple product $nT\tau_E$ for different magnetic confinement experiments. The next generation tokamak ITER [7] is expected to demonstrate the possibility to produce a ten times return on invested energy (Q=10). To increase $nT\tau_E$ further, one has to understand how to control the transport processes of particles and energy in a tokamak.

1.1 Particle motion in the tokamaks

The tokamak (from Russian - "Toroidal chamber with magnetic coils") is a magnetic confinement device proposed by I. Tamm and A. Sakharov in 1950 [8]. Figure 1.2 shows a typical scheme of a tokamak with circular poloidal cross-section. The tokamak is characterized by two geometric quantities: (i) the major radius R is the distance of a point from the toroidal axis and (ii) the minor radius r is the the distance from the plasma centre (magnetic axis). The combination of an externally applied toroidal

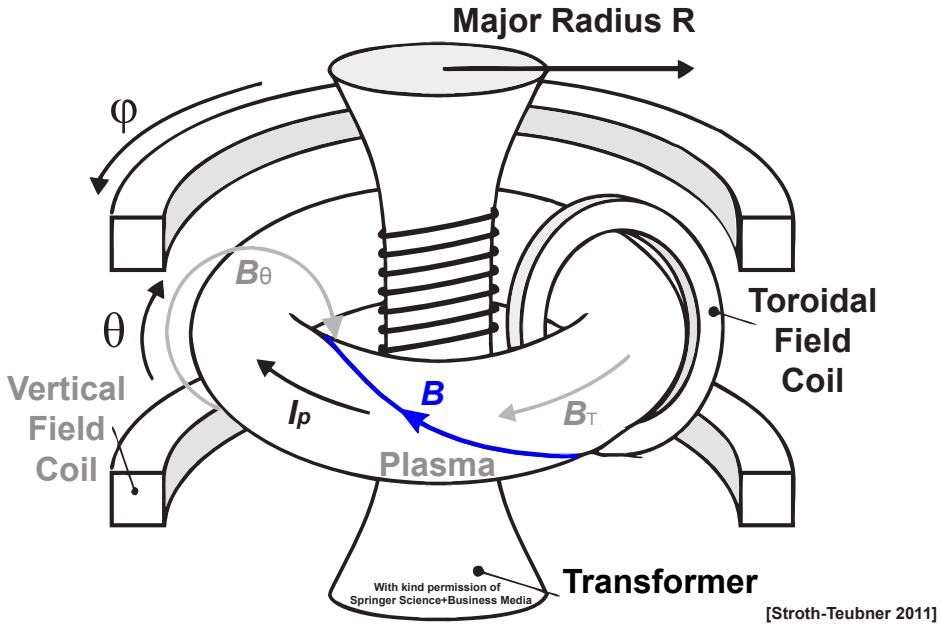

Figure 1.2: Schematic of the magnetic configuration in a tokamak. The combination of the externally applied toroidal magnetic field B_T and the poloidal magnetic field B_θ generated by the inductively driven plasma current I_p creates a helical magnetic field line structure (adapted from [9]).

magnetic field $B_T = B_{T0}R_0/R$ and a poloidal magnetic field B_θ generated by an inductively driven plasma current I_p creates a helical magnetic field line structure. Here B_{T0} is the toroidal magnetic field at the magnetic axis R_0 (see also figure 1.3). The slope of the magnetic field lines is called the magnetic field pitch angle defined as $\alpha = \arctan(B_\theta/B_T)$. A safety factor $q = m/n$ describes the geometry of magnetic field lines and is defined as the ratio of toroidal (m) to poloidal (n) turns of a field line before it close itself. In the case of a circular poloidal cross-section, the safety factor equals to $q = rB_T/R_0B_\theta$. The magnetic flux surface is formed by magnetic field lines twisted around the plasma. Such surfaces have a form of a torus preventing the escape of particles along magnetic field lines from the tokamak. The last closed flux surface is called the separatrix. The magnetic flux surfaces can be labelled with the normalized poloidal flux value ρ_{pol} defined as

$$\rho_{\text{pol}} = \sqrt{\frac{\Psi - \Psi_a}{\Psi_s - \Psi_a}}, \tag{1.2}$$

where $\rho_{\text{pol}} = 0$ on the magnetic axis and $\rho_{\text{pol}} = 1$ at the separatrix. Here Ψ is the magnetic poloidal flux, Ψ_a and Ψ_s the poloidal flux at the plasma axis and the separatrix, respectively. It is important to note that the shape of the surfaces must not

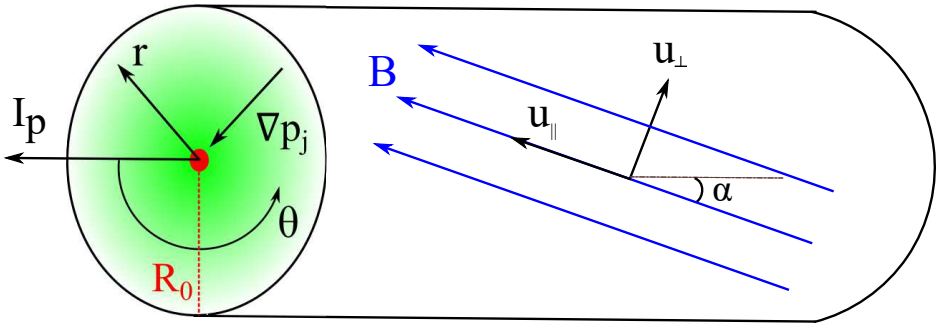

Figure 1.3: The gyro averaged particle motion consists of the fast parallel dynamics along magnetic field lines $u_{\parallel}$, the relatively slow drift perpendicular to the magnetic field lines $u_{\perp}$ and the motion perpendicular to the magnetic surfaces u_r.

necessary be circular (see figure 1.4).

Electrically charged particles in a magnetic field experience a fast circular motion around a magnetic field line with a cyclotron frequency equal to $\omega_{cj} = Z_j B/m_j$. Here Z_j denotes the charge and m_j the mass of the species j. In a plasma the gyro averaged motion can be treated as fluid velocity which has the following components

$$\vec{u} = \vec{u}_{\parallel} + \vec{u}_{\perp} + \vec{u}_r. \tag{1.3}$$

Here $\vec{u}_{\parallel}$ indicates the fast parallel dynamics along the magnetic field line, $\vec{u}_{\perp}$ the relatively slow drift on a flux surface but perpendicular to the magnetic field lines and $\vec{u}_r$ the motion perpendicular to the magnetic surfaces (see figure 1.3). The perpendicular fluid velocity $\vec{u}_{\perp}$ consists of the $\vec{E} \times \vec{B}$ drift velocity and the diamagnetic velocity

$$\vec{u}_{\perp j} = \frac{\vec{E} \times \vec{B}}{B^2} - \frac{\nabla p_j \times \vec{B}}{n_j Z_j B^2} = \vec{v}_{E\times B} + \vec{v}_{dj}, \tag{1.4}$$

where $\vec{E}$ is the radial electric field, p_j the pressure and n_j the density of species j. In this expression the contribution of turbulence driven flows [10] is neglected. While $u_{\parallel}$ and $u_{\perp}$ do not explicitly affect the particle confinement, u_r is responsible for their radial transport. The value of u_r determines the energy confinement time τ_E and therefore the related physics is very important. One obvious mechanism for radial transport are Coulomb collisions between electrons and ions. This can be described as a random diffusion process with a diffusion coefficient D_{cl}

$$u_r^{\mathrm{cl}} = D_{\mathrm{cl}} \frac{1}{n} \frac{\mathrm{d}n}{\mathrm{d}r} = \rho_L^2 \nu_{ei} \frac{1}{n} \frac{\mathrm{d}n}{\mathrm{d}r}. \tag{1.5}$$

Here the larmor radius of the particles ρ_L is the characteristic step length, and the inverse of the collision frequency ν_{ei}^{-1} is the characteristic step time of the diffusion

process. Such a type of transport is called classical. In tokamaks the collisional transport is modified due to the effects of the inhomogeneous magnetic field $B(\vec{r})$. The magnetic field is not constant along magnetic field line $\nabla B_{\parallel} \neq 0$ and can trap particles in magnetic mirrors. Collisions on the other hand act as a detrapping mechanism. The collision frequency normalized to the effective bounce frequency

$$\nu_* = \frac{\nu_{ei}}{2\epsilon\omega_b} = \frac{\nu_{ei} q R}{\epsilon^{3/2} v_{th}} \tag{1.6}$$

can be used as parameter characterizing different transport regimes. Here $\epsilon = r/R$ is the inverse aspect ratio, ω_b the bounce frequency of trapped particles and v_{th} the thermal velocity of the particles. The derivation of the diffusion coefficient at different values of ν_* can be found in reference [9]. This transport mechanism is called neoclassical and is usually higher compared to purely classical transport. The experimentally measured transport, however, is significantly higher due to the presence of turbulence.

1.2 Plasma Turbulence

The plasma measurements show fluctuations in all statistical parameters, such as density δn, temperature δT, electric potential $\delta\phi$ and magnetic field $\delta\vec{B}$. The fluctuations cover a broad frequency range (from several hundred Hz to several MHz) and exist due to the

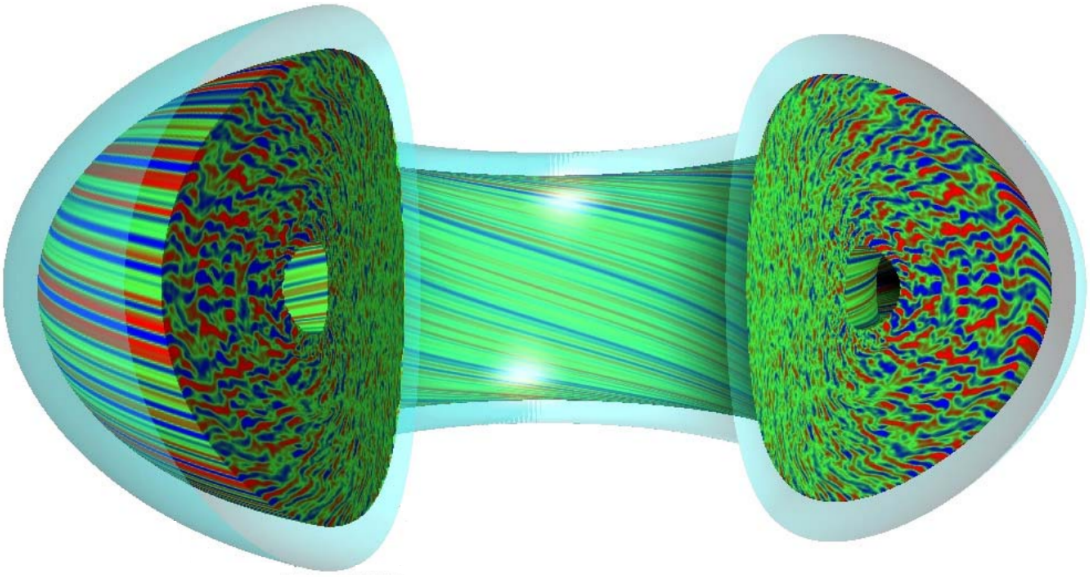

Figure 1.4: Simulation of the turbulence state of a plasma with the GYRO code. The colors represent density fluctuations amplitude (adapted from [14]).

transition of the plasma to a turbulent state. From the transport point of view, the small irregular structures (or turbulent eddies) in the plasma significantly enhance the radial transport by at least one order of magnitude compared to neoclassical transport [11, 12] and thus the understanding of their nature and properties is of crucial importance.

Although turbulent transport is currently not fully understood, it is clear that it affects the performance of the fusion devices and it remains one of the most complex problems in plasma physics. Nowadays, with the development of computer power and turbulence modelling codes, broadband turbulent fluctuations in plasma can be simulated. Many different codes are used, among which are GYRO [13, 14], GENE [15], ELMfire [16], GEMR [17, 18]. In figure 1.4 a snapshot of the density fluctuations from the GYRO code is shown for one time point. The irregular dependence of density on the poloidal angle is also clearly visible. Furthermore, the distribution changes with time. Although existing codes are able to predict fluctuations qualitatively, there is a difference between experimental measurements and simulations. A close comparison between turbulence models and sophisticated turbulence measurements are currently being undertaken to solve this disagreement.

1.3 L-mode vs H-mode

The plasma in a tokamak shows different confinement regimes: the low confinement mode (L-mode) and the high confinement mode (H-mode) [19]. The regimes differ by their energy confinement time τ_E, which in H-mode is about a factor of two higher compared to that in L-mode. This is favorable for a reactor. The transition from

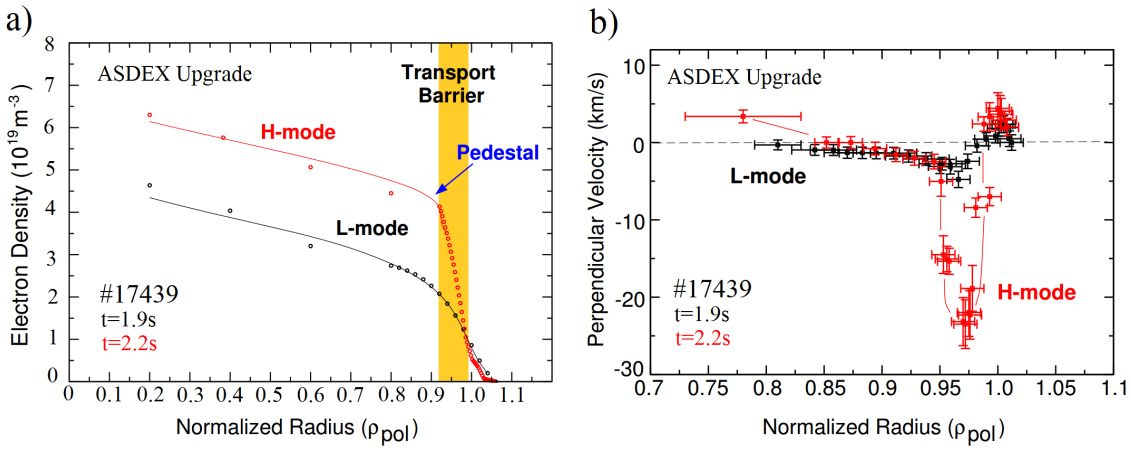

Figure 1.5: The electron density profiles (a) and the radial electric field (b) for L-mode (black) and H-mode plasma (red) (adapted from [22]).

L-mode to H-mode is observed for a heating power above some threshold, $P > P_{th}$, which depends on the plasma density n, the magnetic field B_T and the plasma surface area S [20, 21]. In the H-mode an edge transport barrier (ETB) is formed where the radial transport of particles and energy is significantly reduced compared to L-mode (figure 1.5a). The ETB is characterized by steep gradients in the density n, temperatures T_e and T_i (electrons and main ions) and a strong $v_{E\times B}$ shear flow at the edge of the plasma. The turbulence level in the ETB is suppressed [23]. The suppression of the turbulence and the formation of the ETB is still not fully understood, however, it is believed to be connected with the $v_{E\times B}$ shear flow in the edge of the plasma due to a strong localized radial electric field. The measurement of the $v_{E\times B}$ flow in L-mode (black) and in H-mode (red) are shown in figure 1.5b. The measurements were obtained using a Doppler reflectometry diagnostic [22] in the ASDEX Upgrade tokamak.

1.4 Thesis goals and outline

This thesis was carried out on the tokamak devices ASDEX Upgrade (AUG) located at the Max-Planck-Institute for Plasma Physics, and TEXTOR located at Research centre of Jülich in Germany. To address the spatio-temporal properties of the turbulent density fluctuations in L-mode of AUG, a new Poloidal Correlation Reflectometry (PCR) diagnostic has been developed and installed within the framework of this thesis. The diagnostic measures density fluctuations δn at 4 positions separated by small distances in the poloidal and toroidal plane. Cross correlation of the measured density fluctuations yields information on the turbulent eddy characteristics, such as the perpendicular propagation velocity $v_\perp$, the perpendicular correlation length $l_\perp$ (characteristic size of the turbulent eddy) and the decorrelation time τ_d (characteristic life time of the turbulent eddy) over a wide range of densities ($0.9 - 4.1 \times 10^{19}$ m^{-3}). Moreover, assuming that the turbulent eddies are aligned along the magnetic field line, the magnetic field pitch angle α can be obtained. The following main goals are addressed in this thesis:

1. Development and installation of the PCR diagnostic at AUG. The investigation of transfer function of reflectometry in Born approximation. The development of algorithms for the evaluation of $v_\perp$, $l_\perp$, τ_d and α using cross-correlation and spectral coherence analysis of the density fluctuations.

2. The investigation of the perpendicular propagation velocity of the turbulence (composed of the $E \times B$ drift and the intrinsic phase velocity of turbulence $v_\perp = v_{E\times B} + v_{ph}$) in the core and at the edge of AUG. The comparison of the measured velocity with neoclassical estimate of the $v_{E\times B}$ and with turbulence simulations of phase velocity v_{ph} from the GEMR code.

3. The investigation of the alignment of turbulent eddies in the direction of the magnetic field line at TEXTOR and AUG. The investigation of the possibility to measure the magnetic field pitch angle α from the inclination of turbulent structures and the evaluation of the precision of the method.

4. The measurement of a relation between perpendicular correlation length $l_\perp$ and decorrelation time τ_d of the eddies with mean plasma parameters at AUG. The investigation of an effect of the shear flow on $l_\perp$ and τ_d.

5. The investigation of changes in the turbulence properties between Linear Ohmic Confinement (LOC) and Saturated Ohmic Confinement (SOC) regimes at AUG.

The thesis is structured as follows: In chapter 2, an introduction to plasma turbulence is given. The properties of turbulent eddies and their interaction with sheared $v_{E\times B}$ flows is discussed. Chapter 3 describes the TEXTOR and AUG tokamaks and presents relevant diagnostics used in this work. Chapter 4 explains the principles of the reflectometry diagnostics, while in chapter 5 the new multi-antenna PCR system installed at AUG is presented. The assessment of the system is also shown in this chapter. Chapter 6 presents the data analysis methods used in the thesis. Chapter 7 is devoted to the study of the perpendicular velocity $v_\perp$ and the pitch angle α profiles using the time delay technique of the eddies. The measured phase velocity $v_{ph}(k_\perp)$, from the difference of the measured $v_\perp$ and the neoclassical estimate of the $v_{E\times B}$, is compared with predictions from the turbulence code GEMR and the α profile is compared with equilibrium reconstructions. In chapter 8 the measurement of the perpendicular correlation length $l_\perp$ and the decorrelation time τ_d of the eddies is presented. Chapter 9 is devoted to the study of turbulence properties in two different confinement regimes: the Linear Ohmic Confinement (LOC) and the Saturated Ohmic Confinement (SOC). Here, a quasi coherent fluctuation, as a feature of the LOC are discussed. The last chapter summarizes the results and presents an outlook for future applications of the method.

2 Turbulence

Plasma turbulence causes fluctuations in the fluid density and velocity and therefore has an influence on the radial transport of particles and energy. In this chapter, plasma turbulence is introduced and the properties of the turbulent eddies are described. In this context it is important to discuss (i) how instabilities, driven by gradients of mean plasma parameters, can trigger the turbulent state and (ii) how shear flows can suppress turbulent eddies.

2.1 Fully developed turbulence

Turbulence can exists in any fluid when a fluid is subject to external forces. Qualitatively, the transition to a turbulent state can be shown in an incompressible ($\nabla \cdot \vec{u} = 0$) neutral fluid by the Navier-Stokes equation

$$mn\left(\frac{\partial \vec{u}}{\partial t} + (\vec{u}\cdot\nabla)\,\vec{u}\right) = -\nabla p + \mu\Delta\vec{u}. \tag{2.1}$$

Here mn is the mass density, $\vec{u}$ the velocity field, p the pressure and μ the viscosity of the fluid. A dimensionless equation can be obtained using l_0 the characteristic scale of the system, u_0 the characteristic velocity and $t_0 = l_0/u_0$ the characteristic time. Redefining derivatives $\nabla_n = l_0\nabla$ and $\partial/\partial t_n = t_0\partial/\partial t$ one obtains

$$\frac{\partial \vec{u}_n}{\partial t_n} + (\vec{u}_n\cdot\nabla_n)\vec{u}_n = -\nabla_n p_n + \frac{1}{Re}\Delta_n\vec{u}_n, \tag{2.2}$$

where $\vec{u}_n = \vec{u}/u_0$, $\vec{t}_n = \vec{t}/t_0$ and $p_n = p/mnu_0^2$. The Reynolds number Re is given by

$$Re = \frac{u_0 l_0 mn}{\mu}, \tag{2.3}$$

which is the ratio of the non-linear force (second term of equation 2.1) to the viscous damping force of the system (last term of equation 2.1). Two different systems have the same solution if their Reynolds number is the same.

The behaviour of the flow at different Reynolds numbers can be shown using a fluid running through obstacles of size l_0. At very low number $Re \ll 1$ (figure 2.1a), the flow

is laminar. Any perturbation of the flow is suppressed because of the high friction. An "intermediate" Reynolds number $Re \sim 1$ (figure 2.1b) causes the formation of eddies or Karman vortex streets [24]. These structures appear due to the instability of the flow, when even small forces perpendicular to the flow yield deviations from the flow's straight path, forming eddy structures [25]. This new unstable flow takes a part of energy from the original flow. A fully developed turbulence state appears at very high Reynolds numbers $Re \gg 1$ (figure 2.1c), as superposition of motions at different scales.

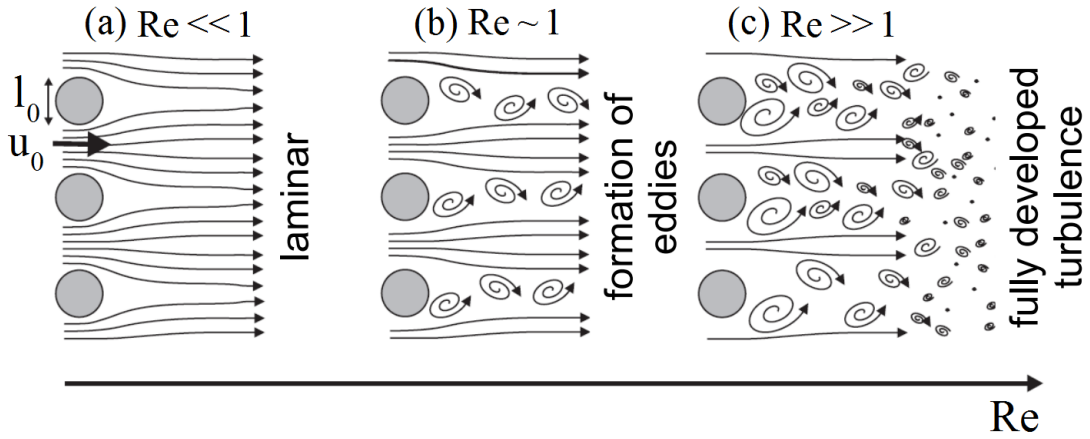

Figure 2.1: Behavior of a flow at different Reynolds numbers (adapted from [9]).

Although this simple picture can characterize the flow behavior, unfortunately it cannot be directly applied to turbulence in fusion plasmas. First of all, fusion plasmas have at least two fluids simultaneously, electrons and ions. Second, the plasma is formed by charged particles, hence electric $\vec{E}$ and magnetic $\vec{B}$ fields, which are generated by the electron and ion fluids, can act back on the fluids. This results in a complex interaction which can generate several types of instabilities. These instabilities lead to a turbulent state of the plasma. Simulations of such a system are computationally extremely demanding, and rely on several approximations. The validation of these approximations can only be made by cross comparing the spectral behavior of the turbulence from the simulations with those from experiments.

2.2 The energy wavenumber spectrum of the eddies

A typical turbulent system transfers energy from an injected instability towards different scales. The kinetic energy of the turbulent fluctuations is defined as

$$\frac{1}{2}\overline{\delta u^2} = \int E(k)\mathrm{d}k, \tag{2.4}$$

where δu is the fluctuation of fluid velocity and k the wavenumber of the fluctuations. An important question is how the turbulence energy $E(k)$ distributes across different scales.

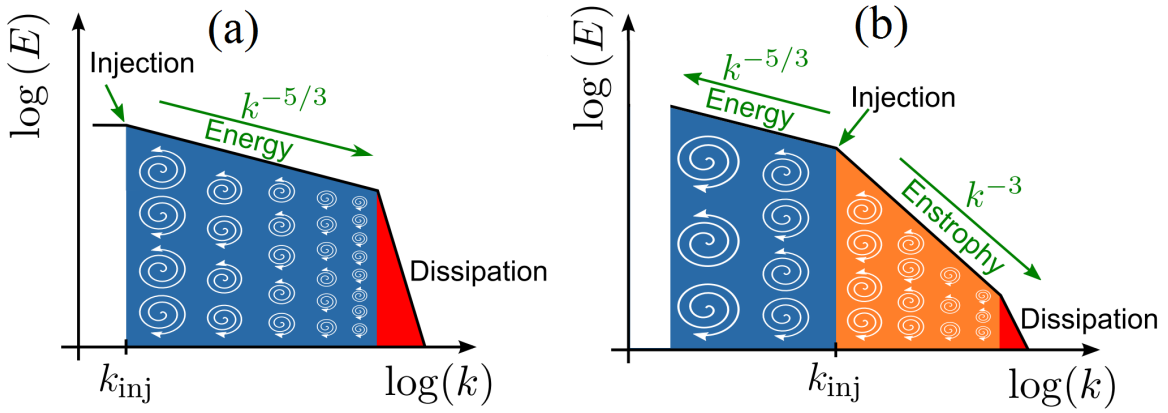

Figure 2.2: The spectral energy per unit wavenumber for (a) 3D turbulence and (b) 2D turbulence (adapted from [26]).

In the case of isotropic 3D turbulence only an energy transfer from big structures towards small structures exists. This is called the direct cascade. In 1941 Kolmogorov published a theory (K41-theory) in which he derived an equation for the spectral energy per unit wavenumber

$$E(k) \sim k^{-5/3}, k > k_{\mathrm{inj}}. \tag{2.5}$$

Here k_{inj} is the wavenumber of the injecting instability. The spectral index $-5/3$ has been confirmed by measurements in fluids [27]. However, the shape of the spectrum depends on the dimension. Transport in fusion devices along a magnetic field line is much faster compared to the slow drifts perpendicular to the magnetic field. This generates anisotropic 2D turbulent structures (see figure 1.4) instead of isotropic 3D structures. This changes the picture totally. The 2D turbulence case has been considered by Krainchan [28]. Two different cascades have been found: a direct cascade from the injection scale k_{inj} towards smaller structures, and an inverse cascade from the injection scale k_{inj} towards larger structures. The spectral energy per unit wavenumber can be described as

$$E(k) \sim \begin{cases} k^{-5/3}, k < k_{\mathrm{inj}} \\ k^{-3}, k > k_{\mathrm{inj}}. \end{cases} \tag{2.6}$$

This dependence is shown in figure 2.2b. Note that from the knee point of the spectrum ($k = k_{\mathrm{inj}}$) the injection scale of the underlying instability can be obtained. In real plasmas the situation is even more complex, since several injection scales can coexist

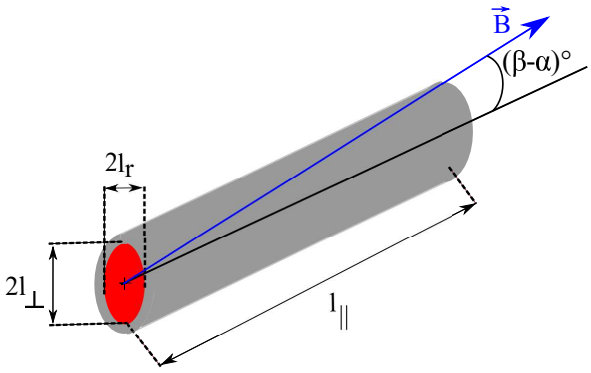

Figure 2.3: A typical turbulent eddy with parallel $l_{\|}$, perpendicular $l_{\perp}$ and radial l_r correlation lengths. The eddy is aligned along the magnetic field line, but may have an additional tilting due to a finite value of $l_{\|}$.

simultaneously. This will modify the spectral indexes and can give rise to several knee points, simultaneously. Several studies of the energy spectra using density fluctuations in low temperature plasmas of a stellarator [29, 30] and high temperature plasmas of a stellarator [31] and tokamaks [32, 33] have been performed.

2.3 The statistical parameters of turbulent eddies

In fusion plasmas, the fast transport along the magnetic field line and the slow drift perpendicular to $\vec{B}$ form an anisotropic turbulent eddy structure. Eddies have all possible sizes, however statistically, three characteristic sizes can be defined, such as (i) the parallel correlation length $l_{\|}$, (ii) the perpendicular correlation length $l_{\perp}$ and (iii) the radial correlation length l_r. Due to the anisotropy usually it is assumed that $l_{\|} \gg l_r, l_{\perp}$ (see figure 2.3). Beside the sizes, the decorrelation time τ_d can be defined as the characteristic life time of the turbulent eddies. The definition of these parameters used in this thesis are given in chapter 6. Assuming that the radial transport is determined by convection around the turbulent eddies [34, 35, 36], a simple diffusion coefficent can be estimated using these parameters

$$D_t = \frac{l_r^2}{\tau_d}. \tag{2.7}$$

The problem of course is that one does not know how to evaluate l_r and τ_d in fusion plasmas. Using linear theory in a cylinder, l_r can be approximated by $l_r \approx l_{\perp} \sim \rho_s$ and $\tau_d \sim L_n/c_s$ (Here $\rho_s = \sqrt{m_i T_e}/eB$ is the drift wave scale, L_n the density scale length and c_s the sound speed). This gives the so-called gyro-Bohm like scaling of the diffusion

coefficient $D_{gb} \sim \rho_s^2 c_s / L_n$ for drift wave turbulence [35, 37]. However, the estimation provided by the linear theory is often incorrect in the case of fully developed turbulence. The measurement and understanding of the turbulent scale and the associated transport is important for the prediction of future devices such as ITER and DEMO.

2.3.1 The alignment of turbulent eddies with the magnetic field line

The turbulent eddies are strongly aligned with the static magnetic field line $\vec{B}$. However, an additional inclination angle $(\beta - \alpha)$ with respect to $\vec{B}$ (see figure 2.3) can appear due to a finite value of $l_{\|}$, which can be estimated roughly by [38]

$$l_{\|} = \frac{2\pi q R}{m - nq}, \tag{2.8}$$

where m and n are the poloidal and toroidal mode numbers of the turbulent structures and $q = rB_T / R_0 B_\theta$ is the local safety factor. This equation can be rewritten using the local magnetic field pitch angle $\tan(\alpha) = B_\theta / B_T$ and the inclination angle of the turbulent structure $\tan(\beta) = rn/Rm$

$$\tan(\beta) = \tan(\alpha) + \frac{2\pi}{l_{||} k_\theta}. \tag{2.9}$$

Here we introduced the poloidal wavenumber of the turbulent structures as $k_\theta = m/r$. This equation defines the declination $(\beta - \alpha)$ of turbulent structures from the magnetic field line. It coincides with the equation obtained by Mahdizadeh [39].

Assuming $k_\theta \approx 0.5$–10 cm^{-1} the declination is expected to be $< 1^\circ$ if $l_{\|} > 10$ m. Only a few publications report on measurements of the parallel correlation length [39, 40, 41, 42] with values between 4 and 40 m reported. Recent parallel correlation length measurements from the TEXTOR tokamak give values between 11 and 22 m [43] indicating that the eddies are well aligned to the magnetic field line at TEXTOR. Conversely, if both (i) the real magnetic field pitch angle α (e.g. from magnetic equilibrium reconstruction) and (ii) the inclination of turbulent structures β can be determined simultaneously then the turbulence parallel correlation length could be obtained according to equation 2.9.

2.4 Turbulence drive - plasma instabilities

To maximize fusion power $P_{fus} \sim n^2 T$, plasmas are very hot and dense in the core. To prevent damage of wall, plasmas are cold and sparse at the edge. This creates gradients

in plasma parameters (see figure 2.4), which are responsible for the development of instabilities acting as an energy source for the plasma turbulence. Instabilities differ by their typical scales and by the local relationships between the different quantities. It was shown in [44], that the properties of the linear instabilities are also partially present in the state of fully developed turbulence. Therefore it is important to give a short overview on the instability properties in the linear phase.

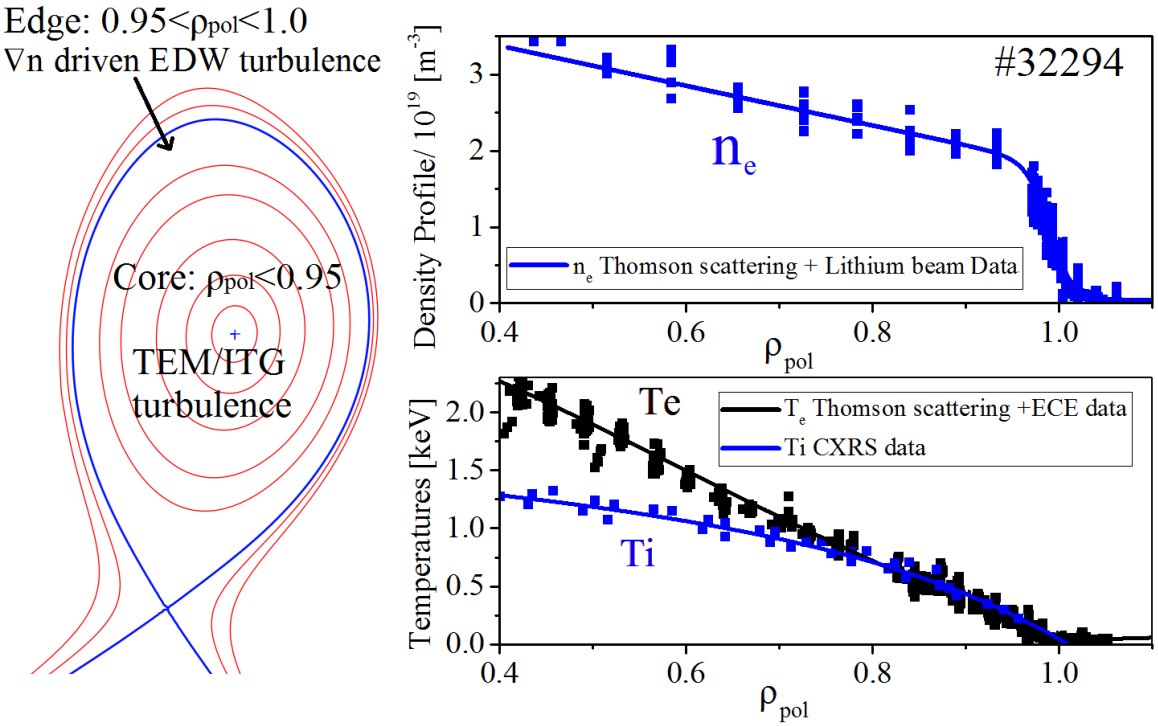

Figure 2.4: Unstable modes in different regions of the AUG plasma

The destabilization of specific modes depends on the local plasma parameters. Figure 2.4 shows an example of density (n), electron temperature (T_e) and ion temperature (T_i) profiles from the L-mode AUG discharge #32294. The radial gradients lead to different unstable modes coexisting at different positions in the plasma. The following quantities are used to characterize the linear instabilities:

1. The normalized logarithmic density gradient $R/L_n = -R\nabla \log(n)$ and normalized logarithmic temperature gradients $R/L_{Te,i} = -R\nabla \log(T_{e,i})$.

2. The normalized scale of an instability $k_\perp \rho_s$, where $\rho_s = (m_i T_e)^{1/2}/eB$ is the drift wave scale.

3. The phase velocity of the mode $v_{ph}(k_\perp) = \omega(k_\perp)/k_\perp$.

The *edge region* of the plasma ($0.95 < \rho_{\text{pol}} < 1$) is dominated by electron drift waves (EDW) driven by the density gradient $\nabla \log(n)/\nabla \log(T_{e,i}) \gtrsim 2$ present in this region [45, 46, 47, 48]. The growth rate has a maximum around $k_\perp \rho_s = 1$. The standard EDW propagates in the electron diamagnetic direction with a phase velocity equal to

$$v_{ph}(k_\perp) = \frac{v_{de}}{1 + k_\perp^2 \rho_s^2}, \tag{2.10}$$

where $v_{de} = \nabla p_e / enB$ is electron diamagnetic drift velocity. The value of v_{ph} is comparable to v_{de} at low $k_\perp \rho_s \ll 1$, but it is equal to only $0.1 v_{de}$ at $k_\perp \rho_s = 3$. The value of v_{ph} at low $k_\perp$ would be comparable to the $E \times B$ drift velocity in the edge region (see section 2.6).

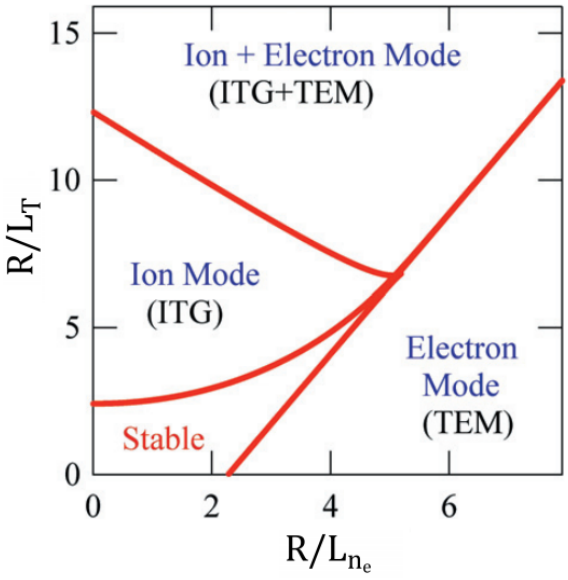

Figure 2.5: The stability diagram of ITG and TEM for $T_i = T_e$ (adapted from [49]).

In the *core region* of plasma ($\rho_{\text{pol}} < 0.95$), where usually $\nabla \log(T_{e,i})/\nabla \log(n) > 1$, two types of modes can exist: (i) trapped electron modes (TEM) driven by the electron temperature gradient R/L_{T_e} and (ii) ion temperature gradient (ITG) modes driven by the ion temperature gradient R/L_{T_i}. The stability diagram of these modes for $T_i = T_e$ is shown in figure 2.5.

ITG modes (also called η_i modes) are usually the most important ones in the plasma core [50]. They are driven by R/L_{Ti} and stabilized by R/L_n. ITG modes are also sensitive to the effective charge Z_{eff} and stabilized with increasing Z_{eff} due to a decrease of the main ion content in the plasma. ITG modes have typical scales of about

$k_\perp \rho_s \approx 0.3$. Numerical simulations indicate that the dispersion relation is linear with a phase velocity of $v_{ph} \approx 3\rho_s c_s / R$ oriented in the ion diamagnetic direction [37, 52].

TEM modes develop in tokamaks due to the presence of trapped particles [51]. They are driven by R/L_{Te} and by R/L_n. The typical scale of TEM modes is similar to that of ITG, $k_\perp \rho_s = 0.3$. The important property of TEM modes is that they can be damped by collisions due to de-trapping of the trapped particles. Numerical simulations show that the TEM phase velocity is of the order of 100–1000 m/s and is oriented in the electron diamagnetic direction [52, 53].

Both ITG and TEM modes show a linear dispersion relation with phase velocities significantly lower than those of the EDW. A short summary of the properties of the instabilities in the linear phase is given in table 2.1.

Properties	EDW	TEM	ITG
v_{ph} direction	Electron direction	Electron direction	Ion direction.
Dispersion	nonlinear	linear	linear
$k_\perp \rho_s$	~ 1	~ 0.3	~ 0.3
Driving	R/L_n	R/L_{T_e}, R/L_n	R/L_{T_i}
Stabilizing	-	ν_{ei}	R/L_n, Z_{eff}

Table 2.1: The properties of instabilities in their linear phase.

2.5 Turbulence suppression by shear flows

The transition to H-mode can be explained by turbulence suppression. The first analytic model of turbulence suppression by $E \times B$ shear flows has been proposed by Biglari et al. in 1990 [54]. An illustration of the model is shown in figure 2.6. When an eddy is placed into a $E \times B$ flow without any gradient $\partial v_{E\times B}/\partial r = 0$, the eddy is simply transported without distortion. In this case the eddy is isotropic in the perpendicular-radial plane with a radial correlation length comparable to perpendicular one $l_r \approx l_\perp$ (figure 2.6a). If a weak shear $\partial v_{E\times B}/\partial r \neq 0$ is added, then the eddy is stretched along the direction of $v_{E\times B}$. In this case the eddy becomes anisotropic with a radial correlation length smaller than the perpendicular one $l_r < l_\perp$ (figure 2.6b). If the shear exceeds a critical value (strong shear), the eddy is torn apart, reducing its radial correlation length (figure 2.6c). This reduces the radial transport because the transport is determined by convection of particles around the eddies (see equation 2.7). The value of the critical shear is given

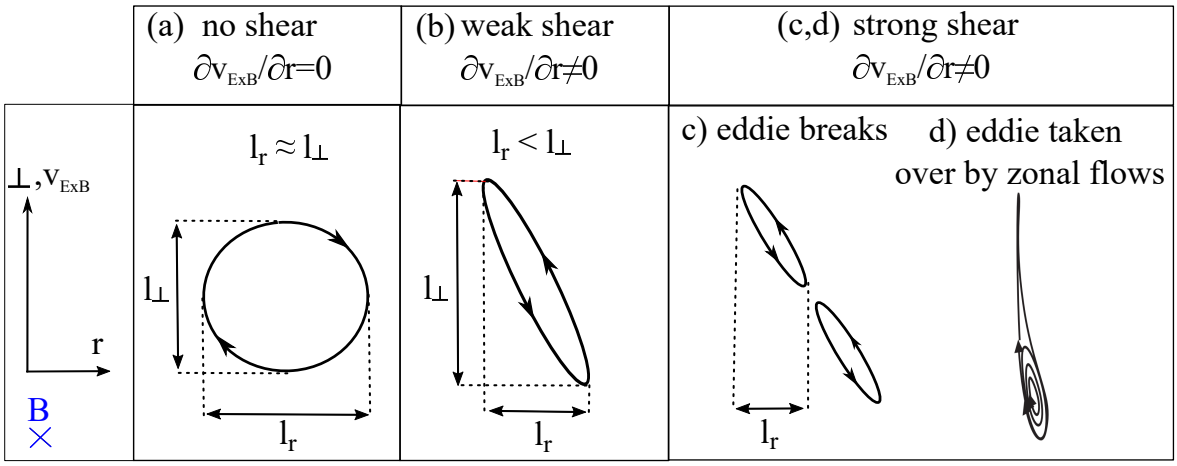

Figure 2.6: The turbulent eddie is placed into field (a) without shear flow, (b) weak shear flow and (c, d) strong shear flow.

by [54]

$$\tau_s^{-1} \equiv (k_\perp l_r) \frac{\partial v_{E\times B}}{\partial r} > \tau_d^{-1}, \tag{2.11}$$

where τ_s is the shear strain time, τ_d the decorrelation time and $k_\perp$ the perpendicular wavenumber of the turbulent structure. The role of a stable shear flow in suppressing turbulence is also discussed in [10].

The Biglari model only causes a redistribution of the energy to smaller scales. An alternative mechanism for the reduction of turbulent energy has been proposed in [55, 56]. In this model the eddy in a strong shear environment is not destroyed, but elongated and convolutes into a larger zonal flow (figure 2.6d). Zonal flows are low frequency (up to some kHz) $n = m = 0$ electrostatic fluctuations localized in a narrow region in the plasma. Zonal flows do not contribute to radial transport and thus can be a reason for a reduction of turbulence transport.

2.6 Measurement of the radial electric field in AUG

The radial electric field in the plasma is determined by the radial force balance [10, 55]

$$E_r = \frac{1}{Z_j n_j} \nabla p_j - u_{\theta j} B_T + u_{Tj} B_\theta, \tag{2.12}$$

where Z_j is the charge, p_j the pressure, $u_{\theta j}$ and u_{Tj} the poloidal and toroidal velocities for the species j.

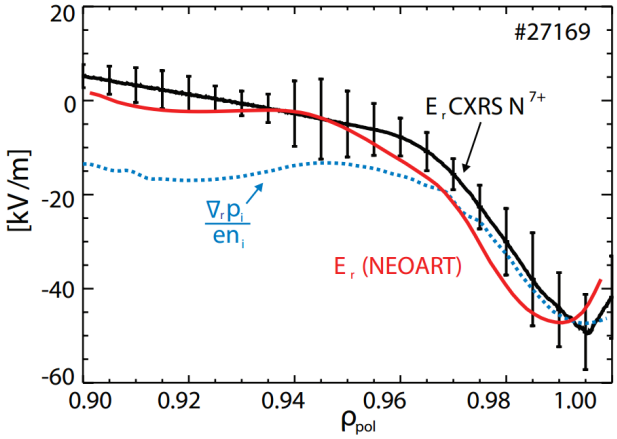

Figure 2.7: CXRS measurements of the radial electric field (adapted from [57]).

The radial electric field has been investigated at AUG in H-mode plasmas and at the transition from L to H-mode [57, 58, 59] using charge exchange recombination spectroscopy (CXRS) diagnostic. CXRS calculates E_r from the measurement of all components of equation 2.12 for an ion species j. The measurement of E_r (black curve) during H-mode where the turbulence level is low is shown in figure 2.7. Close to the edge $\rho_{\mathrm{pol}} > 0.95$ the main ion poloidal and toroidal velocity are close to zero. In this case the radial electric field derived from neoclassical theory can be approximated by the main ion pressure gradient in the form (blue curve in figure 2.7)

$$E_r \approx \frac{\nabla p_i}{en} \tag{2.13}$$

At $\rho_{\mathrm{pol}} < 0.95$, however, equation 2.13 is no longer satisfied due to influence of the main ion toroidal rotation. The full neoclassic model NEOART [60] has been used to take into account the toroidal rotation. This model uses the measurement of toroidal rotation by CXRS and calculates the neoclassical poloidal rotation from equations described in [61]. The comparison of the predicted E_r by NEOART (red curve) with the measured by CXRS (black curve) is shown in figure 2.7.

In addition to the equilibrium radial electric field accounted by neoclassical theory, a turbulence driven zonal flow contribution can be expected. As shown in figure 2.7, this contribution is small in the H-mode plasma edge of AUG. Their contribution in L-mode is still under discussion.

3 Experimental setup

This chapter presents the tokamaks TEXTOR and ASDEX Upgrade. Relevant diagnostics for this work are introduced. The typical discharge waveforms for L-mode plasmas used in the experiment are shown as well.

3.1 TEXTOR and ASDEX Upgrade

TEXTOR (Torus Experiment for Technology Oriented Research) [63] was a middle sized tokamak located at Research centre Jülich in Germany[1]. The main geometry and plasma parameters of TEXTOR are listed in table 3.1. TEXTOR had a circular poloidal cross-section as shown in figure 3.1a. The plasma was limited by a full toroidal belt limiter mounted 45° below the equatorial plane. The limiter at $r = a$ (dashed line) separates the plasma volume into two regions, the core region $r < a$ where the plasma is confined and the scrape-off layer (SOL) region $r > a$ where the plasma interacts with

[1] In 2014 the TEXTOR was shut-down.

Parameter	TEXTOR	ASDEX Upgrade
Major plasma radius R_0	1.75 m	1.65 m
Minor plasma radius a	0.46 m	0.5 m
Vertical plasma radius b	0.46 m	0.8 m
Plasma volume	7 m^3	13 m^3
Elongation of cross-section b/a	≈1 (circular)	1.6 (D-shape)
Maximum magnetic field	3 T	3.9 T
Plasma current	<0.8 MA	<1.6 MA
Pulse duration	<10 s	<10 s
Plasma density	$<10^{20}$ m^{-3}	$<2\times10^{20}$ m^{-3}
Plasma temperature	<2.5 keV	<7 keV
Energy confinement time	<70 ms	<250 ms
Auxiliary heating	<9 MW	<26 MW

Table 3.1: The main geometry and plasma parameters of TEXTOR and ASDEX Upgrade.

the wall. Due to the 1/R dependence of the toroidal magnetic field the high field side (HFS, left side) and the low field side (LFS, right side) can be distinguished. The upper and lower parts of the poloidal cross-section are called top and bottom, respectively.

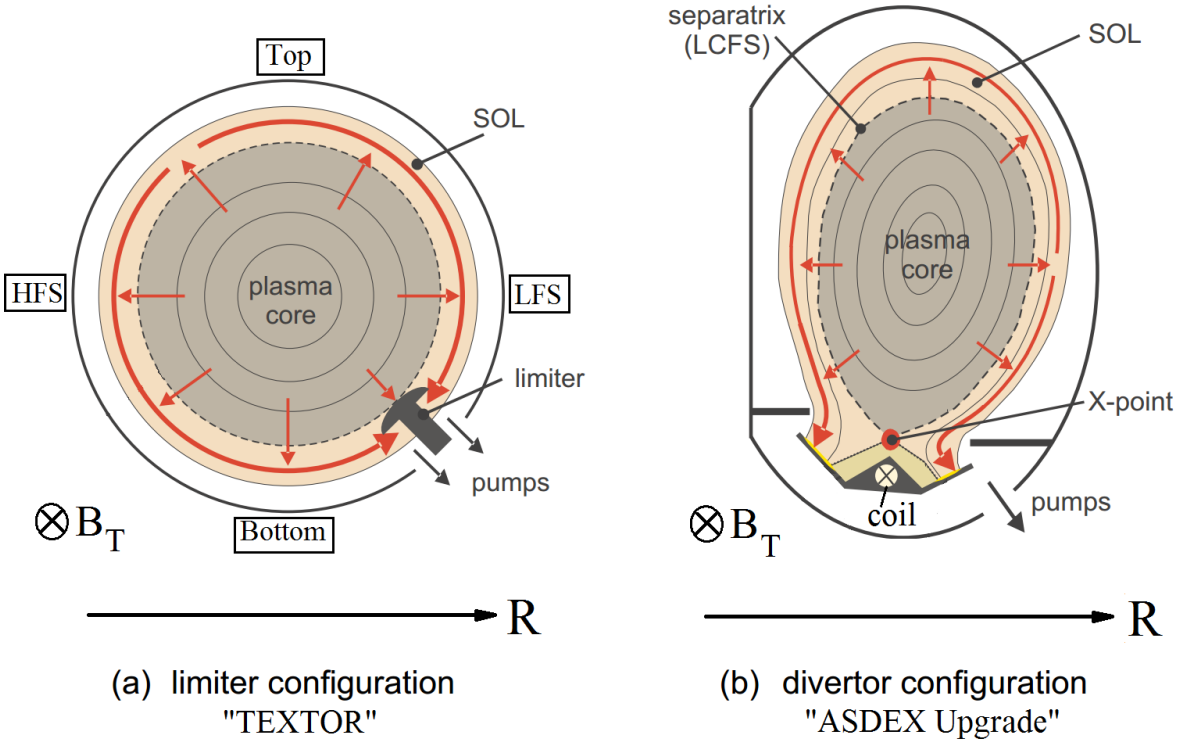

Figure 3.1: Sketch of a poloidal plasma cross-section from TEXTOR in a limiter configuration (a) and from ASDEX Upgrade in a divertor configuration (b). Adapted from [62].

ASDEX Upgrade (Axis Symetric Divertor EXperiment) is a tokamak with a D-shaped plasma cross-section (see figure 3.1b) located at the Max-Planck-Institute for Plasma Physics in Garching, Germany. The major radii R_0 of AUG and TEXTOR are similar. The range of plasma parameters (see table 3.1) and operation scenarios from AUG, however, exceeds that of TEXTOR. At AUG, a divertor concept is used, where the boundary surface hits the plasma walls with two strike lines in the lower part of the vessel (see figure 3.1b). This concept is realized by an additional coil placed in the bottom part of the vessel, which modifies the magnetic field at the edge creating an X-point. The X-point defines the last closed flux surface (LCFS) or separatrix at $\rho_{\mathrm{pol}} = 1$. Flux surfaces outside of separatrix $\rho_{\mathrm{pol}} > 1$ are not closed but end in the divertor region. Particles expelled from the plasma are guided to the divertor where they are pumped away. The divertor concept reduces the influx of sputtered wall material. The typical operation scenario used at AUG is the high confinement mode

(H-mode) achieving twice as high energy confinement compared to low confinement mode (L-mode). This mode was first discovered at ASDEX [19], which is predecessor of AUG.

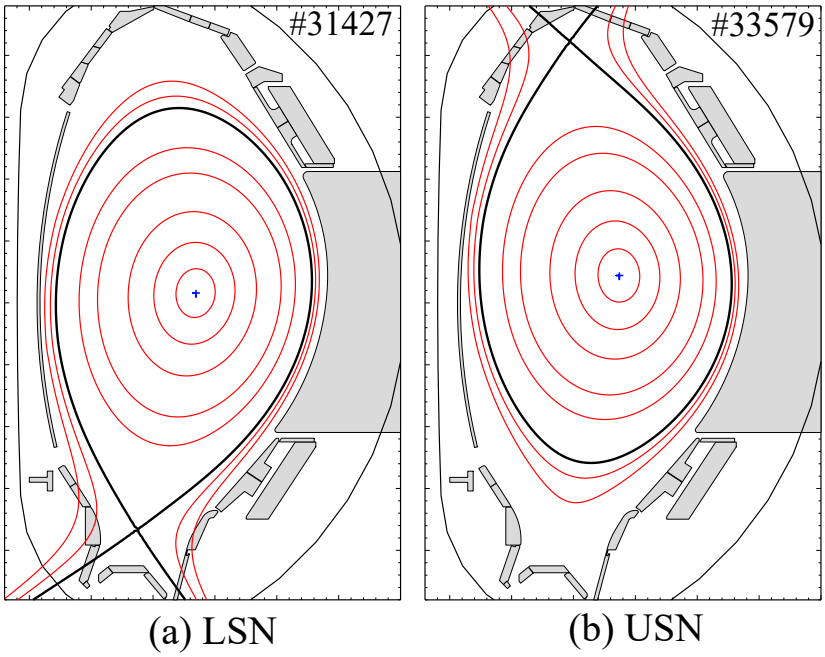

Figure 3.2: The different magnetic configuration achievable on AUG.

At AUG, there are different magnetic field configurations achievable (see figure 3.2). In the lower single null (LSN) configuration, the X-point is located in the lower part of the vessel and in the upper single null configuration (USN) the X-point is located in the upper part. A configuration with two X-points, called double null (DN), is also possible.

The standard magnetic field configuration of AUG plasma has a positive plasma current I_p (counter-clockwise direction, when viewed from above) and negative magnetic field B_T (clockwise direction). Such a configuration creates a left-handed helicity and a positive value of the magnetic field pitch angle $\alpha > 0$ (see figure 3.3a). According to equation 1.4 the electron and ion diamagnetic (ED and ID) drift directions for the standard configuration is oriented upward and downward, respectively, when viewed from the LFS. The sign of α depends on the sign of the product of B_T and I_p while the drift directions are given by the sign of B_T. The four possible combinations are shown in figure 3.3. The E×B drift direction is oriented in the ion diamagnetic direction when $E_r > 0$ and in the electron diamagnetic direction when $E_r < 0$.

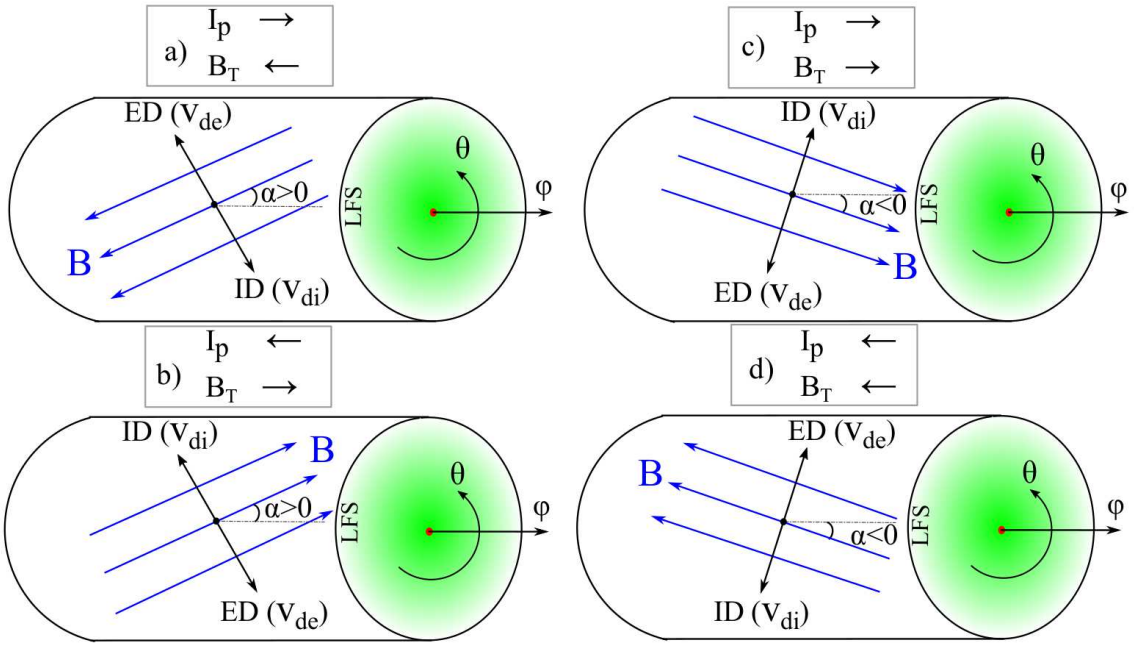

Figure 3.3: The different directions of electron and ion diamagnetic velocities v_{de} and v_{di} and magnetic field pitch angle α depending on the direction of plasma current I_p and toroidal magnetic field B_T.

3.2 Heating systems

In order to achieve the fusion relevant temperatures it is necessary to heat the plasma. An effective heating mechanism in tokamaks is the Ohmic heating (OH) due to the induced plasma current I_p. The power scales as $P_{OH} \propto I_p^2 R_p$, where I_p is plasma current and plasma resistivity scales as $R_p \propto T^{-3/2}$. Ohmic heating gets small at high temperatures. Consequently, additional heating systems such as neutral beam injection (NBI), ion cyclotron resonance heating (ICRH) and electron cyclotron resonance heating (ECRH) are used. The discharges performed for this thesis were mainly heated Ohmically. Some discharges had for diagnostic purposes or dedicated electron/ion heating some NBI or ECRH as well.

The principle of NBI heating is based on the injection of highly energetic neutral particles into the plasma. The particles after being ionized transfer their energy to the plasma through couloumb collisions with the electrons and ions. The NBI system at AUG consists of two injectors (located in sectors 7 and 15) with four sources each. Each source injects up to 2.5 MW so that the NBI system at AUG is equipped with in total 20 MW of power heating. Figure 3.4 shows the injection direction of one source from injector 2 called NBI source 8.

ECRH at AUG is based on the absorption of electromagnetic waves at the second harmonic of electron cyclotron resonance frequencies of 105 and 140 GHz. In total eight gyrotrons are available which can provide 6 MW power.

3.3 Relevant diagnostics

AUG and TEXTOR are equipped with a set of plasma diagnostics to monitor and investigate the behavior of the machine and the plasma. Figure 3.4 shows a poloidal cross-section and a top-down view of AUG with the most relevant diagnostics for this work. These diagnostics are described below, except the Doppler reflectometry (DR) and the poloidal correlation reflectometry (PCR), which are described in chapters 4 and 5.

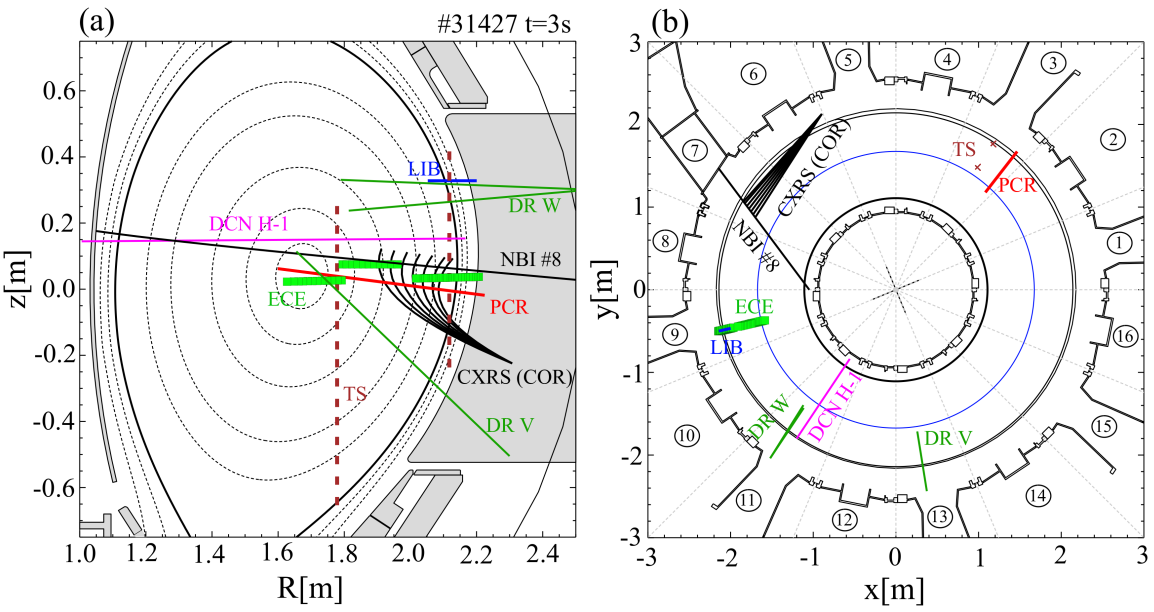

Figure 3.4: (a) Poloidal cross-section and (b) top-down view of AUG showing relevant diagnostics for this work.

3.3.1 Laser interferometry

One diagnostic which provides information on the line-averaged electron density $\bar{n}_e$ is laser interferometry. The diagnostic technique is based on the dependence of the wave

refractive index in O-mode polarization (see section 4.1) on the electron density n_e

$$N_O = \sqrt{1 - n_e \frac{e^2}{\varepsilon_0 m_e \omega^2}} \overset{\omega \gg 1}{\approx} 1 - n_e \frac{e^2}{2\varepsilon_0 m_e \omega^2}, \tag{3.1}$$

where e is the elementary charge, ε_0 the permittivity of free space, m_e the electron mass and ω the probing frequency. The second part of equation 3.1 assumes that the laser frequency is well above the cut-off frequency and therefore a Taylor expansion is applicable. The phase difference between the electromagnetic wave passing through the plasma with respect to passing through vacuum is equal to

$$\begin{aligned} \Delta\phi &= \frac{2\pi}{\lambda_0} \int (N_{vac} - N_O) \mathrm{d}x = \frac{\lambda_0 e^2}{4\pi c^2 \varepsilon_0 m_e} \int n_e(x) \mathrm{d}x \\ &= \frac{e^2}{4\pi c^2 \varepsilon_0 m_e} \frac{\lambda_0}{L} \bar{n}_e. \end{aligned} \tag{3.2}$$

Here $N_{vac} = 1$ is the refractive index of vacuum, λ_0 the vacuum wavelength of the probing wave and L the distance passed by the laser beam. The phase difference is directly proportional to the line average density $\bar{n}_e$ and measured using a phase detector. The density is assumed to be constant on a flux surface. Hence, a set of lines of sight (LOS) enables the reconstruction of the density profile $n_e(\rho_{\mathrm{pol}})$ using Abel inversion.

At AUG, a deuterium cyanide (DCN) laser is used for interferometry, which is operated at a wavelength of 195 μm [64] and provides a temporal resolution of 300 μs. The DCN system consists of 6 laser beams (H-0 to H-5) measuring the line averaged density along 6 different LOS. In this work only the line H-1 passing the plasma centre is used (see figure 3.4).

At TEXTOR, the interferometry system consists of 9 LOS and a laser with a wavelength of 336.6 μm [65] is used. The density profile is calculated from the line averaged data by Abel inversion every 10 ms.

3.3.2 Lithium beam

The electron density profile at the plasma edge is measured with the lithium beam diagnostic (LIB). The diagnostic injects neutral lithium (Li) atoms at an energy of 35–60 keV. Collisions between the neutral lithium atoms and the plasma particles leads to excitation, ionization and charge exchange processes, which are dependent on the local temperature and density. The radiative transition ($\mathrm{Li}_{2p \to 2s}$) at wavelength 670.8 nm is measured along different lines of sight. Using a forward model [66] the measured line radiation can be used to deduce $n_e(\rho_{\mathrm{pol}})$ of the plasma.

The LIB diagnostic at AUG [67] allows to measure density profiles from the scrape-off layer up to roughly $\rho_{\mathrm{pol}} \approx 0.98$ with a radial resolution of 6 mm. The temporal resolution of the diagnostic is 5 μs.

3.3.3 Thomson scattering

The electron temperature and density profiles in the plasma core and edge are measured with the Thomson scattering (TS) diagnostic. This diagnostic exploits the scattered wave from the interaction of an electromagnetic wave with the plasma electrons. The electric field of the wave accelerates electrons, which in turn emit radiation in all directions (incoherent scattering). The intensity of the scattered radiation is proportional to n_e, while the Doppler width of the scattered radiation is proportional to T_e. The contribution of ions is neglected due to the large mass difference ($m_i \gg m_e$).

The TS diagnostic at AUG uses Nd:YAG lasers [68, 69]. The system launches a laser beam at two positions vertically into the plasma (see figure 3.4). One laser enables measurements in the plasma core and the other at the edge. The scattered waves are measured with respectively 16 and 11 polychromators providing spatially resolved profiles. The diagnostic has a temporal resolution of 3 ms for the core and 8 ms for the edge.

3.3.4 Electron cyclotron emission

The electron temperature profile can also be measured using the electron cyclotron emission (ECE) diagnostic. The diagnostic is based on the generation of electromagnetic radiation due to the gyro-motion of electrons around the magnetic field lines [70]. For an optically thick plasma, Planck's law for the spectral radiance I_ω of a black body allows to determine T_e as

$$I_\omega = \frac{\omega^2}{2\pi^2 c^2} T_e. \tag{3.3}$$

The radiation frequency $\omega(R) = \zeta e B_T(R)/m_e$ (ζ stands for harmonics of the cyclotron radiation) depends on the radial position, therefore, a radial profile can be obtained.

The ECE radiometer at AUG uses 60 different frequencies at the second harmonic of the cyclotron resonance ($\zeta = 2$). The radial position of the measurement is given by the toroidal magnetic field profile $B_T(R) = B_{T0} R_0/R$ and depends therefore, on the value of the magnetic field B_{T0} at the magnetic axis R_0. For the standard configuration with $|B_{T0}| = 2.4$ T the measurement positions are shown in figure 3.4. The sampling rate of the system is 1 MHz. At the edge the measurements are not optically thick and therefore forward modeling is used to reconstruct $T_e(\rho_{\mathrm{pol}})$ profiles [71].

3.3.5 Charge exchange recombination spectoscopy

The temperature of the different ions in the plasma can be assumed to be the same[2]. Hence impurity ions are used to measure the main ion temperature $T_i(\rho_{\text{pol}})$. Furthermore, the impurity velocity $u_j(\rho_{\text{pol}})$ and density $n_j(\rho_{\text{pol}})$ profiles are measured using charge exchange recombination spectroscopy (CXRS). The diagnostic utilises the charge exchange reaction between an impurity ion (A) and the injected deuterium (D) from the NBI source [72, 73]

$$\begin{aligned} A^{Z+} + D^0 &\rightarrow A^{(Z-1)+*} + D^+ \\ A^{(Z-1)+*} &\rightarrow A^{(Z-1)+} + h\nu. \end{aligned} \tag{3.4}$$

The resulting recombined impurity ion is in an excited state and emits a photon $h\nu$ at a specific wavelength λ during the decay process. The intensity of the spectral line gives information on the impurity density, the Doppler width on the impurity temperature and the Doppler shift on the impurity velocity.

The CXRS systems at AUG measure typically boron (B), nitrogen (N), carbon (C) and helium (He) impurities depending on the impurity content of the plasma. In this thesis the recently upgraded core system with toroidal lines of sight [75] is used. The system consists of both LFS and HFS channels, however, for this work only LFS channels are of interest. The neutral particles for the system are injected from NBI source 8 (see figure 3.4), which can operate with short blips of ≈ 16 ms. These blips do not perturb the plasma too strongly.

3.4 Typical discharge waveforms

Figure 3.5 shows the time evolution of plasma parameters during a typical experiment analyzed in this thesis. The plasma current I_p and the magnetic field B_{T0} are kept constant during the whole discharge. The average electron density $\bar{n}_e$ is increased during the discharge using a feedback control of the gas puff on the DCN H-1 channel. In order to measure the main ion temperature T_i and the impurity toroidal rotation with CXRS, short NBI blips are applied. Despite of the high power of the blips (2.5 MW), the average NBI heating is small ($\langle P_{NBI}/P_{OH}\rangle < 0.25$) due to the short duration of the blips of 16 ms. The electron temperature T_e decreases with increasing density, because it is connected to the ion temperature through electron-ion collisional energy exchange

[2]The main ion temperature T_i and impurity temperature T_j are equal due to the short equilibration time ($\approx 50\,\mu$s) compared to the confinement time (≈ 100 ms) (see [59]).

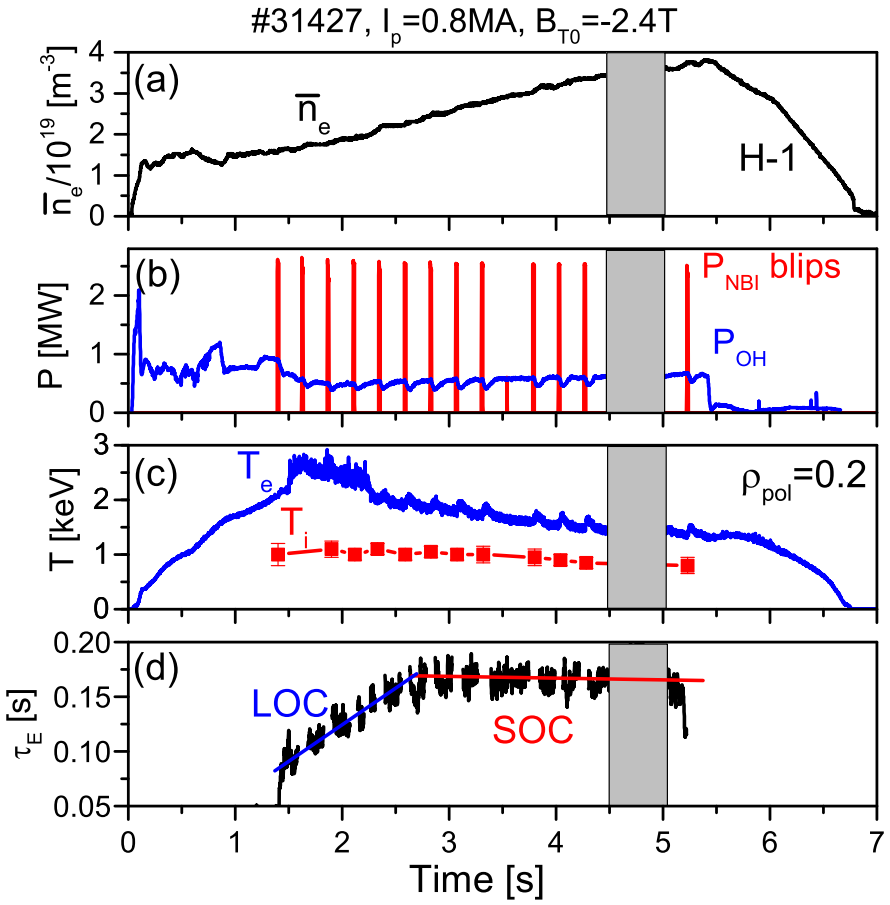

Figure 3.5: The time trace of plasma parameters for a typical discharge of a plasma current $I_p = 0.8$ MA and magnetic field $B_{T0} = -2.4$ T. From top to bottom, the following quantities are shown: (a) line averaged electron density $\bar{n}_e$, (b) Ohmic power P_{OH} and NBI blips P_{NBI}, (c) electron T_e and ion T_i temperatures at $\rho_{\mathrm{pol}} = 0.2$, (d) energy confinement time τ_E. The grey area contain transition to the H-mode plasma, which is not analyzed in this thesis.

$p_{ei} \propto n^2(T_e - T_i)/T_e^{3/2}$ which increases with density. The energy confinement time is evaluated between blips as

$$\tau_E = \frac{W_E}{P_{OH}} = \frac{\int \frac{3}{2}(n_e T_e + n_i T_i)\mathrm{d}V}{P_{OH}}, \tag{3.5}$$

where W_E denotes the plasma energy. In Ohmic plasmas, a linear increase of τ_E with the line averaged density is observed. However, above a critical density the energy confinement time saturates. The corresponding regimes have different transport properties and are named Linear Ohmic Confinement (LOC) and Saturated Ohmic Confinement (SOC) regime, respectively [12].

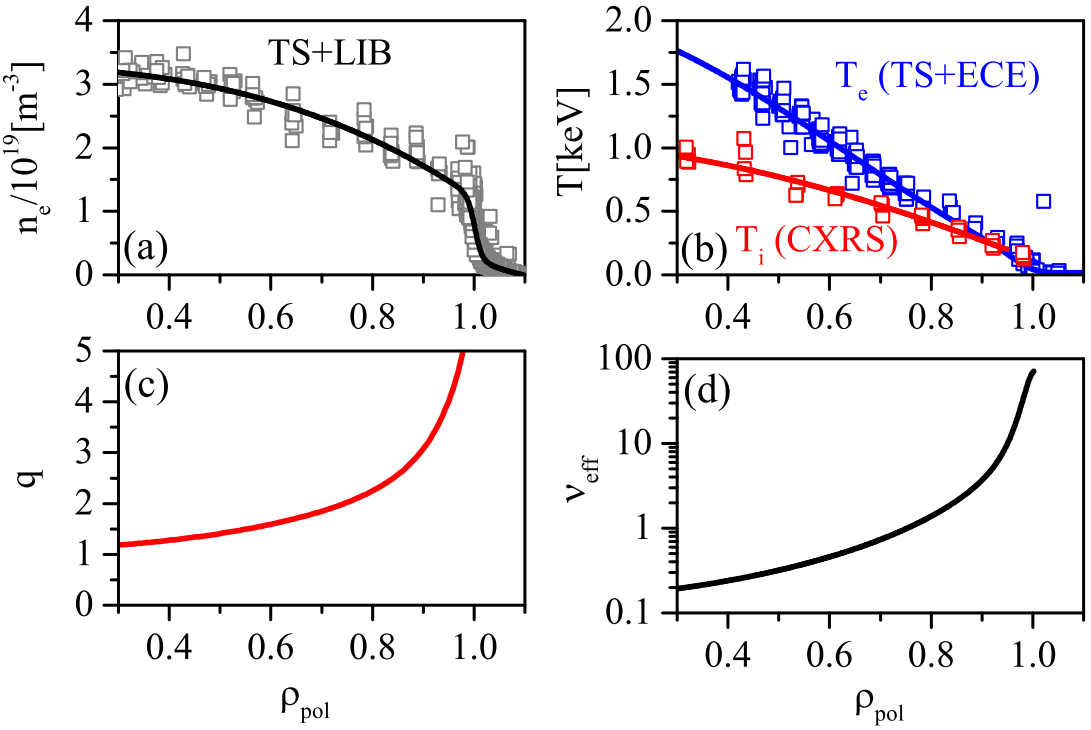

Figure 3.6: The profiles of electron density (a), electron and ion temperatures (b), safety factor (c) and effective collisionality (d) for a discharge #31427 at t=3.25 s.

Figure 3.6 shows typical radial profiles for electron density (a), electron and ion temperatures (b), safety factor (c) and effective collisionality $\nu_{\text{eff}} = \nu_{ei}/(c_s/R)$ (Here c_s is the sound speed) (d) at $t = 3.25$ s. q was calculated using the magnetic equilibrium from the CLISTE code [76], while the effective collisionality was evaluated using [58]

$$\nu_{\text{eff}} = 0.00279 \times \left(15.94 - 0.5 \log \frac{n_e}{T_e^2}\right) \times \frac{n_e}{T_e^2} R \sqrt{m_A} Z_{\text{eff}}, \tag{3.6}$$

where the density is given in units of 10^{19} m^{-3}, temperature in keV, m_A is the mass of the main ion in atomic mass units and Z_{eff} the effective charge. Here $m_A = 2$ and $Z_{\text{eff}} = 1.5$ were used.

4 Reflectometry diagnostic technique

In this chapter various types of reflectometry diagnostics relevant for this thesis and measurement parameters are presented. A reflectometry diagnostic launches a microwave beam into the plasma, which propagates until it reaches a cut-off condition, where the refractive index goes to zero, and is reflected. The reflected or scattered beam is measured with one or several receiving antennas.

4.1 Microwave propagation in plasma

The theory of microwave propagation presented in this section is based on the work of Ginzburg [77].

4.1.1 Wave equation

Electromagnetic waves with frequencies ranging from 0.3 to 300 GHz or vacuum wavelengths between 1 m and 1 mm are called microwave radiation. The wave electric field $\vec{E}$ of microwaves in plasmas is governed by the wave equation

$$\begin{aligned} \nabla(\vec{\nabla}\cdot\vec{E}) - \Delta\vec{E} &= \frac{\omega^2}{c^2}\hat{\varepsilon}(\omega)\vec{E} \\ \hat{\varepsilon}(\omega) &= \hat{\delta} + \frac{i}{\omega\varepsilon_0}\hat{\sigma}(\omega). \end{aligned} \tag{4.1}$$

Here $\hat{\varepsilon}(\omega)$ is the permittivity tensor, $\hat{\delta}$ the unity tensor and $\hat{\sigma}(\omega)$ the conductivity tensor. It is assumed that all fields have a local dependence $e^{-i\omega t}$. In the general case the permittivity tensor $\hat{\varepsilon}(\omega)$ has a complex form, however, it can be simplified for high frequencies. The procedure of calculating $\hat{\varepsilon}(\omega)$ is described in detail in [77]. The resulting permittivity tensor is expressed as (the coordinate system is shown in

figure 4.1)

$$\hat{\varepsilon}(\omega) = \begin{pmatrix} \gamma & ig & 0 \\ -ig & \gamma & 0 \\ 0 & 0 & \eta \end{pmatrix} \begin{matrix} (r) \\ (\perp) \\ (\parallel) \end{matrix} \qquad \begin{aligned} \gamma &= 1 - \frac{\omega_{pe}^2}{\omega^2 - \omega_{ce}^2} \\ g &= -\frac{\omega_{ce}}{\omega} \frac{\omega_{pe}^2}{\omega^2 - \omega_{ce}^2} \\ \eta &= 1 - \frac{\omega_{pe}^2}{\omega^2} \end{aligned} , \tag{4.2}$$

where the electron plasma ω_{pe} and cyclotron ω_{ce} frequencies are expressed as

$$\omega_{pe} = \sqrt{\frac{n_e e^2}{\varepsilon_0 m_e}} \qquad \omega_{ce} = \frac{eB}{m_e}. \tag{4.3}$$

4.1.2 O-mode vs X-mode propagation

Propagation in a uniform and homogeneous plasma can be described in the form of plane waves $E \propto e^{i\vec{k}\vec{r}}$. In this case the wave equation 4.1 becomes

$$k^2\vec{E} - \vec{k}(\vec{k}\cdot\vec{E}) = \frac{\omega^2}{c^2}\hat{\varepsilon}(\omega)\vec{E}. \tag{4.4}$$

In reflectometry experiments, electromagnetic waves are usually launched and received having the wave vector perpendicular to the confining magnetic field $\vec{B} = B\vec{e}_{\parallel}$, i.e. $\vec{k} = k_r\vec{e}_r + k_\perp\vec{e}_\perp$. Introducing the refractive index $\vec{N} = \vec{k}/k_0$ with $k_0 = \omega/c$ equation 4.4 can be written as

$$\begin{pmatrix} \gamma - N_r^2 & N_r N_\perp + ig & 0 \\ N_r N_\perp - ig & \gamma - N_\perp^2 & 0 \\ 0 & 0 & \eta - N^2 \end{pmatrix} \begin{pmatrix} E_r \\ E_\perp \\ E_\parallel \end{pmatrix} = 0. \tag{4.5}$$

The dispersion relation is obtained when the determinant of the matrix equals zero. Equation 4.5 has two non trivial solutions, which correspond to the different polarization modes. In the toroidal geometry of fusion devices the solutions can be illustrated with the help of figure 4.1, where waves are launched from the LFS of the tokamak in the direction of increasing density.

The ordinary mode (O-mode) propagation is obtained for the case when the wave's electric field vector is parallel to the magnetic field, i.e. $\vec{E} = E_\parallel\vec{e}_\parallel$. For this case the

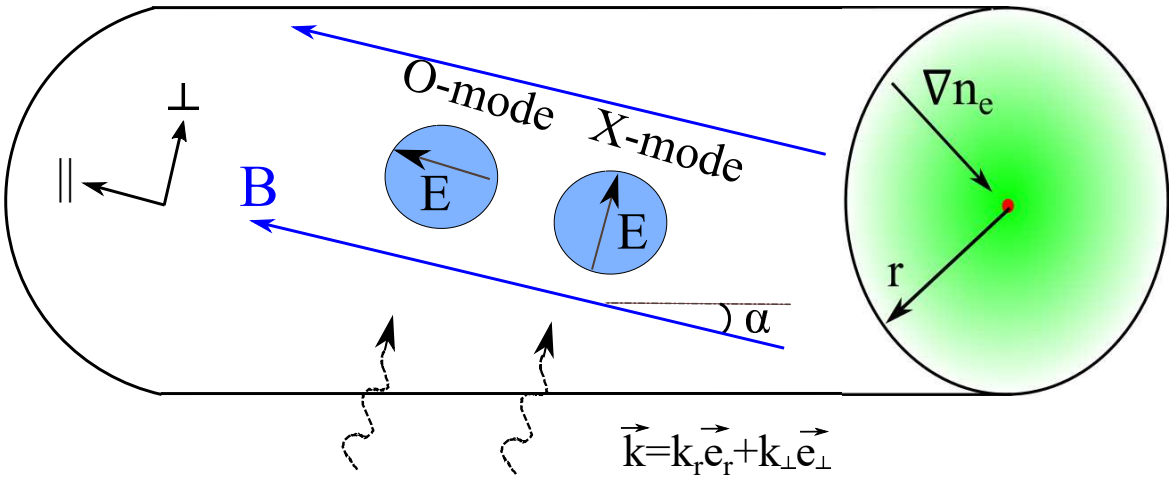

Figure 4.1: Two types of propagating modes. Ordinary mode with $\vec{E} \| \vec{B}$ (left) and extraordinary mode with $\vec{E} \perp \vec{B}$ (right). The blue spot represents the beam footprint on the magnetic surface.

refractive index is

$$N_O^2 = \eta = 1 - \frac{\omega_{pe}^2}{\omega^2}. \tag{4.6}$$

Here, the refractive index depends on the electron density of the plasma only.

The extraordinary mode (X-mode) propagation is obtained for the case when the electric field is perpendicular to the magnetic field, i.e. $\vec{E} = E_r \vec{e}_r + E_\perp \vec{e}_\perp$. For this case the refractive index is given by

$$N_X^2 = \frac{\gamma^2 - g^2}{\gamma} = 1 - \frac{\omega_{pe}^2}{\omega^2} \frac{\omega^2 - \omega_{pe}^2}{\omega^2 - \omega_{pe}^2 - \omega_{ce}^2}. \tag{4.7}$$

The X-mode refractive index depends on both the electron density and the local magnetic field, which is a superposition of the external toroidal magnetic field and a poloidal magnetic field due to the plasma current.

4.1.3 Cut-offs in plasmas

The refractive index of the free space is $N^2 = 1$. As the wave propagates through the plasma in regions where ω_{pe} and ω_{ce} are increasing, the refractive index of the wave decreases. A cut-off occurs when the refractive index changes from real ($N^2 > 0$) to imaginary values ($N^2 < 0$), i.e. at the point where $N^2 = 0$. At this point the wave will be reflected. The frequencies satisfying this condition for O-mode (f_O) and X-mode

(f_{XL} and f_{XU}) are

$$f_O = \frac{\omega_{pe}}{2\pi}$$

$$f_{XL} = \frac{1}{4\pi}(\sqrt{\omega_{ce}^2 + 4\omega_{pe}^2} - \omega_{ce}) \tag{4.8}$$

$$f_{XU} = \frac{1}{4\pi}(\sqrt{\omega_{ce}^2 + 4\omega_{pe}^2} + \omega_{ce}).$$

Figure 4.2 shows an example of electron cyclotron (f_{ce}), O-mode cut-off (f_O), lower (f_{XL}) and upper (f_{XU}) X-mode cut-off frequencies with respect to the radial position in the AUG. The plasma parameter profiles are from discharge #32294. In this thesis

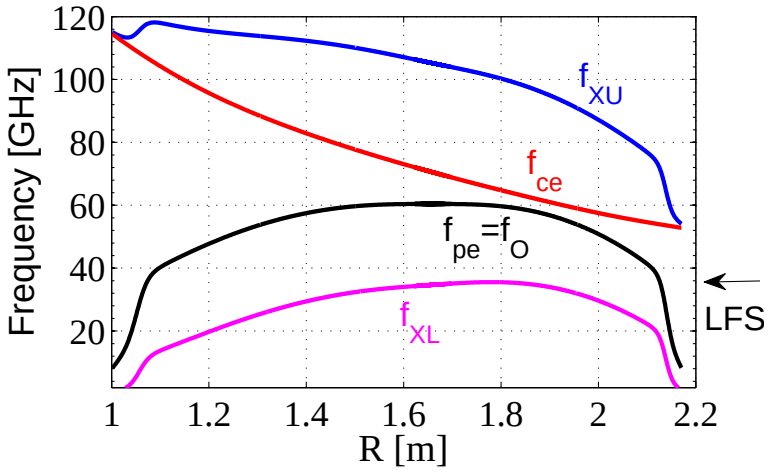

Figure 4.2: Values of electron cyclotron (f_{ce}), O-mode cut-off (f_O), lower X-mode (f_{XL}) and upper Xmode (f_{XU}) cut-off frequencies computed for discharge #32294 ($B_{T0} = -2.4$ T and $\bar{n}_e = 3.84 \times 10^{19}$ m^{-3}).

O-mode and upper X-mode cut-off frequencies are used to measure plasma parameters, where waves launched from the LFS of the tokamak.

4.2 Transfer function of fluctuation reflectometry in Born approximation

The reflected radiation from the cut-off layer can be treated as combination of the unperturbed reflected beam (as if there was no turbulent density fluctuations) and the scattered beam due to the interaction of turbulent density fluctuations with the incident

wave [78]. The scattered beam can be used to investigate density fluctuations. The mechanism of scattering is similar to Bragg scattering in crystals [79]. The scattered wave vector $\vec{k}_s$ is defined by the Bragg condition

$$\vec{k}_s = \vec{k}_i + \vec{k}. \tag{4.9}$$

Here $\vec{k}_i$ is the wave vector of the incident wave and $\vec{k}$ is that of the turbulent density fluctuations. If this equation is satisfied the energy transfer between scattered and incident wave is maximal. For the reflectometry application only the scattered part received by the antennas is important. Piliya [80] proposed a method to calculate the scattered signal received directly in the antenna based on a receptivity theorem. For small density fluctuations levels [81]

$$\left(\frac{\delta n_e}{n_e}\right)^2 \ll \frac{c^2}{\omega^2 l_r d_c}\left(\ln\frac{d_c}{l_r}\right)^{-1} \tag{4.10}$$

and O-mode polarization the measured complex signal is given by

$$I(t) + iQ(t) = C\int \frac{\delta n_e(\vec{r},t)}{n_c(f)} W(\vec{r})\mathrm{d}\vec{r}, \tag{4.11}$$

where l_r is the radial correlation length of turbulent density fluctuations, d_c the distance from the antenna to the cut-off position and C is a dimensional factor. $I(t)$ and $Q(t)$ are quadrature detector signals (see section 5.1). The complex weight function is defined as

$$W(\vec{r}) = W_I(\vec{r}) + iW_Q(\vec{r}) = \langle E_t(\vec{r},t)E_r(\vec{r},t)\rangle\,. \tag{4.12}$$

Here $E_t = E_{t0}(\vec{r})e^{i(\phi_t(\vec{r})+\omega t)}$ is the full-wave distribution of the electric field of the transmitting antenna in the unperturbed plasma (i.e. solution of equation 4.1 when density fluctuations are neglected) and $E_r = E_{r0}(\vec{r})e^{i(\phi_r(\vec{r})-\omega t)}$ is the fictitious field that would be excited by the receiving antenna if it wave of transmitting in the same unperturbed plasma. The brackets denote averaging over a period of the microwave radiation. Equation 4.11 is the generalization of the Born approximation [82] applied to the plasma. Similar equation for the scattered signal obtained in the received antenna has been obtained earlier by Hutchinson [78] using Green's function of equation 4.1, but in 1D geometry. This approximation gives a reasonable estimate of the signal only for small density fluctuation levels $\delta n/n < 1$–$4\,\%$ (calculated using equation 4.10). Equation 4.11 has been compared with full wave simulations and good agreement has been obtained for small density fluctuation levels [81, 83]. This regime is also called the linear regime of reflectometry. In the opposite case the nonlinear regime of reflectometry is obtained [85], when the incident wave experiences multiple scattering processes. Interpretation of the signal in the nonlinear regime is more challenging.

Equation 4.11 is used in section 6.4 to calculate the resolution of the reflectometry system at AUG. It shows that a scattered signal is proportional to the absolute value of the electric field in a plasma. As the wave approaches the cut-off layer its amplitude increases [77], hence the scattered energy also increases. This defines the localization of the scattering process close to the cut-off layer. The equation for a system with monostatic antennas and 1D geometry has been studied in [86]. In the arbitrary case, the relationship between measured signal and density fluctuations depends on the geometry of the beam and the electric field distribution.

4.3 Reflectometry diagnostics

In this section various types of reflectometry diagnostics relevant for this thesis are introduced.

4.3.1 Normal incidence reflectometry

Normal incidence reflectometry is based on the measurement of microwaves reflected from a cut-off layer. The transmitting antenna launches a microwave beam into the plasma, perpendicular to the confining magnetic field $\vec{k} \perp \vec{B}$ and parallel to the density gradient $\vec{k} \| \nabla n_e$ (figure 4.3). The wave propagates until it reaches the cut-off and

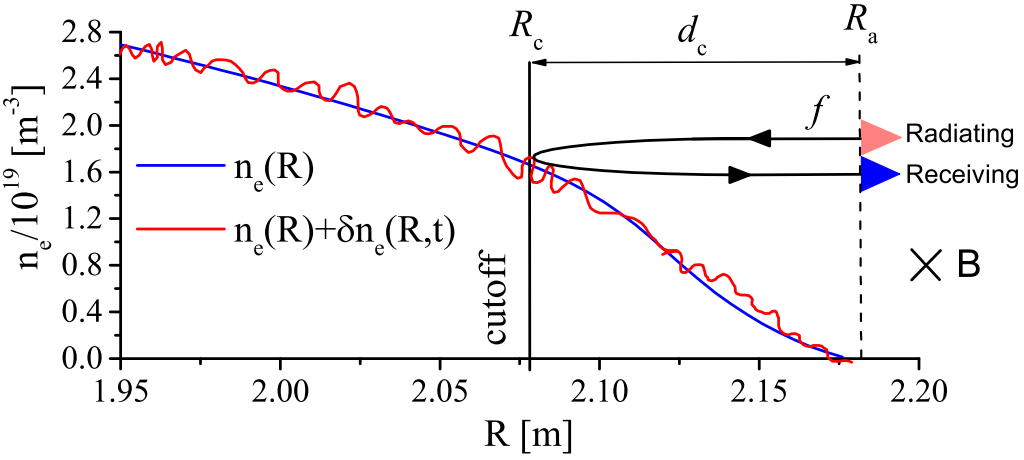

Figure 4.3: Schematic of reflectometry experiments. The microwave beam launched into the plasma from the radiating antenna is reflected at the cut-off position and measured by an receiving antenna.

is reflected. Depending on the probing frequency and polarization, the position of the reflection can be selected. The reflected beam is measured by the same antenna

(monostatic system) or by different ones (bistatic system). Since the reflection position depends the local plasma density, a density profile and fluctuations can be measured by reflectometry.

The method is similar to the radio detection and ranging (RADAR) system [87], that is used in echolocation. However, in contrast to RADAR, the phase difference between transmited and reflected waves in plasma is defined not only by the distance to the cut-off layer, but by an integral along the propagation path. The phase between transmitted and reflected beam is

$$\phi = 2k_0 \int_{R_a}^{R_c} N(R, f) \mathrm{d}R - \pi/2. \tag{4.13}$$

Here, R_a is the antenna position and R_c the cut-off position. The factor $\pi/2$ appears due to the reflection at the cutoff layer [77]. For O-mode polarization this gives

$$\phi(f, t) = 2k_0 \int_{R_a}^{R_c} \sqrt{1 - \frac{(n_e(R) + \delta n_e(R, t))e^2}{\varepsilon_0 m_e 4\pi^2 f^2}} \mathrm{d}R - \pi/2. \tag{4.14}$$

Here, it is supposed that the plasma is 'frozen', i.e. the frequency of any fluctuation is much smaller than the probing frequency $f = \omega/2\pi$ (MHz compared to tens of GHz). For small density fluctuation levels, $\delta n_e(R, t)/n_e(R) \ll 1$, it is possible to decompose the phase into a mean part and a fluctuating part $\phi(f, t) = \bar{\phi}(f) + \delta\phi(f, t)$. The mean phase is used for the density profile reconstruction (profile reflectometry) [88, 89, 90]. An Abel integral transform for O-mode propagation gives the distance to the cut-off position d_c and the mean density n_c at the cut-off position

$$\begin{aligned} d_c(f) &= \frac{c}{2\pi^2} \int_0^f \frac{\mathrm{d}\bar{\phi}/\mathrm{d}f'}{\sqrt{f^2 - f'^2}} \mathrm{d}f' \\ n_c(f) &= 4\pi^2 \varepsilon_0 m_e f^2 / e^2. \end{aligned} \tag{4.15}$$

The fluctuating part of the phase gives information about density fluctuations at the fixed reflection layer (fluctuation reflectometry) [91]

$$\delta\phi(f, t) = 2k_0 \int_{R_a}^{R_c} \frac{\delta n_e(R, t)}{n_c(f)} \frac{\mathrm{d}R}{N_O(R)}. \tag{4.16}$$

Since the refractive index N_O approaches zero at the cut-off, the phase fluctuation is most sensitive to density fluctuations at the cut-off position. This defines the localization of the density fluctuation measurement.

4.3.2 Doppler reflectometry

Doppler reflectometry (DR) is based on measurements of the backscattered signal from the cut-off layer. The transmitting antenna launches a microwave beam into the plasma at a specific tilt angle θ_0 with respect to the flux surface (see figure 4.4a). The polarization of the beam can be O or X-mode. The beam propagates in the plasma until it reaches a cutoff position, where the beam is reflected. At the cutoff layer (green line) the beam is sensitive to density fluctuations, which scatter the beam (see section 4.2). The backscattered radiation fulfills the Bragg condition $k_\perp = 2k_i$[1] (see equation 4.9 for $k_i = -k_s$). This backscattered radiation is measured by the same or a different antenna (see figure 4.4b). If the density fluctuations are moving, the frequency of the backscattered signal is Doppler shifted by $2\pi f_D = v_\perp k_\perp$. Therefore, a simple relation is obtained for the perpendicular velocity $v_\perp(k_\perp) = 2\pi f_D / k_\perp$. The perpendicular

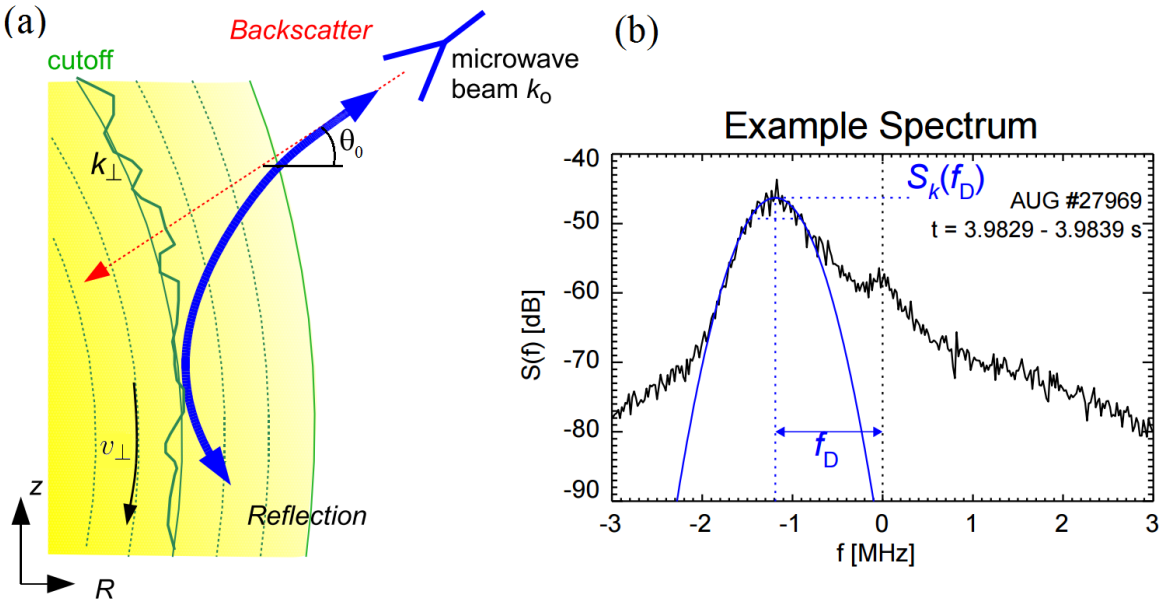

Figure 4.4: Principles of DR diagnostic. (a) A density fluctuations moving with perpendicular velocity $v_\perp$ cause back-scattering waves. (b) The Doppler shift f_D of backscattered signal is proportional to $v_\perp(k_\perp)$ at the cutoff layer. Adapted from [92, 93]

velocity of turbulent density fluctuations is composed of the $E \times B$ drift and the phase velocity of the turbulent structures

$$v_\perp(k_\perp) = E_r/B + v_{ph}(k_\perp) \tag{4.17}$$

[1] In slab geometry $k_\perp = 2k_0 \sin(\theta_0)$, where k_0 is vacum wavenumber of the probing wave.

and therefore depends on the perpendicular wavenumber $k_\perp$. Different $k_\perp$ can be selected by varying the probing wavenumber $k_0 = 2\pi f/c$ and the incidence angle θ_0. AUG is equipped with several DR:

1. Two V-band (50–75 GHz) systems, one for O-mode and one for X-mode, located in sector 13 [92] (see figure 3.4). Both are fixed angle antenna systems.
2. The W-band (75–110 GHz) system located in sector 11 [93] (see figure 3.4). The system uses a mechanically movable mirror, which can scan θ_0 from $-30°$ to $3°$ during one discharge. This option permits to measure the velocity $v_\perp(k_\perp)$ for different perpendicular wavenumbers $k_\perp$.

The location of the measurement and the perpendicular wavenumber at AUG is determined using the beam tracing code TORBEAM, which takes the real density profiles and the magnetic equilibrium as input [94].

4.3.3 Correlation reflectometry

The normal incidence reflectometry diagnostic, which is described in section 4.3.1, uses only one receiving antenna to measure the reflected wave. Hence, the density fluctuations are measured in one specific detection volume. Several different correlation

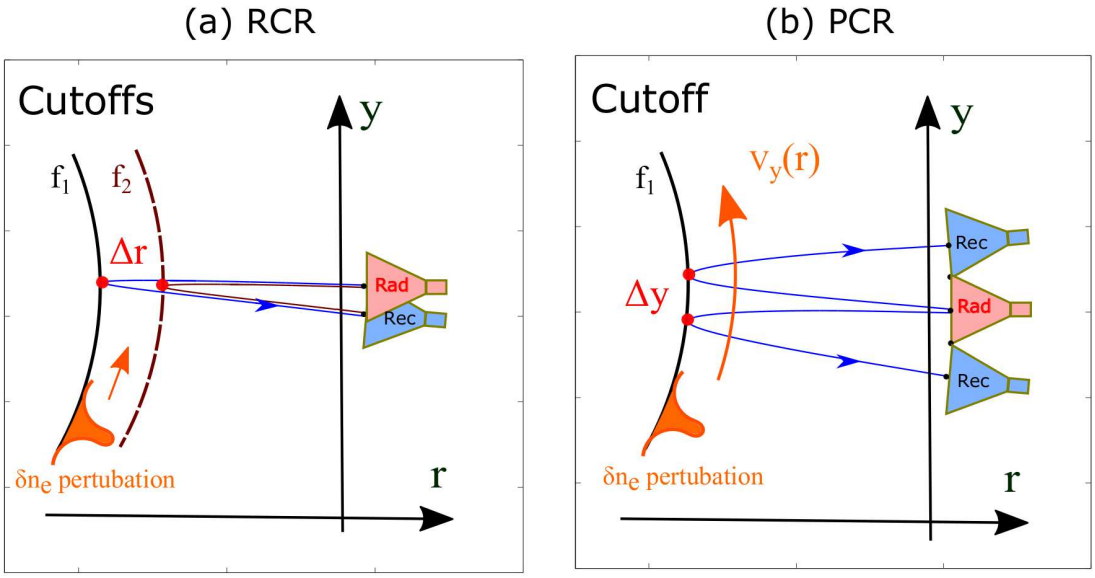

Figure 4.5: Comparison of (a) radial correlation reflectometry and (b) poloidal correlation reflectometry schemes. Red is the emitting antenna and blue are receiving antennas.

measurements are possible with reflectometry. The radial correlation reflectometry (RCR) scheme is shown in figure 4.5a. In this scheme signals at two different probing frequencies (f_1 and f_2) are measured simultaneously. The detected volumes (red points in figure 4.5a) have a radial separation Δr. If Δr is small one can measure the radial correlation length l_r of the density fluctuations from cross-correlation analysis. The application of RCR is described in [95, 96, 97, 98]. Theoretical limitations of this approach were investigated in [83, 84, 86].

Alternatively, signals can be measured at the same reflection layer, but with several poloidally or toroidally separated antennas. The poloidal correlation reflectometry (PCR) scheme is shown in figure 4.5b. If density fluctuations propagate in poloidal direction with velocity v_y a time delay between signals from different measurement volumes would allow to measure v_y. Note that the separation between the antennas cannot be too high, because density fluctuations decorrelate during propagation. In other words the condition $\Delta y < v_y \tau_d$ should be fulfilled, where τ_d is the decorrelation time of density fluctuations. Using a cluster of receiving antennas with several poloidally and toroidally separated antennas the PCR system can measure the perpendicular correlation length ($l_\perp$), the decorrelation time (τ_d) and the fluctuation propagation velocity ($v_\perp$). From the assumption of elongated density fluctuations in the direction of the magnetic field line the pitch angle α can be estimated as well [99, 100].

First PCR systems have been used at the JET [101, 102, 97] and T-10 [103, 104, 105] tokamaks with 2 receiving antennas. At TEXTOR a four receiving antennas system is used similar to that in figure 5.1. Applications of the TEXTOR system are described in [43, 106, 107]. Recently a PCR system operated in X-mode has been installed at the EAST tokamak [108, 109]. Theoretical analyse of PCR capabilities have been done using a 3D WKB approach [110, 111, 112] only. In this work a new poloidal correlation reflectometry system was developed and installed at AUG.

For readers it may be also of interest that the technique of a reflected wave measurement with several antennas is also applied outside of plasma applications as method of contactless velocimetry e.g. for vehicle velocity [113] or wind measurements [114].

5 Poloidal correlation reflectometry

In this chapter the poloidal correlation reflectometry (PCR) diagnostics installed at TEXTOR and ASDEX Upgrade are presented. The systems measure the reflected microwave beam with a cluster of 4 receiving antennas, distributed poloidally and toroidally with respect to the launching antenna. Figure 5.1 shows schematically the PCR antenna array installed on AUG. By cross-correlating the reflectometer signals from arbitrary antenna pairs, properties of the density fluctuations, such as the perpendicular correlation length ($l_\perp$), decorrelation time (τ_d), the fluctuation propagation velocity ($v_\perp$) and the inclination of the eddy α, being a measure of the pitch angle of magnetic field lines, can be obtained. The details of the new PCR system installed at AUG and its assessment is presented.

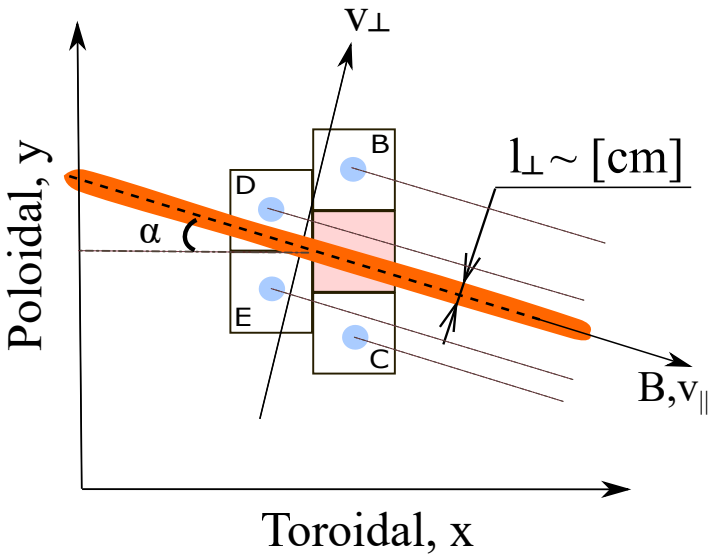

Figure 5.1: Schematic of the PCR antenna array on ASDEX Upgrade. Rad (red) is the transmitting while B, D, E, C (blue) are receiving antennas. A turbulent eddy (orange) aligned parallel to the magnetic field moves in the perpendicular direction in front of the PCR antennas.

5.1 Microwave circuitry

The PCR diagnostics at TEXTOR and AUG use a microwave scheme with heterodyne receiver. Such scheme, shown in figure 5.2, consists of a microwave source ω_i, transmission lines, transmitting (TX) and receiving (RX) antennas, heterodyne receiver [70] and IQ detectors. In order to measure the reflected wave, the received signal should

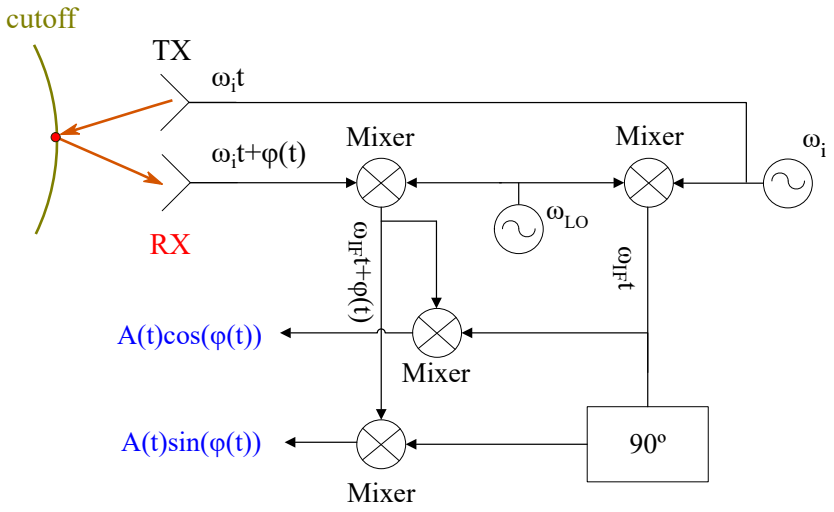

Figure 5.2: Components of a reflectometer: microwave source ω_i, transmission lines, transmitting (RX)/receiving (TX) antennas and a heterodyne receiver.

be downconverted to a lower frequency. In a heterodyne receiver two frequencies are used and signal mixing is obtained in two steps. In the first step the reflected and the local reference signals (ω_i) are downconverted to an intermediate frequency (ω_{IF}) by mixing with a local oscillator frequency $\omega_{LO} = \omega_i + \omega_{IF}$. This procedure for the reflected signal gives

$$A(t)\cos(\omega_i t + \phi(t)) \otimes \cos(\omega_{LO} t) \rightarrow A(t)\cos(\omega_{IF} t + \phi(t)). \tag{5.1}$$

The high frequency harmonic ($\omega_i + \omega_{LO}$) is removed by using a filter. In a second step the signal shifts to zero frequency by mixing with the intermediate frequency ω_{IF} and filtering the harmonic ($2\,\omega_{IF}$)

$$A(t)\cos(\omega_{IF} t + \phi(t)) \otimes \cos(\omega_{IF} t) \rightarrow I(t) = A(t)\cos(\phi(t)). \tag{5.2}$$

This procedure is repeated simultaneously using a signal shifted by $\pi/2$

$$A(t)\cos(\omega_{IF} t + \phi(t)) \otimes \sin(\omega_{IF} t) \rightarrow Q(t) = A(t)\sin(\phi(t)). \tag{5.3}$$

The last mixing step is also called IQ detection. By combining the two signals the phase of the received microwave beam and its amplitude can be reconstructed. Indeed using the complex signal both $\phi(t)$ and $A(t)$ can be obtained as

$$\begin{aligned} I(t) + iQ(t) &= A(t)e^{i\phi(t)} \\ \phi(t) = \pm \operatorname{atan}\left(\frac{Q(t)}{I(t)}\right) \qquad A(t) &= \sqrt{I(t)^2 + Q(t)^2}, \end{aligned} \tag{5.4}$$

where the sign of ϕ has to be chosen according to the complex plane. A heterodyne receiver offers a low noise signal which is important for correlation measurements and simplifies the operation with a tunable probing frequency [70].

5.2 Installation on TEXTOR

A PCR diagnostic was developed and used on the (now defunct) TEXTOR tokamak [107]. The PCR diagnostic had a restricted probing frequency range covering the Ka-band (27–37 GHz) corresponding to local densities of $0.9–1.7 \times 10^{19}$ m^{-3} in O-mode polarization. Two antenna arrays were operated (each with one launching and four receiving antennas): one array pointing inwards from the tokamak low field side

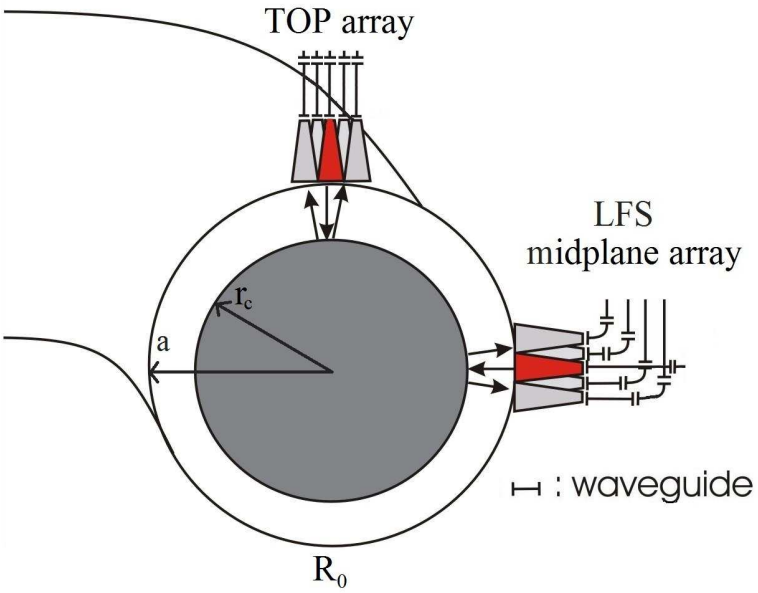

Figure 5.3: Schematic TEXTOR PCR front-end showing two arrays at the TOP and LFS midplane. Red is the emitting antenna and grey are receiving antennas.

(LFS) mid-plane and one array pointing downward from the vessel top at the plasma major radius R_0. The transmitting microwave generator and the heterodyne receivers were connected to the antennas by fundamental Ka-band waveguides. The microwave oscillator could be switched to any antenna combination in the top and LFS arrays. The antenna arrangement is shown in figure 5.3. The top array used rectangular horn antennas with an opening of 19×39 mm^2 while the LFS array used circular antennas with a diameter of 50 mm. The poloidal angle separation of the different combinations was $\Delta\theta = (0.025, 0.05, 0.075, 0.1)$ radian for the LFS and top arrays.

The launched beam and the receiver reference beam (with a 20 MHz offset) are generated by a YIG oscillator with low phase noise [115]. The reflected and the reference beams are combined in fundamental mixers followed by I/Q detectors. The resulting I and Q output signals are recorded with 14 bit resolution using INCAA data loggers at 1 MHz (later updated to 2 MHz).

5.3 Installation on AUG

This section describes details of the new PCR system developed and installed at ASDEX Upgrade. The PCR system at AUG currently operates over both the Ka- (24–37 GHz) and U-band (40–57 GHz). This entire frequency range corresponds to a local density range of 0.9–4$\times 10^{19}$ m^{-3} in O-mode polarization.

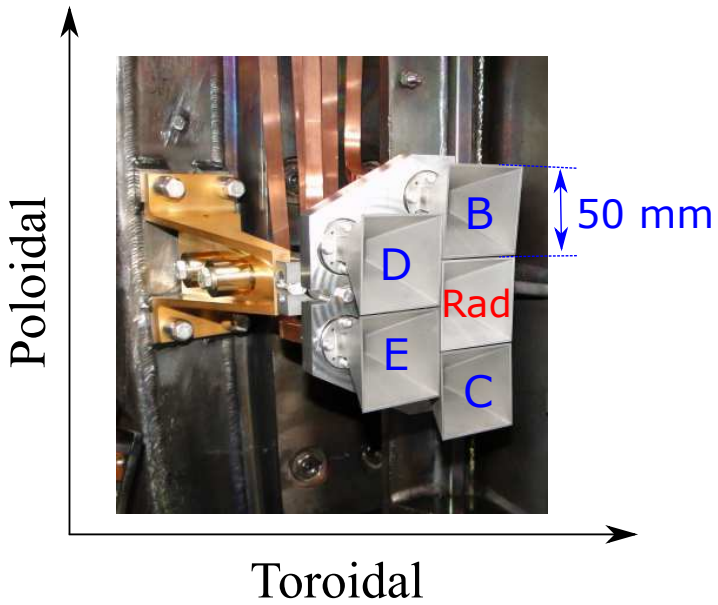

Figure 5.4: A photo of antenna cluster, as installed on the ASDEX Upgrade tokamak. 'Rad' is the transmitting antenna and B, C, D, E are receiving antennas.

5.3.1 Antenna cluster

A new 5 antenna array with square aperture horns of 50×50 mm^2 was designed. Such an antenna shape permits both O- and X-mode polarization measurements. The separation between receiving antenna orifices amounts to $(25, 50, 75, 100)$ mm in the poloidal direction and $(0, 50)$ mm in the toroidal direction. The geometry of a horn antenna is shown in appendix A. Figure 5.4 is a photograph of the antenna array mounted on the vessel at the mid-plane of the LFS. All antennas have been aligned to focus to the same point at $R = 1.6$ m and $y = +60$ mm (magnetic axis). For a typical plasma configuration, the plasma column is shifted up from the geometrical centre by ≈ 60 mm. To minimize a possible Doppler shift in the reflected signal due to poloidal movement, the antenna cluster is titled upwards by 5°. The exact position of the installed antenna cluster is measured with a coordinate measuring device. In figure 5.5 the lines of sight of all antennas are shown, calculated as normal to the antenna mouths. The antenna cluster was tested using a mirror installed in front of the array.

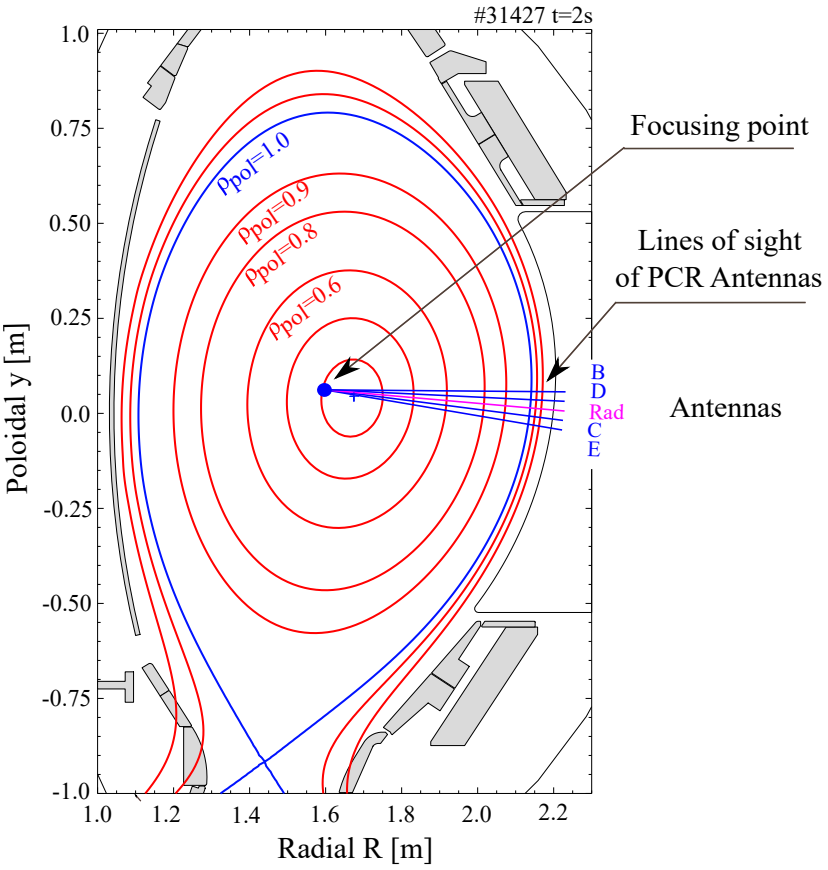

Figure 5.5: Lines of sight of PCR antennas. All antennas are focused to $R = 1.6$ m.

Note that electric field of TE_{10} and TE_{01} fundamental modes of antenna radiation are aligned in toroidal and poloidal direction, but not parallel and perpendicular to magnetic field lines. A different magnetic field pitch angle ($-10° < \alpha < 10°$) results in a lower amplitude of the received O- and X-mode components, but does not affect the measurements significantly.

The antenna radiation pattern $I(\theta) = r^2|E^2|$ in the far field region of the horns have been calculated using a Matlab package [116]. The half power beam width $\Delta\theta_{3dB}$ varies from 16 to 32° depending on frequency. For more details on the calculated power distribution see appendix A. The antenna radiation pattern has not been measured.

5.3.2 Waveguides and grid polarizer

Due to the limited space inside the AUG vessel the connecting waveguide path is complicated and has a total length of about 10 m in one direction. The inner dimension of the waveguide is 10×10 mm^2 to allow for both O-mode and X-mode propagation. A schematic CAD model of the external and internal waveguides is shown in figure 5.6. Different waveguides are marked by different colours with purple for the radiation path. The waveguide loss per one way has been measured to be 7–11 dB, depending on frequency. In figure 5.6 several significant bends in the waveguides (shown by red arrows) are visible. The most significant bending is located close to the antennas, reaching 105° with a curvature radius of 30 mm. Unfortunately, measurements have shown that such tight bending causes significant cross-conversion between TE_{10} and TE_{01} fundamental waveguide modes, which complicates the separation between O- and X-mode polarization (i.e. both polarization modes will be measured simultaneously).

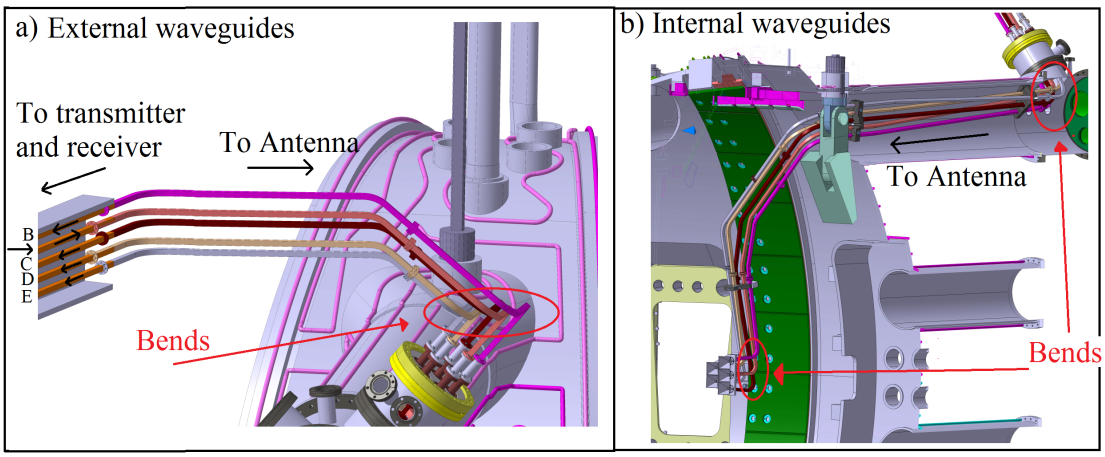

Figure 5.6: CAD model of external and internal waveguides connecting the antenna with the transmitting/receiving components.

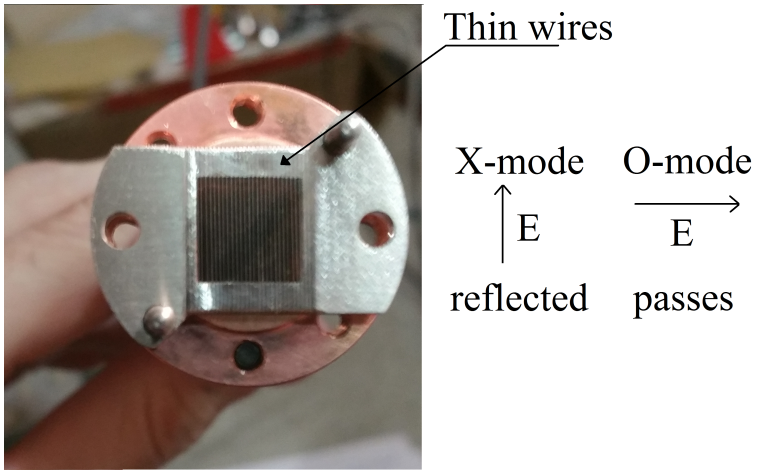

Figure 5.7: Photography of the grid polarizer which has been installed on all receiving antennas. The polarizer is blocking X-mode polarization and passing O-mode polarization.

As a temporary solution to avoid the cross-polarization measurement wire grid polarizers were designed and installed behind all receiving antennas. The wire grid polarizer consists of 27 thin metal wires aligned in one direction (figure 5.7). The principle of the grid polarizer can be explained as follows. An incident wave on a polarizer with electric field parallel to the wires will be reflected, while the perpendicular component will freely pass. The polarizers were installed such that only O-mode polarization is measured and X-mode rejected. The wire grid polarizer was tested and shown to have -30 dB rejection of the unwanted mode.

5.3.3 Generators

The cross-correlation analyses of different receiving antennas requires a low noise level in the measured signal. The significant portion of the noise is due to phase noise of the generator. This can be a problem when a small values of the phase fluctuations ($\delta\phi \ll \pi$) need to be detected. In this thesis two new independent dual-channel low noise (-150 dBc/Hz wide-band noise) microwave synthesizers are used for the transmitter and local oscillator sources. The synthesizers operate in the range of 3–5 and 10–15 GHz simultaneously. Active frequency multipliers ($\times 8$ and $\times 4$) extend the frequencies up to the Ka-band (24–40 GHz) and U-band (40-60 GHz) ranges. The microwave synthesizers at AUG can operate in fast frequency stepping mode with a transient switching time of < 60 μs permitting an arbitrary frequency pattern (with 5000 frequencies maximum). Hence, different plasma cut-offs can be scanned on the short time scale.

A program in Java with a GUI interface was written for controlling the synthesiz-

ers. The program uses an Ethernet interface of the generators and permits remote programming of the frequency pattern and duration of each step. The software can be used on both Windows and Linux platforms. An example of a typical pattern after multiplication of the frequencies is shown in figure 5.8. This pattern is repeated several times during one discharge. It is important to note that the U-band has a gap between 40 and 45 GHz due to high attenuation in the waveguides for these frequencies.

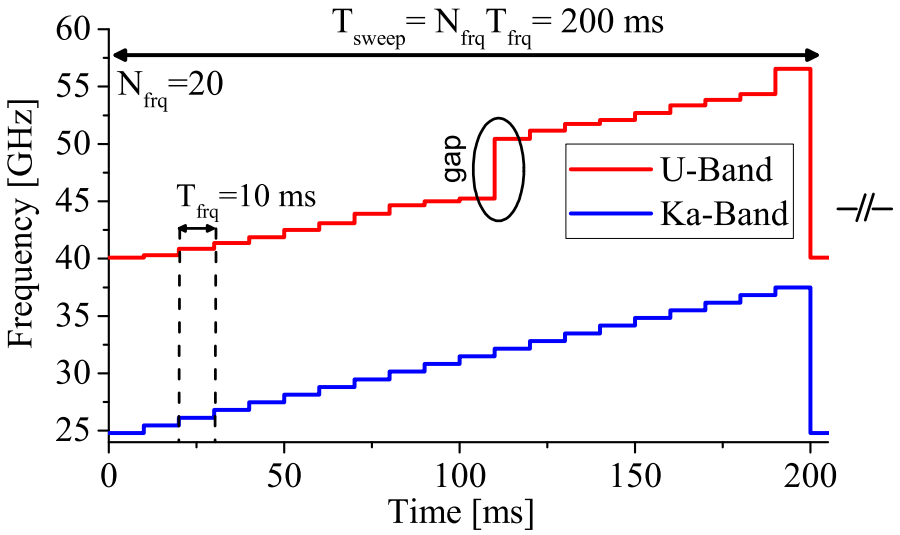

Figure 5.8: The shown frequency program repeats several times during one discharge.

5.3.4 PCR scheme

A schematic of one Ka-band channel (emitting and one receiving channel) is shown in figure 5.9. A dual-channel low noise (−150 dbc/Hz wide-band noise) microwave synthesizer in the range of 3–5 GHz is used as transmitter and local oscillator (LO) sources. For heterodyne detection, the transmitter and LO have a fixed frequency difference of 2.5 MHz. Active multipliers (×8) and power amplifiers extend the frequencies up to the Ka-band range. The power of the launched microwave prior waveguide path is about 40 mW across the band. The reflected signal and the local reference signal are down-converted to an intermediate frequency (IF) of 20 MHz by a mixer, followed by low frequency amplifiers and I/Q-detection section. The I and Q signals are digitized using a 2 MHz serial IO (SIO) ADC with 12 bit resolution. This scheme is repeated 4 times for all receiving antennas. A similar scheme is used for the U band, but with a 10–15 GHz range for the microwave synthesizer prior to (×4) up-conversion

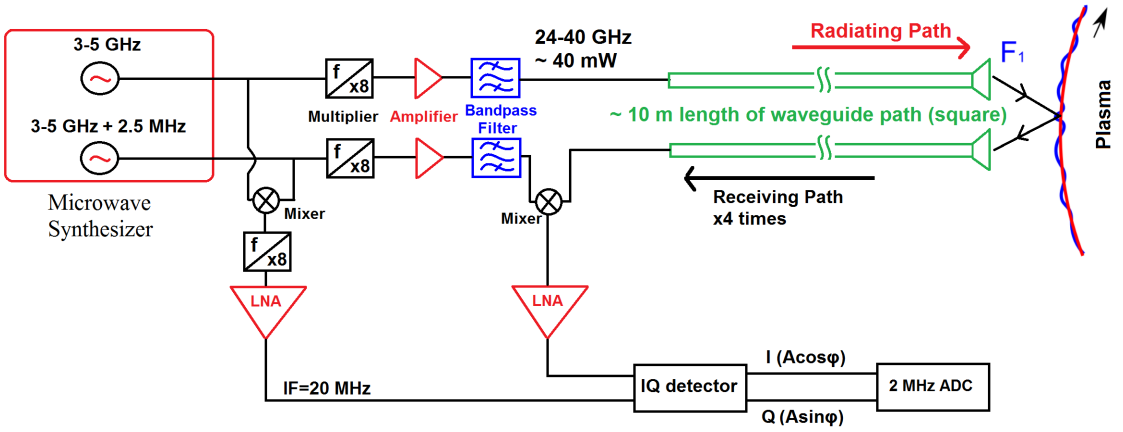

Figure 5.9: A schematic of one Ka-band channel (emitting and one receiving channel) of the PCR on AUG.

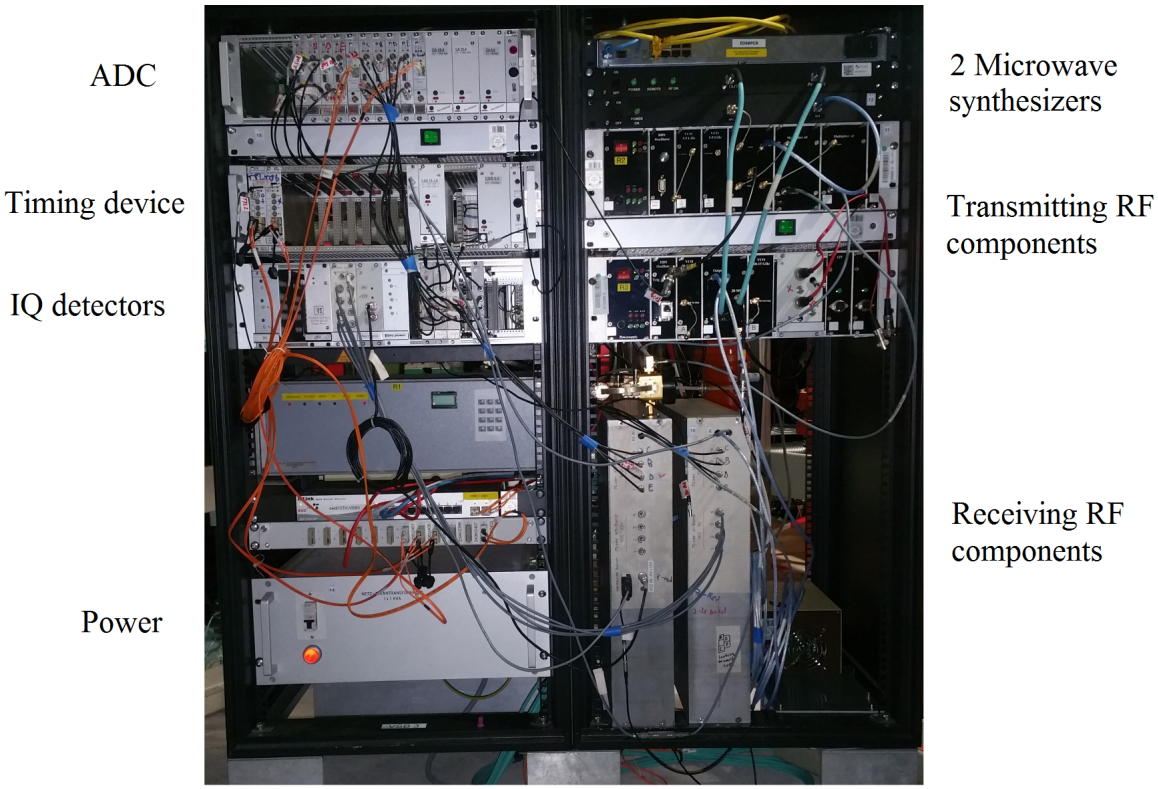

Figure 5.10: Hardware box with components of the PCR system.

to U-band. During each plasma discharge both the Ka- and U-band data are collected simultaneously. All external components of the reflectometer are mounted in one double rack (figure 5.10) installed in the torus hall.

5.4 Assessment of the AUG system performance

In O-mode operation the measurement radial position depends on the density profile. For (low) core line averaged densities of $\bar{n}_e \simeq 1.6 \times 10^{19}$ m^{-3} the system is capable of measuring density fluctuations from the plasma core to the edge $\rho_{\mathrm{pol}} = 0.4$–$0.9$. For higher densities ($\bar{n}_e \simeq 4.7 \times 10^{19}$ m^{-3}) only the edge region $\rho_{\mathrm{pol}} = 0.95$–$1.0$ is accessible.

The first test of the PCR system at AUG was performed without plasma, using a mirror installed 50 cm in front of the antenna cluster. An I/Q detector signal of an amplitude of ≈ 30–100 mV (peak value) was measured by all receiving antennas. The reconstructed phase using equation 5.4 was constant without significant oscillation.

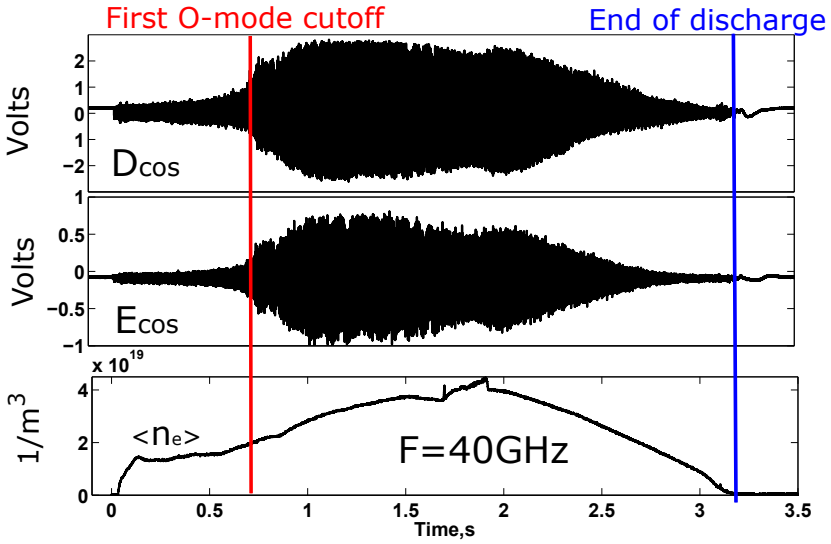

Figure 5.11: Reflected signals from plasma measured by in-phase detectors for the antenna D and E.

Figure 5.11 shows the signals recorded by in-phase I(t) detectors for the antennas D and E (D_{cos} and E_{cos}) during a plasma discharge. A fixed frequency of 40 GHz (U-band) has been used for this case. The signals from other antennas look similar. After plasma formation at $t = 0$ s a signal amplitude of ≈ 100 mV is obtained, although the cut-off still does not yet exist (density too low). For this case the reflectometer works as an interferometer. At $t = 0.7$ s there is a significant increase in amplitude

due to the appearance of the O-mode cut-off and the amplitude reaches ≈ 0.5–2 V. The different amplitudes for antenna D and E are due to different attenuations in the waveguides. The opposite behaviour is observed at the end of discharge, $t = 2.7$ s, where the density decreases and the cut-off disappears. The phase shift between in-phase I(t) and out-phase Q(t) signals has been measured close to 90° for all antennas. Due to old electronics it is necessary to calibrate the 90° shift of IQ detectors from time to time again.

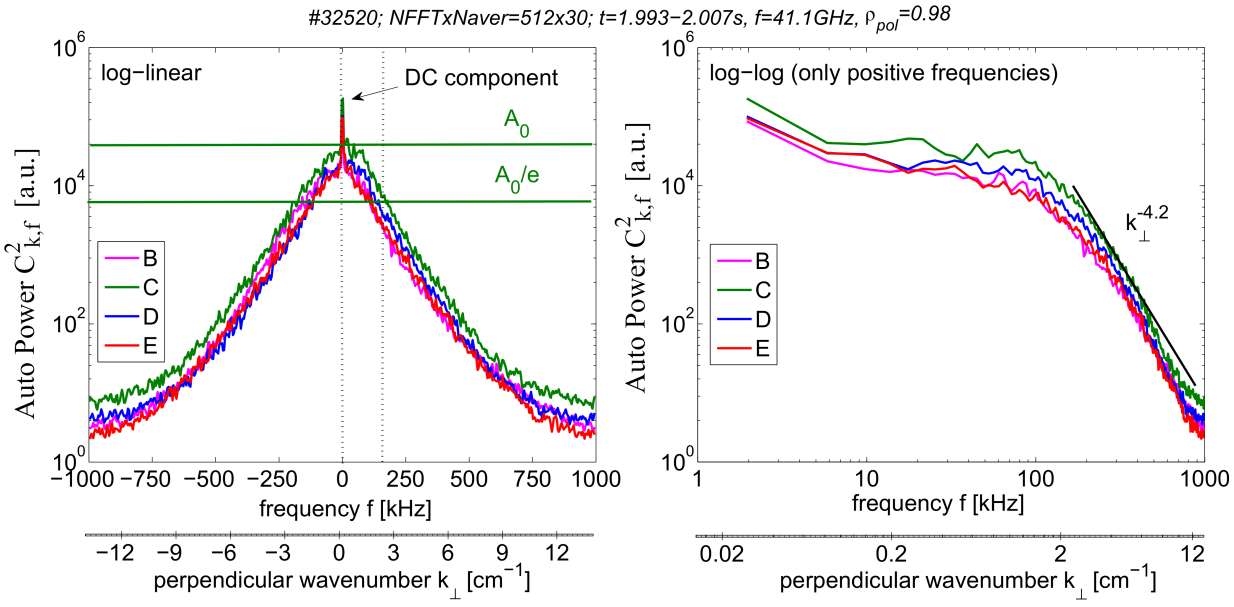

Figure 5.12: Turbulence auto power spectrum measured at probing frequency 41.1 GHz for discharge #32520. The wavenumber scale was calculated as $k_\perp = 2\pi f / v_\perp$.

The mean component of every signal is extracted and the complex signal is calculated as C(t) =I(t)+iQ(t) for every antenna. This signal includes both amplitude and phase information (equation 5.4). The auto power spectrum of the complex signal C(t) from discharge #32520 is shown in figure 5.12 for all receiving antennas. The spectrum is calculated with 512 points and averaged for 30 non overlapping windows. The launch frequency was $f = 41.1$ GHz and the cut-off position was calculated to be $\rho_{\mathrm{pol}} = 0.98$, around the minimum in E_r (see figure 1.5). The spectra of all antennas look similar and are without Doppler shift. Broadband fluctuations are observed up to 800 kHz, however, the actual width depends on the velocity of rotation. Assuming that the frequency of the fluctuations is connected with the perpendicular wavenumber as $k_\perp = 2\pi f / v_\perp$, leads to the wavenumber scale plotted in figure 5.12. The estimated perpendicular velocity $v_\perp = 4.5$ km/s from section 7.1.2 for discharge #32520 is used. The auto power

spectra decay to the A_0/e level at $k_\perp = 2.1$ cm^{-1}. This decay is due to a combination of the natural decay of the fluctuation power $E(k_\perp)$ with perpendicular wavenumber and the sensitivity of the PCR system $S(k_\perp)$ (see section 6.4.2).

To fully demonstrate the diagnostics potential the measured phase in the presence of strong edge localized magnetohydrodynamic (MHD) mode ($\rho_{pol} = 0.99$) is shown in figure 5.13. The phase have been calculated using equation 5.4, taking into account a phase unwrapping procedure (i.e. by correcting phase jumps). All antennas show a similar oscillation with a frequency of $f = 62$ kHz, but, the signals are shifted in time. The reason for the shift is the propagation of the mode in the electron diamagnetic direction. For the presented case the velocity of propagation is $v_\perp = 12$ km/s and the

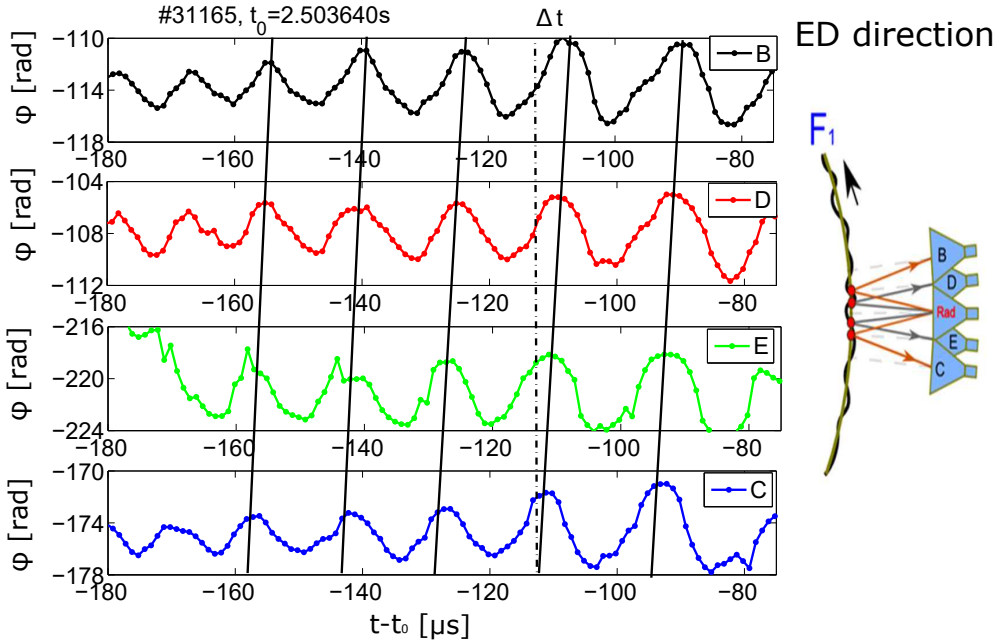

Figure 5.13: Modulation of the phase of different receiving antennas due to propagation of edge localized MHD modes in electron diamagnetic direction.

wavenumber of the mode $k_\perp = 0.3$ cm^{-1} have been estimated. The mode is observed not only in reflectometry data, but also in magnetic coils data and have been studied in [117].

6 Theory and correlation analysis techniques

This chapter describes the correlation analysis techniques applied to the PCR system. In section 6.1, cross-correlation in a turbulent field is discussed. A cross-correlation model is introduced, which links the measured cross-correlation fuction (CCF) to properties of turbulent eddies, such as the perpendicular propagation velocity $v_\perp = v_{E\times B} + v_{ph}$, the perpendicular correlation length $l_\perp$ and the decorrelation time τ_d. Section 6.2 shows CCF measurements between different antennas. The effect of the magnetic field line pitch angle α is discussed. The extraction of $v_\perp$ and α using Bayesian analyses of measured time delays is shown. The methods to measure $l_\perp$ and τ_d are presented as well. In section 6.3 the method to obtain the dispersion relation of fluctuations $k_\perp(f)$ using cross-phase estimation is shown. The last section 6.4, discusses the limitation of the PCR diagnostic related to the radial resolution and sensitivity of the system to poloidal wavenumbers k_θ.

6.1 Cross-correlation in turbulent field

A turbulent system displays variations in both space and time. To quantify how turbulent fluctuations at one location and one time correlate with those at another location and time the cross-correlation function (CCF) can be used. The CCF of the density fluctuating component about their mean value in turbulent fields is defined as [118]

$$\rho(\vec{\varepsilon},\tau) = \frac{\langle \delta n(\vec{r},t)\delta n(\vec{r}+\vec{\varepsilon},t+\tau)\rangle}{\sqrt{\langle \delta n^2(\vec{r},t)\rangle}\sqrt{\langle \delta n^2(\vec{r}+\vec{\varepsilon},t+\tau)\rangle}}\,, \tag{6.1}$$

where $\vec{\varepsilon}$ is a spatial separation vector and τ is a temporal separation. The methodology presented in this section is equally relevant for the study of turbulence in general turbulent flows or in the tokamak. Therefore, we first consider cross-correlation in the general turbulent field and then apply the results to turbulence in a tokamak.

6.1.1 Elliptic model

For simplicity only a one dimensional CCF $\rho(\varepsilon, \tau)$ with a separation vector $\vec{\varepsilon} = (\varepsilon, 0, 0)$ along the stream-wise component of the mean velocity $\vec{v} = (v, 0, 0)$ is considered. The

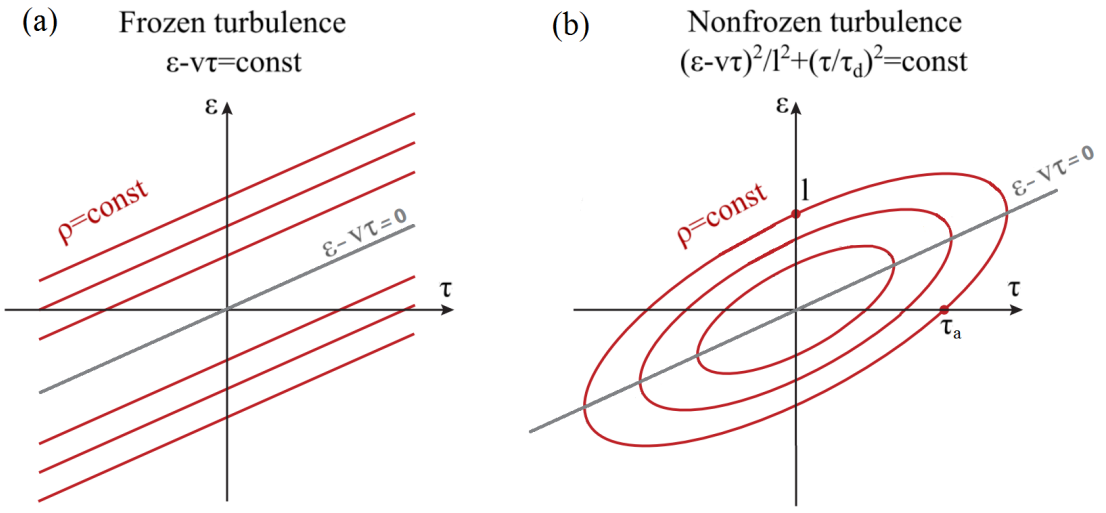

Figure 6.1: The isocorrelation countours $\rho(\varepsilon, \tau) = C$ for (a) the Taylor frozen model (pure convection of the eddies) and (b) the elliptic model (convection + distortion of the eddies).

first model of a CCF linking the spatial and temporal scales of the turbulent eddies has been proposed by Taylor [119, 120], where turbulent structures move in space with a convective velocity v without significant distortion. The one-dimensional CCF for this case has a simple translational symmetry

$$\rho(\varepsilon, \tau) = f(\varepsilon - v\tau). \tag{6.2}$$

Here the function f describes the shape of the CCF (e.g. Gaussian, Lorentzian or arbitrary). Such a model implies that the cross-correlation never decays on the characteristic line $(\varepsilon - v\tau)$. The schematic diagram for the isocorrelation contours $\rho(\varepsilon, \tau) = C$ of the Taylor CCF is shown in figure 6.1a. This model is applicable for small turbulent intensities (or small Reynold numbers), however it is broken at high intensities. Briggs [121] suggested to include an additionally distortion (or mutation) of the turbulence eddies during propagation with an effective decorrelation time τ_d. The CCF model using distortion of the eddies is called the elliptic model [122] and gives the CCF as

$$\rho(\varepsilon, \tau) = f\left(-\frac{(\varepsilon - v\tau)^2}{l^2} - \frac{\tau^2}{\tau_d^2}\right). \tag{6.3}$$

Here l is a correlation length (characteristic size of the eddies), τ_d is the decorrelation time (characteristic lifetime of the eddies) and v is the mean flow velocity. The isocorrelation contours have an elliptic shape as shown in figure 6.1b. For the case $\tau_d = \infty$ (no distortion) equation 6.3 reduces to the Taylor form (equation 6.2). The elliptical model was compared with numerical simulations of the Navier-Stokes equation [122, 123, 124] and shows good agreement. When the parameters v, l, τ_d and the shape of the CCF are known, the correlation of density fluctuations is fully described. The theoretical models for τ_d are presented in detail in section 8.2.3.

6.1.2 The CCF in tokamaks

To first order, the turbulent structures in a tokamak are expected to be strongly elongated in the direction of the helical magnetic field i.e. inclined to the toroidal direction. On a magnetic surface, turbulent eddies have two velocity components. One parallel to the magnetic field $v_{||}$ and one perpendicular to it composed of the $E \times B$ drift and the phase velocity of the turbulent structures $v_\perp(k_\perp) = E \times B / B^2 + v_{ph}(k_\perp)$ (see figure 6.2a), where $k_\perp$ is the perpendicular wavenumber. While propagating, the turbulent eddies additionally mutate with an effective decorrelation time τ_d. Adopting the elliptical approximation [121, 122, 123, 125] for the turbulence having a Gaussian distribution, both in space and time, the point cross-correlation on the magnetic surface can be expressed as

$$\rho(\varepsilon_\parallel, \varepsilon_\perp, \tau) = \exp\left(-\frac{(\varepsilon_\parallel - v_\parallel \tau)^2}{l_\parallel^2} - \frac{(\varepsilon_\perp - v_\perp \tau)^2}{l_\perp^2} - \frac{\tau^2}{\tau_d^2}\right). \tag{6.4}$$

Here $l_\parallel$ and $l_\perp$ denote the parallel and perpendicular fluctuation correlation lengths, $\varepsilon_\parallel$ and $\varepsilon_\perp$ the parallel and perpendicular separations between the measured volumes and τ the separation in time. The exponential shape of the CCF was selected because it is applicable to experimental results presented in this thesis. In principle both velocities, $v_\parallel$ and $v_\perp$, should be taken into account in the CCF. However, for comparable separations in parallel and perpendicular directions $\varepsilon_\perp \approx \varepsilon_\parallel$ the parallel velocity can be neglected when the following is met:

$$\gamma = \frac{v_{||}}{v_\perp} \frac{l_\perp}{l_{||}} \ll 1. \tag{6.5}$$

Condition (6.5) is fulfilled in toroidally confined plasmas due to the fact that the parallel correlation length of measured structures $l_{||}$ (several meters) [39, 40, 41, 42] is significantly longer than the perpendicular correlation length $l_\perp$ (some centimeters). This means that the parallel velocity can only affect the time delay measurements if $v_{||} > 10^2 v_\perp$. This is rarely the case for typical L-mode plasmas, however, possible where

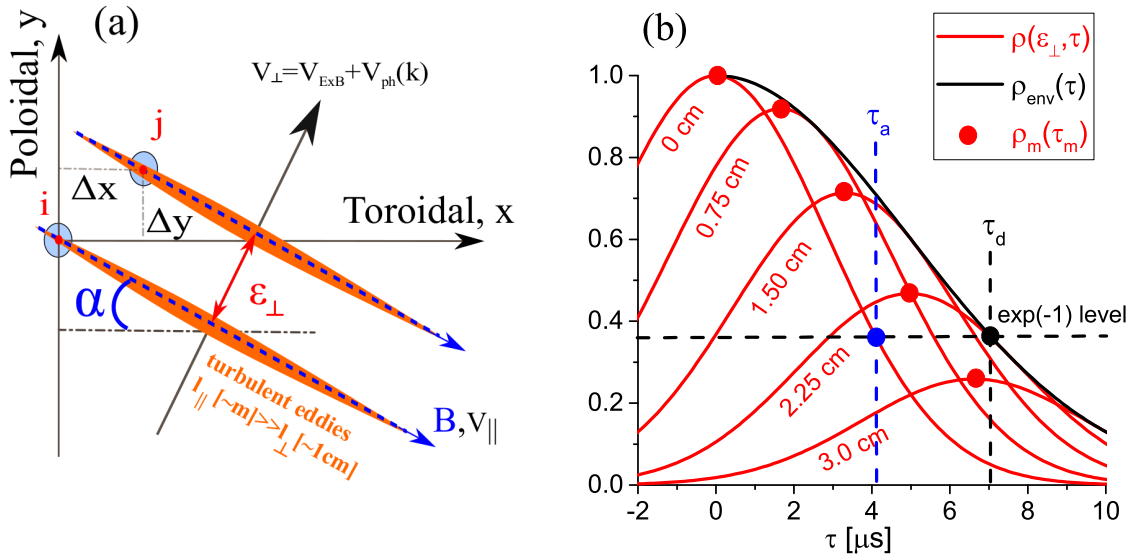

Figure 6.2: (a) Schematic representation of the cross-correlation between point i and j. Turbulent eddies (orange) aligned parallel to the magnetic field move in the perpendicular direction. (b) Cross-correlation function of density fluctuations for different perpendicular separations.

$v_\perp \approx 0$ (e.g. in the edge shear region, where $v_\perp$ changes sign). In the following analyses we neglect the parallel propagation. In this case the CCF simplifies to

$$\rho(\varepsilon_\perp, \tau) = \exp\left(-\frac{(\varepsilon_\perp - v_\perp \tau)^2}{l_\perp^2} - \frac{\tau^2}{\tau_d^2}\right). \tag{6.6}$$

The CCF from equation 6.6 is obtained for the case of a point cross-correlation, i.e. infinitesimal detection volume sizes. The real measurements always have a finite detection volume size l_s. This modifies the CCF to

$$\rho(\varepsilon_\perp, \tau) = \exp\left(-\frac{(\varepsilon_\perp - v_\perp \tau)^2}{l_{\text{eff}}^2} - \frac{\tau^2}{\tau_d^2}\right), \tag{6.7}$$

where the effective correlation length $l_{\text{eff}}^2 = l_\perp^2 + l_s^2$ includes the additional term l_s, related to the finite size of the detecting volume of the PCR (see section 6.4.2). In figure 6.2b an example of $\rho(\varepsilon_\perp, \tau)$ for different perpendicular separations is shown using typical values of $\tau_d = 7$ μs, $l_{\text{eff}} = 1.5$ cm and $v_\perp = 3$ km/s.

6.1.3 Time delay estimations

For the case of a gaussian CCF from equation 6.7 the peak correlation time delay τ_m between two detecting volumes

$$\tau_m(\varepsilon_\perp) = \arg\max_\tau(|\rho(\varepsilon_\perp, \tau)|) = \frac{\varepsilon_\perp}{v_\perp}\left(1 + \frac{l_{\text{eff}}^2}{v_\perp^2 \tau_d^2}\right)^{-1} \tag{6.8}$$

(red points in figure 6.2b) increases with the perpendicular separation $\varepsilon_\perp$, which depends on the selected antenna pairs and on the value of the magnetic field pitch angle α

$$\varepsilon_\perp(\Delta x, \Delta y, \alpha) = (\Delta y + \Delta x \tan(\alpha))\cos(\alpha). \tag{6.9}$$

Here Δx and Δy denote the separation between detecting volumes in the toroidal and poloidal directions, respectively (see figure 6.2a). It is important to note that the measurement of time delays τ_m are difficult when they exceed the decorrelation time τ_d of the turbulence due to the low level of correlation.

For the case of infinite decorrelation time $\tau_d = \infty$, a ratio of the time delay and the separation $\tau_m(\varepsilon_\perp)/\varepsilon_\perp$ depends only on the perpendicular velocity. However, for the case of a finite decorrelation time, this ratio is not only a function of $v_\perp$, but also depends on l_{eff} and τ_d. The perpendicular velocity can be extracted if the autocorrelation time τ_a, i.e. $\rho(0, \tau_a) = \rho(0, 0)/e$, and the decorrelation time τ_d (the decay of the envelope as indicated in figure 6.2b), i.e. $\rho_{\text{env}}(\tau_d) = \rho_{\text{env}}(0)/e$ are known. Using equation 6.7 the autocorrelation time is expressed as

$$\tau_a = \frac{(l_{\text{eff}}/v_\perp)\tau_d}{\sqrt{l_{\text{eff}}^2/v_\perp^2 + \tau_d^2}}. \tag{6.10}$$

Combining equations (6.8) and (6.10) the peak correlation time delay τ_m can be expressed via τ_a and τ_d as

$$\tau_m(\varepsilon_\perp) = \frac{\varepsilon_\perp}{v_\perp}\left(1 - \frac{\tau_a^2}{\tau_d^2}\right). \tag{6.11}$$

This relationship permits us to calculate the perpendicular velocity as

$$v_\perp = \frac{\varepsilon_\perp}{\tau_m(\varepsilon_\perp)}\left(1 - \frac{\tau_a^2}{\tau_d^2}\right). \tag{6.12}$$

Although, the autocorrelation time depends on l_{eff}, τ_d and $v_\perp$, both τ_a and τ_d can be measured experimentally, as shown in figure 6.2b (blue and black point). This measurement methodology is similar to one obtained by Briggs [121], which is applied to plasmas in [125]. Summarizing, $v_\perp$ can be measured from time delay analyses using this method when the following conditions are fulfilled:

1. If turbulent eddies are aligned in the direction of the magnetic field and the value of the magnetic field pitch angle α is known.
2. If the value of the peak correlation time delay τ_m between two measured volumes does not exceed the value of the decorrelation time τ_d of the turbulence i.e. $\tau_m < \tau_d$.
3. If the ratio of auto- and decorrelation time τ_a/τ_d can be calculated or neglected.

6.1.4 Magnetic field pitch angle extraction from time delay estimations

According to equations 6.9 and 6.11, for a given separation (Δx and Δy) the peak time delay τ_m is a function of the perpendicular velocity $v_\perp$, the magnetic field pitch angle α and the ratio τ_a/τ_d. The value of α depends on the current profile in the plasma and is not known a priori, which makes the $v_\perp$ measurements more complicated. However, applying a three-point correlation technique with different poloidal and toroidal separations or multi-point measurements, α and $v_\perp$ can be determined simultaneously. Moreover, the ratio of two time delays from two different separations does not depend on $v_\perp$ so α can be determined as

$$\begin{aligned} \frac{\tau_{mi}}{\tau_{mj}} \equiv \xi &= \frac{\Delta y_i + \Delta x_i \cdot \tan(\alpha)}{\Delta y_j + \Delta x_j \cdot \tan(\alpha)}, \\ \tan(\alpha) &= -\frac{\Delta y_i - \xi \cdot \Delta y_j}{\Delta x_i - \xi \cdot \Delta x_j}. \end{aligned} \tag{6.13}$$

Note that because the ratio ξ does not depend on $v_\perp$, the α estimation is not sensitive to the decorrelation time τ_d. α is a non-linear function of the ratio ξ, i.e. of two time delays. Using $\tan(\alpha) \approx \alpha$ for small angles we can approximate the errors in the α measurement as

$$\begin{aligned} \sigma_\alpha &= \sqrt{\left(\frac{\mathrm{d}\alpha}{\mathrm{d}\tau_{mi}} \cdot \sigma_{\tau_{mi}}\right)^2 + \left(\frac{\mathrm{d}\alpha}{\mathrm{d}\tau_{mj}} \cdot \sigma_{\tau_{mj}}\right)^2} \\ &= \sqrt{2}\frac{\sigma_{\tau_m}}{\tau_m}\frac{\Delta x_i \Delta y_j - \Delta y_i \Delta x_j}{(\Delta x_i - \xi \Delta x_j)^2}\xi. \end{aligned} \tag{6.14}$$

Here σ_{τ_m}/τ_m is the uncertainty in the time delay given in percent. The error in α depends on the time delay ratio ξ. Substituting ξ from equation 6.13 we obtain

$$\sigma_\alpha = \sqrt{2}\frac{\sigma_{\tau_m}}{\tau_m}\frac{(\Delta y_i + \Delta x_i \alpha)\,(\Delta y_j + \Delta x_j \alpha)}{(\Delta y_i \Delta x_j - \Delta x_i \Delta y_j)}. \tag{6.15}$$

The best resolution is achieved when one antenna combination is aligned with the magnetic field line and another is perpendicular to it. An interesting case is obtained when $\Delta x_i = -\Delta x_j = \Delta y_i = \Delta y_j$. For this case we obtain

$$\sigma_\alpha = \frac{\sqrt{2}}{2}\frac{\sigma_{\tau_m}}{\tau_m}(1-\alpha^2). \tag{6.16}$$

For a 5 % error in the time delay measurements we obtain about a 2° error (worst case) in the measurement of the angle, which still allows for a realistic reconstruction of the α profiles. However, the α error can be reduced further if more than 2 time delay measurements are available, as is demonstrated in section 6.2.4.

6.2 Measurements of the CCF

This section presents measurements of the cross-correlation function using different antennas of the PCR. The methods to obtain the perpendicular velocity $v_\perp$, magnetic field pitch angle α, effective correlation length $l_{\text{eff}} = \sqrt{l_\perp^2 + l_s^2}$ and decorrelation time τ_d using the CCF are shown as well.

6.2.1 Position of measurements from beam tracing code TORBEAM

To correlate signals from poloidally and toroidally separated antennas, the precise positions of the reflection volumes need to be known. The poloidal and toroidal measurement positions are not a fixed function of the radius, but depend on the cut-off layer curvature (poloidal R_{pol} and toroidal R_{tor}) and the shape of the magnetic surface (e.g. vertical and horizontal shift of the plasma column).

At TEXTOR a simple calculation based on a circular poloidal cross-section of the iso-density surface was sufficient to obtain the reflection positions [115]. However, the D-shaped poloidal cross-section of AUG requires a more sophisticated approach. Here, the beam tracing code TORBEAM [126] is used with the real geometry of AUG plasma and antennas, together with fitted electron density profiles and the magnetic equilibria from the CLISTE code [76]. The radiation patterns of the launch/receiving antennas have a sufficiently wide beam width (spot overlap) that an optimal ray exists that passes from the centre of the launch antenna orifice to each of the receive antennas. The $\Delta\theta_{3dB}$ half power beam width of the antennas varies between 16 and 32° depending on frequency (see appendix A). The optimal ray (and hence reflection position) is found by tracing a set of rays with different angles within the launch radiation pattern. Figure 6.3 shows an example of the ray-tracing calculation for the conditions of discharge

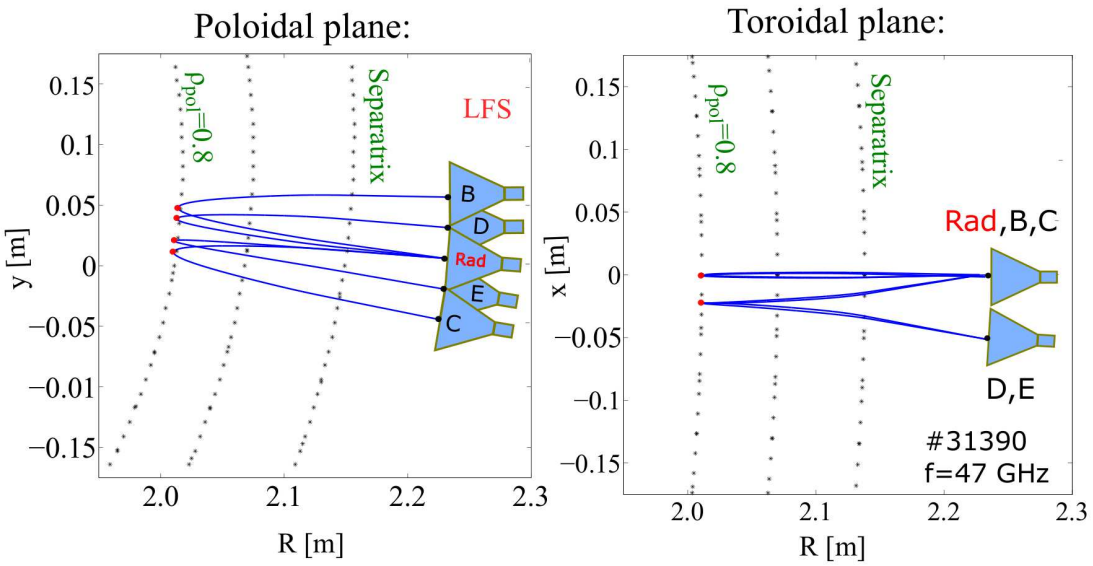

Figure 6.3: Examples of ray traces starting from the launch antenna (Rad), propagating to the reflection/cut-off layer and then to the receiving antennas (B, C, D, E). Red points correspond to the reflection point.

#31390 and a probing frequency of $f = 47$ GHz. The turning points of the reflected rays (red bold points) define the measurement positions for each antenna pair. At $\rho_{\mathrm{pol}} \simeq 0.8$ and a typical plasma geometry the separation between points amounts to $\Delta y = (10.4, 20.3, 30.5, 40.7)$ mm in the poloidal direction and $\Delta x = (0, 24.9)$ mm in the toroidal direction. As will be shown in section 6.4.2 the ray tracing reflection position is close to the expected detection volume position obtained using Born approximation.

The separations are investigated as a function of different cut-off radii, different plasma densities and different magnetic configurations. In figure 6.4 the poloidal and toroidal separations are shown for two discharges with different line averaged densities (LSN, positive I_p and negative B_T). For the line averaged density $\bar{n} = 1.5 \times 10^{19}$ m^{-3}, (figure 6.4a), ray-tracing has been performed using frequencies from 27 GHz at $\rho_{\mathrm{pol}} = 0.96$ to 38.6 GHz at $\rho_{\mathrm{pol}} = 0.4$. A strong dependence of the poloidal separation with ρ_{pol} is observed, which can be explained by a large change in the poloidal curvature R_{pol}. However, the toroidal dependence is weak, due to a small change in the toroidal curvature R_{tor} across ρ_{pol}. A comparison of the separations at higher density $\bar{n} = 3.1 \times 10^{19}$ m^{-3}, shown in figure 6.4b, yields similar results, despite the fact that the probing frequencies are different, starting from 31 GHz at $\rho_{\mathrm{pol}} = 0.98$ to 56.3 GHz at $\rho_{\mathrm{pol}} = 0.4$. This suggests that the effect of the frequency is small and that the main dependence comes from the curvature of the magnetic surfaces. In addition the effect of a vertical shift

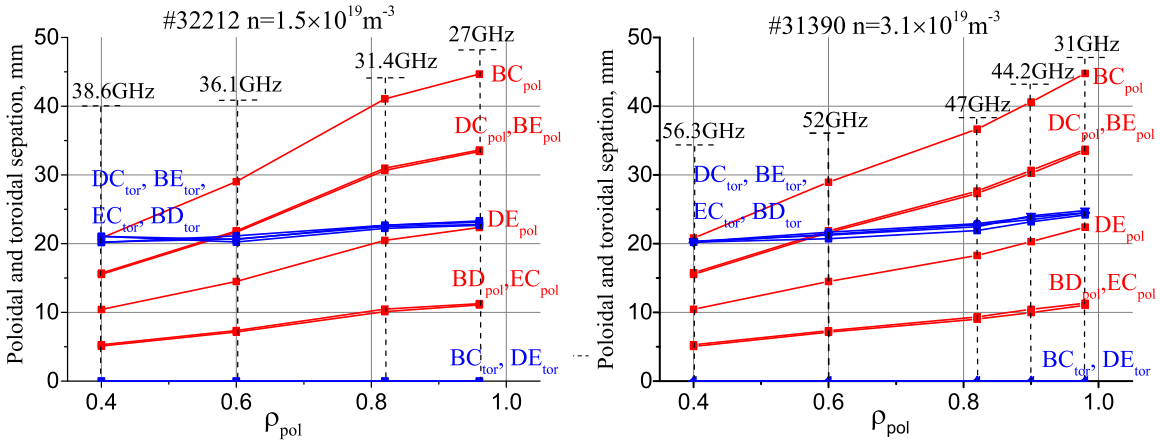

Figure 6.4: Comparison of poloidal (red) and toroidal (blue) separations between the measurement points of different horn antennas (B, C, D, E) for two discharges with different densities. To have the same reflection layer the launch frequency was changed.

of the plasma is studied in the range of ±25 mm. Only a very weak change in the poloidal and toroidal separations in the order of 2 % is found which does not exceed the measurement error.

6.2.2 Experimental CCF between different antennas

For two discrete signals X and Y the CCF is expressed as

$$\rho_{XY}(\tau) = \frac{\langle X \cdot Y^{\star} \rangle}{\sqrt{\langle |X|^2 \rangle \langle |Y|^2 \rangle}}. \tag{6.17}$$

Here X and Y are either complex signals $A(t)e^{i\phi(t)}$, or complex phase signals $e^{i\phi(t)}$, or amplitude signals $A(t)$, or phase signals $\phi(t)$ from arbitrary antennas of the PCR. Figure 6.5 shows a comparison between the CCF for each type of signal of antenna combinations EC & DC from discharge #32520. The signals were filtered in the range 2–750 kHz before calculation of the CCF. This is necessary in order to remove the DC component of the signals and high frequency noise, which sometimes is observed. The correlation level for the complex phase $e^{i\phi(t)}$ (blue dotted line) is higher than for the amplitude $A(t)$ (red dotted line) indicating that phase information is more important. Note, that if a numerical algorithm for the phase unwrapping of complex signal is applied, then signals do not correlate anymore (see green line in figure 6.5). Independent of signal type, the peak correlation time delay

$$\tau_m = \arg\max(|\, \rho_{XY}(\tau)\, |) \tag{6.18}$$

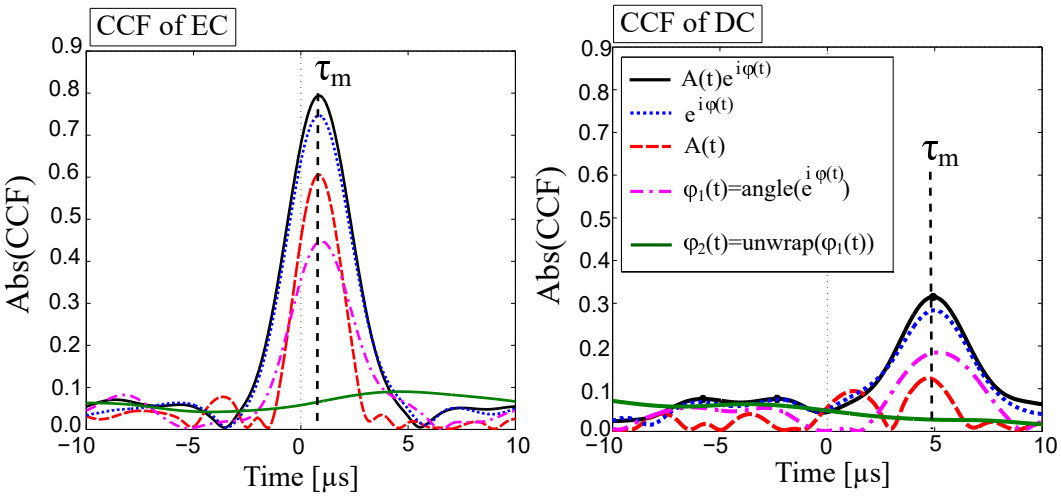

Figure 6.5: Comparison of the CCF for complex signal (black), complex phase (blue), amplitude (red), phase (magenta) and unwrapped phase (green) for two antenna pair combinations EC and DC.

is the same. From now on we consider results derived from the complex signal only.

Figure 6.6a depicts all possible CCFs for AUG discharge #32843 at $t = 3.31\,\mathrm{s}$ within a time windows of 5 ms. The CCF indeed varies with the antenna pair separation. All individual CCFs can be fitted with a Gaussian function $\rho_m \exp(-(\tau - \tau_m)^2/\tau_w^2)$ (figure 6.6b). Not only the peak correlation time delay τ_m, but also the peak correlation level ρ_m varies with the antenna pair separation (figure 6.6a). The reason is the decorrelation of the turbulence during its propagation (section 6.1.2). One can describe

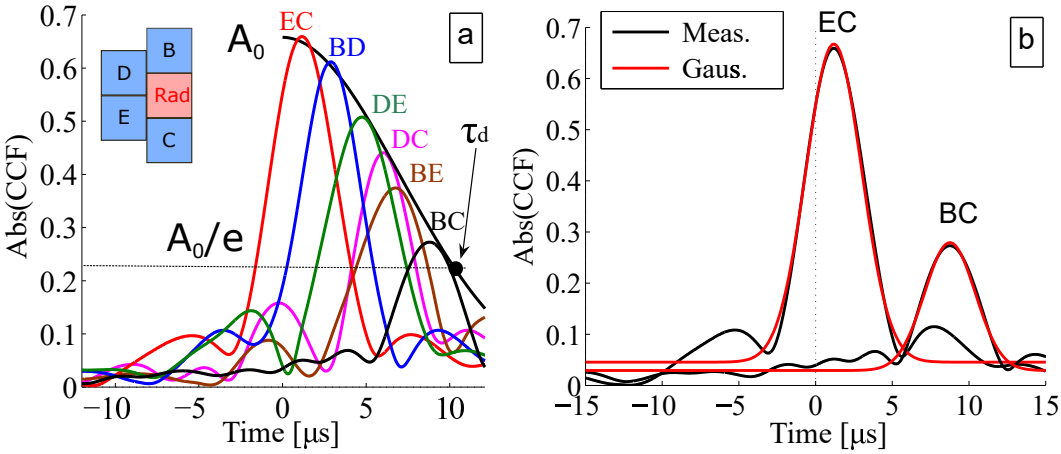

Figure 6.6: (a) Cross-correlation function for various antenna pair combinations. (b) Fit of two experimental CCFs (black) with the Gaussian function (red).

the decorrelation effect by an envelope $\rho_0 \exp(-\tau^2/\tau_d^2)$ with a certain decorrelation time τ_d as shown in figure 6.6a for the presented case of 10.5 μs. However, the obtained τ_d depends on plasma parameters. The correlation level at zero time delay ρ_0 is not always unity. This is due to the presence of an uncorrelated signal (noise) in the data as for example due to noise in the IQ detectors. This contribution does not affect the measurement because it equally affects all antenna pair combinations since they have the same electronics.

In figure 6.7 the peak correlation time delay τ_m depends on the selected antenna pair. Different τ_m are obtained for such antenna pair combinations with different toroidal signs $\Delta x_i = -\Delta x_j$ but equal poloidal signs $\Delta y_i = \Delta y_j$ (here i and j stands for different antenna pair combinations). The reason for this difference has its origin in the pitch angle α. In figure 6.7 the τ_m values are shown as a function of the poloidal separation Δy

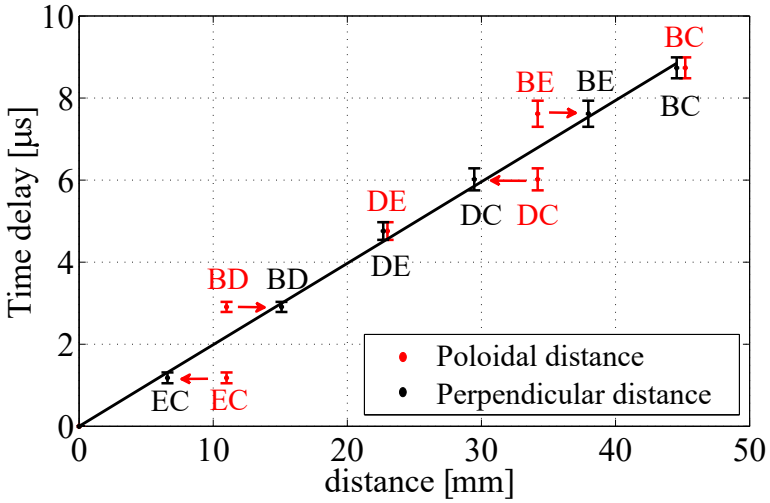

Figure 6.7: Time delay τ_m as a function of poloidal (red) and perpendicular separation (black). The value of magnetic field pitch angle is 9.5°

(red points) and as a function of the perpendicular separation $\varepsilon_\perp$ (black points). Here $\varepsilon_\perp$ denotes the separation of the reflections perpendicular to $\vec{B}$ according to equation 6.9. Assuming a constant perpendicular velocity $v_\perp$ the deviation from the linear regression fit (line) with the poloidal separation values (red) is due to an inclination angle. This angle is, to first order, the magnetic pitch angle α. This deviation disappears when plotting the time delay as a function of the perpendicular separation (black points), calculated using equation 6.9.

6.2.3 The fixed and stepping frequency measurements of CCFs

In this thesis two regimes of operation of the PCR were used. In the first regime the frequency of the U- and Ka-band were kept fixed during the whole discharge.

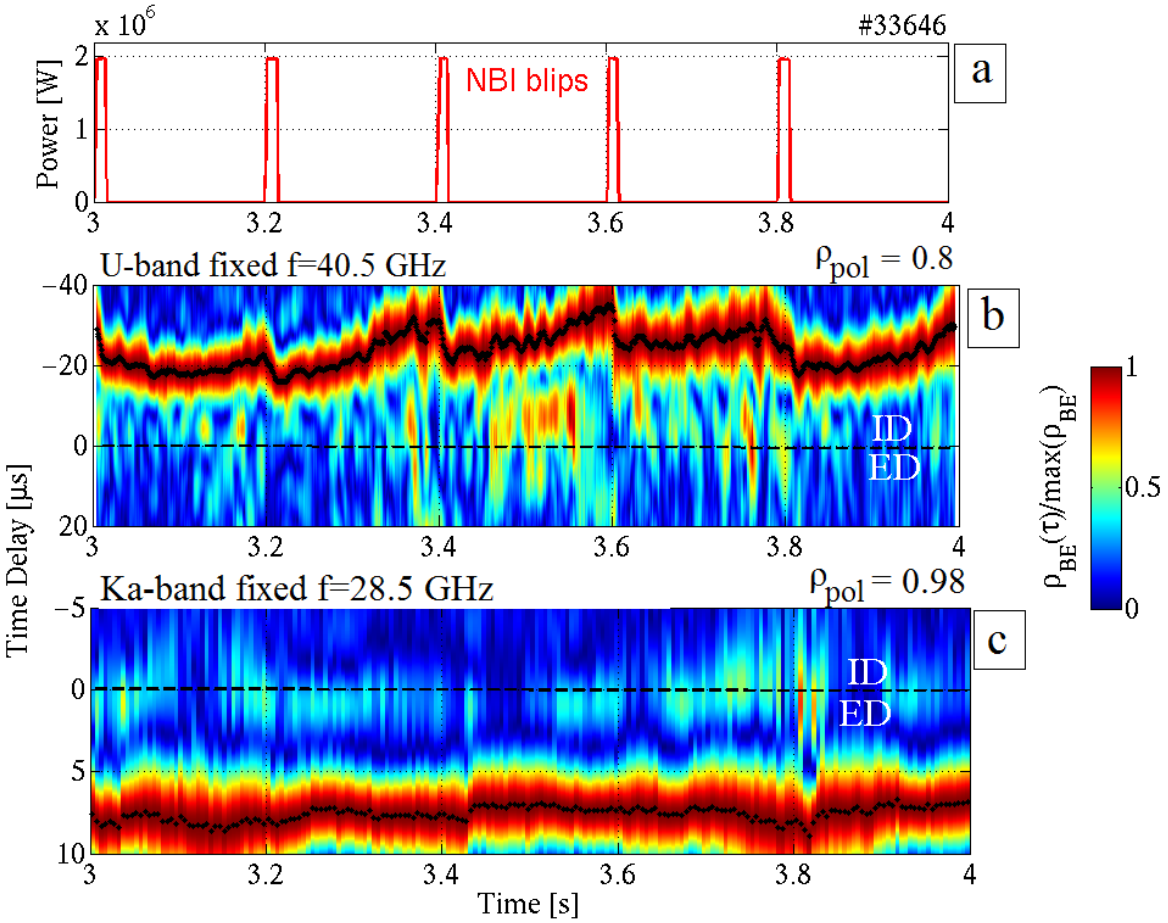

Figure 6.8: Fixed frequency measurements of the PCR for the discharge #33646. Short NBI blips (a) every 200 ms are applied. Normalized CCFs for combination BE of the U-Band at ρ_{pol}=0.8 (b) and Ka-Band at ρ_{pol}=0.98 (c).

An example of simultaneous measurements of the normalized CCF $\rho_{BE}(\tau)/\max_{\tau}(\rho_{BE})$ with the U-band (40.5 GHz) and Ka-band (28.5 GHz) for antenna combination BE is shown in figure 6.8. The CCFs are calculated with a 5 ms sliding window without overlap. The U-band system has a cut-off position at $\rho_{\mathrm{pol}} = 0.8$, while the Ka-band has a cut-off position at $\rho_{\mathrm{pol}} = 0.98$. A clear time delay is observed for both cases, which changes over time. The time delay has a different sign at $\rho_{\mathrm{pol}} = 0.8$ and $\rho_{\mathrm{pol}} = 0.98$

related to fact that $v_\perp$ has different signs at these radii as well. The time delay at $\rho_{\mathrm{pol}} = 0.8$ is affected by applied NBI blips (figure 6.8a), where every blip decreases the time delay (i.e. increases $v_\perp$ in the ion diamagnetic direction). The NBI blips do not affect the rotation at the edge $\rho_{\mathrm{pol}} = 0.98$ of the plasma. Fixed frequency operation has been used when the evolution of CCFs at a fixed radius was investigated.

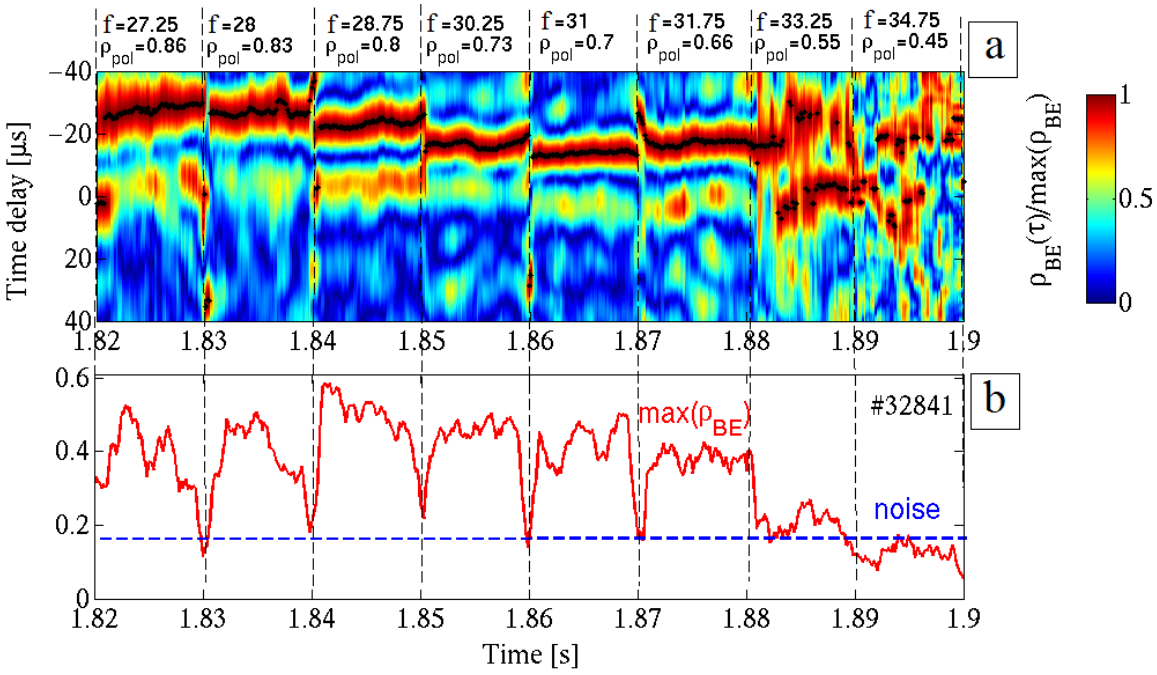

Figure 6.9: Stepping frequency measurements of the PCR for the discharge #32841. The frequency was changed every 10 ms. (a) Normalized CCF for the BE combination of the Ka-band. (b) Peak correlation level max(ρ_{BE}).

For the investigation of the radial dependence of the CCF, the system is operated in a frequency stepping regime. For this case the frequency is kept constant for a short duration and than changed to the next value. A typical program is shown in figure 5.8. A duration of 10 ms is enough to obtain a statistically significant CCF. An example of a measurement during stepping operation is shown in figure 6.9a for discharge #32841. The plasma parameters during the sweep are nearly constant. The CCF is calculated with 2 ms sliding window with 1.8 ms overlap. Above the upper trace in the figure 6.9 are the frequencies and corresponding radial positions in the plasma. The time delay exhibits a clear dependence on the radial position. This appears because of both the separation and velocity dependence on plasma radius. Figure 6.9b shows the maximal correlation level for the combination BE. The correlation level drops during a frequency

change due to the delay of the synthesizers locking. For deeper positions $\rho_{\mathrm{pol}} < 0.5$ the correlation level is low. The measurements of the CCF for this region of the plasma is difficult.

6.2.4 Measurements of $v_\perp$ and α using a Bayesian approach

$N = 4$ antennas permit the estimation of $M = N(N-1)/2 = 6$ different time delays (see figure 6.7), which can be used for the measurement of $v_\perp$ and α. To minimize the error, a multi-point analysis of all possible measurement pairs is used with a Bayesian approach. The main benefit of this method that it can estimate the probability to have a specific α and $v_\perp$ from the M measured time delays. It is assumed that the measured time delays follow a normal distribution with mean τ_m, and variance σ_{τ_m}. The variance can be evaluated from successive measurements of the time delay for any combination. The Bayesian probability to obtain a specific α and a specific $v_\perp$ from M time delays is defined as

$$P(v_\perp, \alpha | \tau_{mi}, \sigma_{\tau_{mi}}) = \prod_{i=1}^{M} \frac{P(\tau_{mi}, \sigma_{\tau_{mi}} | v_\perp, \alpha) \cdot p(v_\perp, \alpha)}{p(\tau_{mi}, \sigma_{\tau_{mi}})}. \tag{6.19}$$

The prior probability $p(v_\perp, \alpha)$ is assumed equally distributed over some range of velocities and angles. The probability of the measurement $p(\tau_{mi}, \sigma_{\tau_{mi}})$ does not depend on $v_\perp$ and α and therefore can be used as a normalization factor. The likelihood $P(\tau_{mi}, \sigma_{\tau_{mi}} | v_\perp, \alpha) = \exp(-(\tau_{mi} - \tau(v_\perp, \alpha))^2 / \sigma^2_{\tau_{mi}})$ describes the probability to measure a time delay τ_{mi} if the real velocity is $v_\perp$ and the real pitch angle is α. The analytic

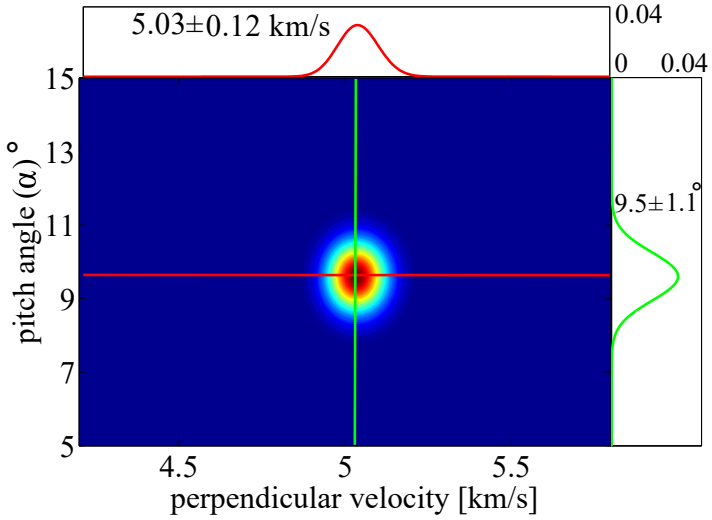

Figure 6.10: Bayesian probability function for discharge #32843 at $t = 3.31\,\mathrm{s}$.

function $\tau(v_\perp, \alpha)$ is obtained from geometry using equations (6.9) and (6.11), however, neglecting the factor τ_a/τ_d. The correction $(1-\tau_a^2/\tau_d^2)$ is taken into account after the Bayesian probability calculation.

An example of a calculation of Bayesian probability distribution function using time delays of the PCR system (see figure 6.7) is shown in figure 6.10. The centre of gravity of the spot represents the most probable values for the pitch angle α and the perpendicular velocity $v_\perp$. Error bars are estimated from the $1/e$ probability level in $v_\perp$ and α accordingly.

6.2.5 Measurements of effective correlation length l_{eff}

In the following, two methods are proposed to obtain the effective correlation length $l_{\text{eff}} = \sqrt{l_\perp^2 + l_s^2}$. The first method uses a e^{-1} separation of the CCF i.e. $\rho(l_{\text{eff}}, 0) = \rho(0,0)/e$. This method requires detailed measurements of the CCF as function of the perpendicular separation $\varepsilon_\perp$. The minimal separation between reflection volumes of the PCR system at $\rho_{\text{pol}} = 0.8$–1.0 is $\varepsilon_\perp \approx 0.7$–$1.1$ cm. Measurements of l_{eff} smaller than 1 cm are difficult with such an approach. Figure 6.11a shows the application of the method to discharge #30777 at $t = 3.8$ s. Already the shortest combination shows a significantly reduced correlation level. Other values are on the noise level. Fitting the Gaussian function with only a single point is difficult and produces large error bars. Nevertheless, the value of the effective correlation length was calculated to be

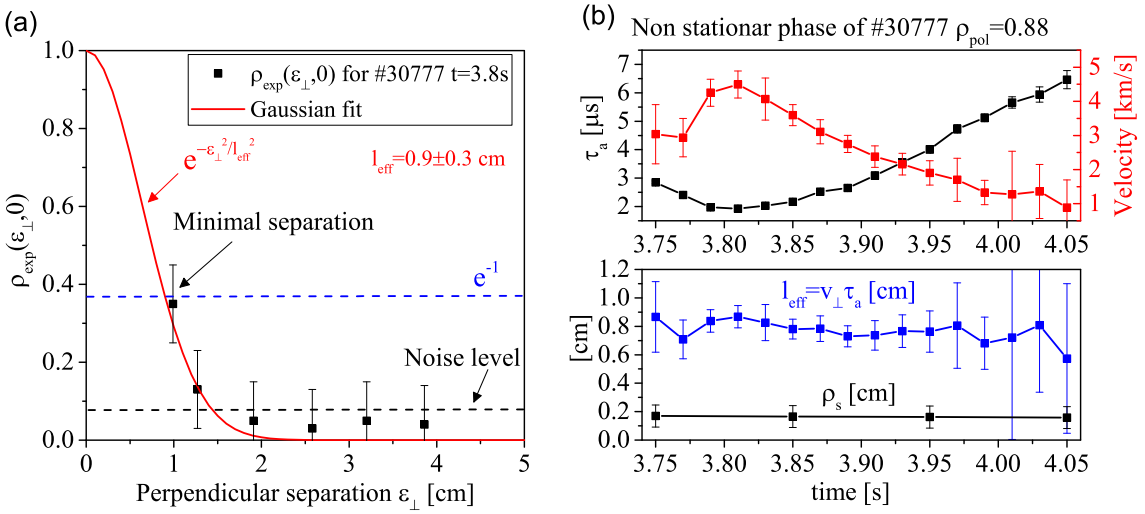

Figure 6.11: Measurement of the effective correlation length l_{eff} (a) from the cross-correlation at zero time delay and (b) using the relationship $l_{\text{eff}} \approx v_\perp \tau_a$. Both methods give similar effective correlation length values.

$l_{\text{eff}} = 0.9 \pm 0.3$ cm using this approach.

The second method is based on measurements of the autocorrelation time $\rho(0, \tau_a) = \rho(0,0)/e$. The effective correlation length is obtained by inverting equation 6.10:

$$l_{\text{eff}} = \frac{v_\perp \tau_a}{\sqrt{1 - \tau_a^2/\tau_d^2}}. \tag{6.20}$$

Equation 6.20 can be simplified if $\tau_a \ll \tau_d$ (which is typically the case for the analyzed discharges[1]), giving $l_{\text{eff}} = v_\perp \tau_a$. If $v_\perp$ and τ_a are measured simultaneously the effective correlation length can be calculated. The velocity is obtained using time delay analyses. Figure 6.11b shows measurements of $l_{\text{eff}} = v_\perp \tau_a$ using this method for the same discharge #30777. The analyzed time period is not stationary and the velocity (red line) changes over time at the same position. The autocorrelation time (black line) also changes over time, however, the effective correlation length $l_{\text{eff}} = v_\perp \tau_a$ (blue line) stays nearly constant independent of the velocity. It is important to note that this value of the effective correlation length is comparable to that from the previous method. In further analyses the second method is used, since it gives smaller error bars.

6.2.6 Measurements of decorrelation time τ_d

In figure 6.12 the peak correlation level ρ_m is plotted as function of the peak correlation time delay τ_m (see figure 6.6a) for different antenna combinations. The measurements are shown for two positions $\rho_{\text{pol}} = 0.75$ and 0.98. ρ_m decreases with τ_m due to the decorrelation of the turbulence while propagating. The exponential fit $\rho_m(\tau_m) = \rho_0 \exp(-\tau_m^2/\tau_{dm}^2)$ (blue and red curves) permits one to estimate τ_{dm} which can be used as an approximation for the decorrelation time τ_d. The measured τ_{dm} is slightly smaller than the real τ_d

$$\tau_{dm}^2 = \tau_d^2 - \tau_a^2. \tag{6.21}$$

Equation 6.21 is obtained using equation 6.8 for τ_m and equation 6.10 for τ_a. For the case when $\tau_a \ll \tau_d$ (which is typically the case for the analyzed discharges[1]) the difference is very small. In the following analyses it is assumed that $\tau_{dm} \approx \tau_d$. In figure 6.12 one can see that decorrelation time at $\rho_{\text{pol}} = 0.75$ (red curve) is longer than at $\rho_{\text{pol}} = 0.98$ (blue curve). These observations are discussed in chapter 8.

It is important to discuss if the envelope can appear as diagnostic effect. In appendix B simulations of the CCF in Born approximation between separated antennas show that in the absence of a decorrelation process (purely propagation of synthetic turbulent density fluctuations) the peak cross-correlation level is close to one. This suggest that

[1] In the analyzed discharges the autocorrelation time (see equation 6.10) is approximately equal to the propagation time crossing the measured volume which is shorter than τ_d.

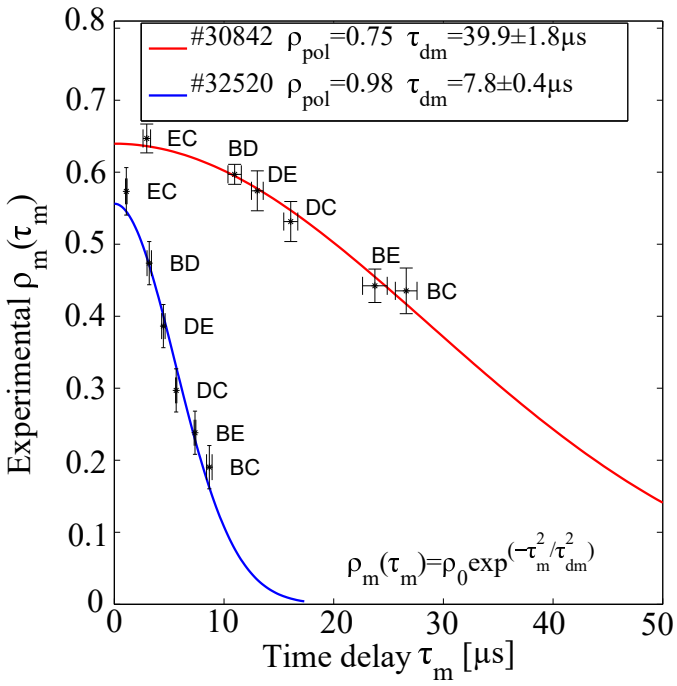

Figure 6.12: The experimental fit through the peaks of CCFs $\rho_m(\tau_m)$ for the core and the edge of AUG. Eddies in the core live longer than in the edge.

the observed envelope is due to decorrelation of the turbulence and not a diagnostic effect. This significantly simplifies the interpretation of τ_d measurements compared to l_{eff}, which additionally includes the detection volume size.

6.3 Estimation of the dispersion relation

This section introduces a technique to determine the dispersion relation $k_\perp(f)$ of propagating waves in dispersive media [127]. The method is based on the estimation of the spectral coherence $G_{XY}(f)$ between two separated measurements X and Y

$$G_{XY}(f) = \frac{\langle X(f)Y^*(f)\rangle}{|\langle X(f)\rangle|\,|\langle Y(f)\rangle|} = \gamma(f)e^{i\Delta\phi(f)}. \tag{6.22}$$

Here X and Y are Fourier signals of density fluctuations. The spectral coherence can be decomposed into the coherence amplitude $\gamma(f) = |G_{XY}(f)|$ and the cross-phase $\Delta\phi(f) = \text{atan}(G_{XY}(f))$. $\gamma(f)$ ranges from 0 to 1. It is equal to 1 when the spectral components of the signals are identical and shifted only in time. The cross-phase $\Delta\phi(f)$ gives information on the perpendicular wavenumber which corresponds to the frequency

f (i.e. the dispersion relation) [127]

$$k_\perp(f) = \frac{\Delta\phi(f)}{\varepsilon_\perp}. \tag{6.23}$$

The velocity of propagating waves is determined from the cross-phase as

$$v_\perp(k_\perp) = \frac{2\pi f}{k_\perp} = 2\pi\varepsilon_\perp \left(\frac{\Delta\phi(f)}{f}\right)^{-1}. \tag{6.24}$$

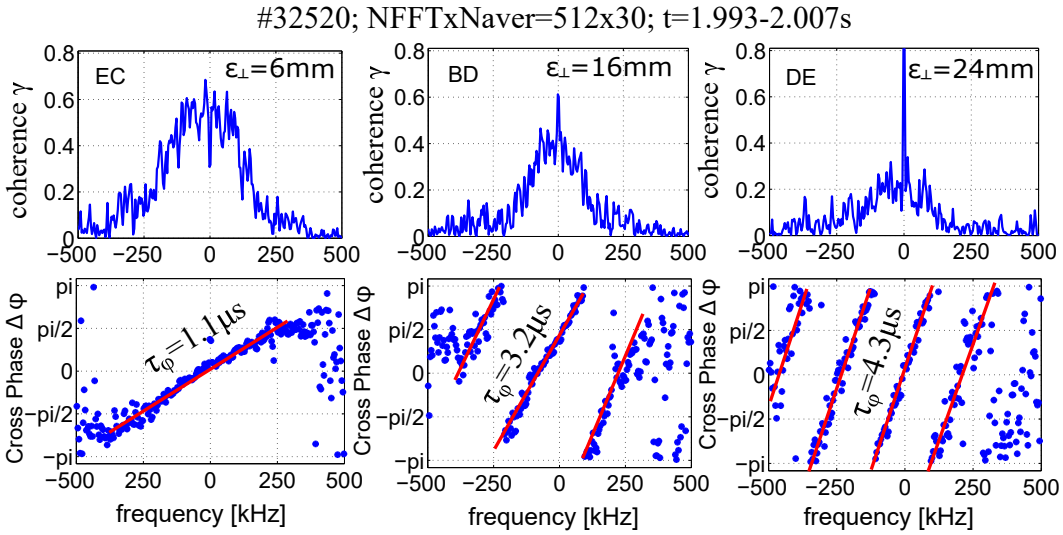

Figure 6.13: The spectral coherence amplitude $\gamma(f)$ and cross-phase $\Delta\phi(f)$ for 3 different perpendicular separations of #32520.

Figure 6.13 shows the coherence amplitude $\gamma(f)$ and cross-phase $\Delta\phi(f)$ measured for 3 different antenna separations from discharge #32520 at $\rho_{\mathrm{pol}} = 0.98$. The spectral coherence is calculated from 512 points and averaged for 30 non-overlapping windows. The separations perpendicular to the magnetic field $\varepsilon_\perp$ for these combinations are calculated using equation 6.9. The cross-phase spectra $\Delta\phi(f)$ have constant slopes indicating that the dispersion relation is linear for the measured frequency range. For the shortest distance ($\varepsilon_\perp \approx 6$ mm) a high coherence amplitude $\gamma(f)$ and a small cross-phase slope $\Delta\phi(f)$ is observed. With the increase of the separation the slope of the cross-phase $\Delta\phi(f)$ increases because more time is needed for the propagation from one reflection point to the other. The coherence amplitude $\gamma(f)$ decreases with the separation. The study of the dispersion relation in the edge of AUG is performed in the section 7.1.2.

6.4 Resolution of the measurements

6.4.1 Radial resolution

The radial resolution of the PCR diagnostic has been approximated by the full-width half-maximum of the first Airy lobe of the microwave squared electric field E^2 at the cut-off layer. For O-mode polarization with a moderate density gradient scale length $L_n = |\nabla \log(n)|^{-1}$ this is given by [78]

$$\delta R = \frac{1.6 L_n}{[(\omega/c) L_n]^{2/3}} \tag{6.25}$$

where $\omega = \omega_{pl}(n_e)$ is estimated from the density profile at the reflection position. The typical radial resolution is of the order of 2–12 mm depending on the density and probing frequency. It is of interest that the resolution improves at the edge due to decreasing L_n and reaches values in the range 2–4 mm. Note, however, that the radial resolution of the method can deteriorate due to small angle scattering of the microwaves [81, 83].

6.4.2 Sensitivity to poloidal wavenumbers and poloidal resolution

Small structures can only be detected, if the reflection volume is small enough. Otherwise, averaging of the density fluctuations over the reflection volume occurs. Here, the parameter of interest is the sensitivity of the PCR to different poloidal wavenumbers $I^2_{k_\theta} = S(k_\theta)\delta n^2_{k_\theta}$, where I_{k_θ} is the amplitude of the measured signal for density fluctuations with a poloidal wavenumber k_θ. To obtain the sensitivity function $S(k_\theta)$, a full-wave simulation can be used that takes into account density fluctuations. Such a calculation of $S(k_\theta)$ has been performed e.g. for Alcator C-mod [128] and TEXTOR [129].

For AUG the sensistivity function $S(k_\theta)$ is obtained in Born approximation only. According to section 4.2 the response in the measured signal by the IQ detector is given by equation 4.11 with a complex weighting function from equation 4.12. The Born approximation gives a reasonable estimate of the signal only for small density fluctuation levels $\delta n/n < 1$–$4\,\%$ (calculated using equation 4.10). On AUG equation 4.11 is analyzed in the case of a bistatic configuration. The combination Rad-B (see figure 6.3) is considered only, however, any pair combination can be used. The unperturbed full-wave distributions of transmitting antenna E_t and receiving antenna E_r are found with the microwave code developed in [130] using a cylindrical coordinate system. Figure 6.14a shows magnetic surfaces from the CLISTE code (red dots) and approximated

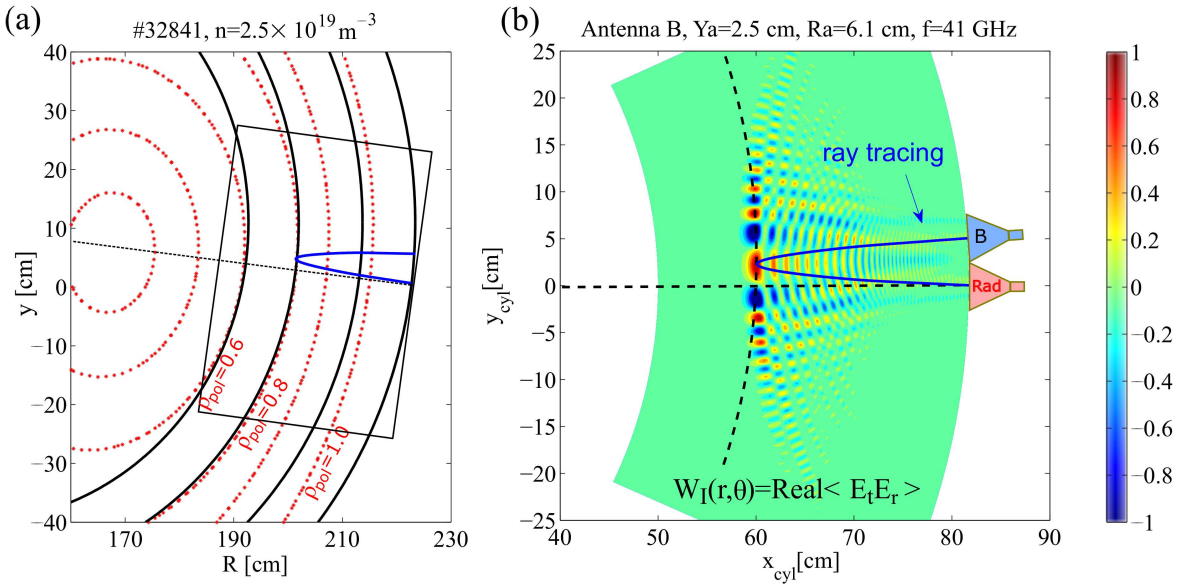

Figure 6.14: (a) Approximation of magnetic surfaces from CLISTE code by cylindrical surfaces. (b) Calculation of real part of weight function $W_{IB} = \text{real}\langle E_t(\vec{r},t)E_r(\vec{r},t)\rangle$ in cylindrical coordinates for the case of bistatic configuration.

cylindrical surfaces (black lines). It is assumed that the density $n_e(r)$ is constant on such cylindrical surface. The experimental density profile has been projected onto cylindrical coordinates. The blue curve shows a ray tracing calculation for the case of $f = 41$ GHz and the combination Rad-B. The black frame denotes the region where calculations of E_t and E_r is performed. The electric field in the antenna mouth is assumed close to the actual field distribution in the horn of a microwave antenna in the H-plane (see appendix A). As an example the real part of the weight function $W_{IB}(r,\theta)$ for the in-phase signal $I(t)$ is shown in figure 6.14b. Discharge #32841 is used for the density profile. The ray tracing calculation is also plotted in the figure. One can see that the reflection point of the ray tracing is close to the actual maximum of $W_I(r,\theta)$.

In order to obtain the sensitivity function $S(k_\theta)$ the responses of $I(t)$ and $Q(t)$ in the presence of rotating density fluctuations

$$\delta n(r,\theta,t) = \cos(m\theta - \omega_\theta t)\exp(-\frac{(r-r_0)^2}{(\Delta r/2)^2}) \tag{6.26}$$

have been investigated at different radii r_0. Here $m = k_\theta r$ is the poloidal wavenumber and ω_θ the angular frequency of density fluctuations. The radial size of the fluctuations is assumed to be $\Delta r = 1$ cm. The square of the maximal response of the IQ detectors is used as an estimate for the sensitivity function $S(k_\theta = m/r) = \left\langle \max(I(t))^2 + \max(Q(t))^2 \right\rangle$. The example of the normalized $S(k_\theta)$ for the conditions of discharge #32841 and

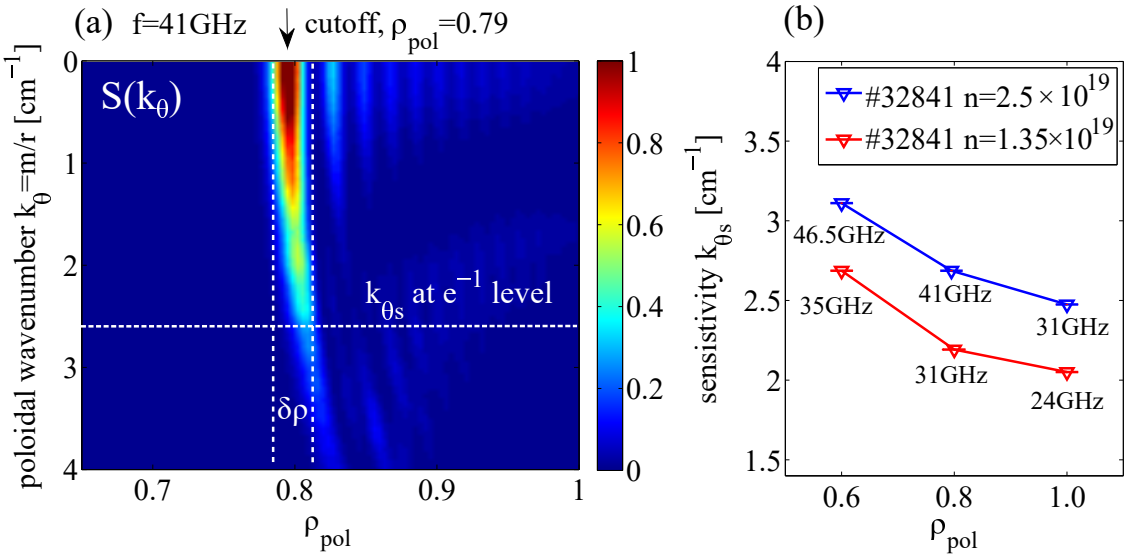

Figure 6.15: (a) Sensitivity of the PCR $S(k_\theta)$ to different poloidal wavenumbers k_θ and radial positions ρ_{pol} in Born scattering approximation. (b) Comparison sensitivity $k_{\theta s}$ at e^{-1} level, i.e. $S(k_{\theta s}) = S(k_\theta)/e$, for different radial positions and frequencies.

frequency $f = 41$ GHz is shown in figure 6.15a. As expected, the system is most sensitive at the cut-off layer. The sensitivity at the e^{-1} level[1] is calculated to $k_{\theta s} = 2.7$ cm^{-1}. This estimate is similar to the full wave estimate for TEXTOR [129] with similar antenna geometry.

The dependence of the sensitivity $k_{\theta s}$ at the e^{-1} level is investigated as a function of radial position and frequency. Figure 6.15b shows the dependence of $k_{\theta s}$ on the radial position for the discharge #32841 at line average density of $\bar{n} = 2.5 \times 10^{19}$ m^{-3} (blue curve). The sensitivity improves towards the core. This can be explained by a decreasing cut-off curvature radius. The comparison to the smaller density case $\bar{n} = 1.35 \times 10^{19}$ m^{-3} (red curve) shows that at a fixed radial position the sensitivity improves with frequency. In further analyses it is assumed that the sensitivity to perpendicular wavenumbers is similar, i.e. $k_{\perp s} \approx k_{\theta s}$.

The poloidal resolution in real space can be roughly approximated as $l_s = 2/k_{\theta s}$. For the results from figure 6.15a this is approximately 0.75 cm. The effect of finite $k_{\theta s}$ on the measured effective correlation length l_{eff} is shown in appendix B. The conclusion is that poloidal/perpendicular correlation lengths smaller than the sensitivity length which is of the order of 0.6–0.8 cm for AUG cannot be measured with the PCR system.

[1] This is the sensitivity to the squared $\delta n^2_{k_\theta}$ fluctuations. Sensitivity to δn_{k_θ} is higher by a factor of $\sqrt{2}$.

7 Perpendicular velocity and magnetic field pitch angle measurements

Turbulent density fluctuations in tokamaks are expected to be nearly aligned in direction of the magnetic field lines and to propagate in the perpendicular direction. In this chapter, the PCR diagnostic has been applied for the reconstruction of the perpendicular velocity $v_\perp = v_{E\times B} + v_{ph}(k_\perp)$ and the magnetic field pitch angle α profiles. Section 7.1 is devoted to study $v_\perp$ profiles for different perpendicular wavenumbers of L-mode AUG plasma using PCR ($k_\perp$ = 0–3 cm^{-1}) and DR ($k_\perp$ = 6–16 cm^{-1}) diagnostics. The $v_\perp$ profiles are compared with neoclassical estimations of the $E \times B$ drift velocity $v_{E\times B}$ and with calculations of the turbulent phase velocity $v_{ph}(k_\perp)$ from nonlinear gyrofluid simulations using the GEMR code. The α profiles are investigated in section 7.2 in both AUG and TEXTOR tokamaks. The measured α profile in AUG is compared with values obtained by magnetic reconstruction using the equilibrium code CLISTE.

7.1 Perpendicular velocity measurements

7.1.1 Typical profile

By scanning the PCR probing frequency, a radial velocity profile is obtained. Here the Bayesian approach from section 6.2.4 has been applied to obtain $v_\perp$ and its error $\sigma_{v_\perp}$ from measured time delays. An example from L-mode discharge #32294 is shown in figure 7.1a (red line). All $v_\perp$ points have been corrected with the decorrelation correction factor $(1 - \tau_a^2/\tau_d^2)$ explained in section 6.1.3, which was about of 0.94, except in the shear region where it was 0.8. The measured $v_\perp$ changes sign from electron diamagnetic direction in the plasma edge ($\rho_{\rm pol} > 0.95$) to ion diamagnetic direction in the plasma core ($\rho_{\rm pol} < 0.95$) due to a contribution of a toroidal velocity in the $v_{E\times B}$ velocity. The edge region of the similar discharge #32316 is shown in more detail in figure 7.1b (red line). The PCR $v_\perp$ profile has a gap in the region $\rho_{\rm pol}$ =0.92–0.975, which is related to a loss of correlation at these radii (although the fluctuation signal

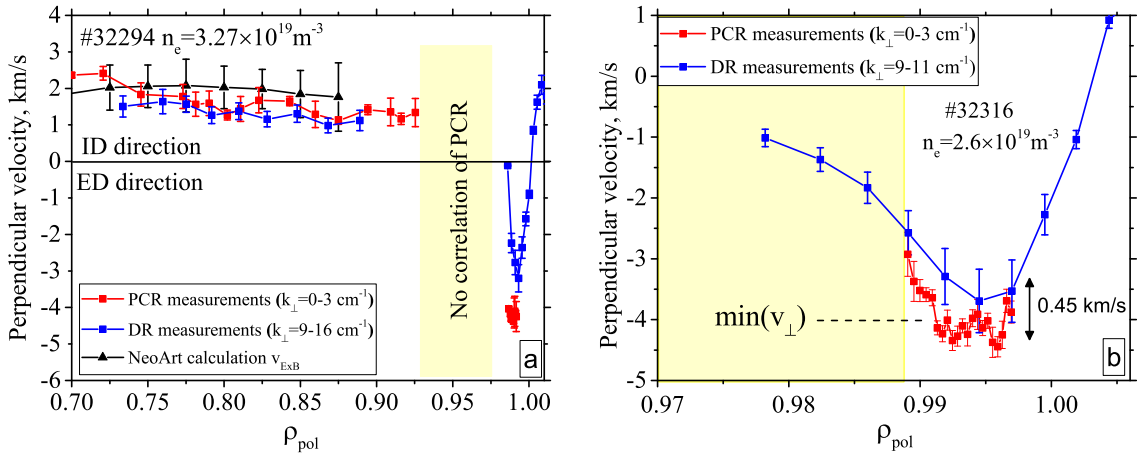

Figure 7.1: (a) Velocity profiles from discharge #32294. (b) Zoom in velocity profiles of edge region #32316.

remains strong). Such a behavior appears to be related to a decrease of the decorrelation time τ_d of the density fluctuations in this region simultaneously with a increase of the propagation time caused by decrease in $v_\perp$. For small values of τ_d, eddies on the magnetic surface decorrelate faster than the time needed to propagate between the measurement volumes and therefore $v_\perp$ cannot to be measured. More details on the measurement of τ_d are given in section 8.2.1.

The PCR $v_\perp$ measurement have been compared with Doppler reflectometry (DR) measurements, which give the local $v_\perp = v_{E\times B} + v_{ph}(k_\perp)$ of turbulent fluctuations at some specific wavelength $k_\perp$ [93, 94]. For comparison the DR measurements (blue curves in figure 7.1) have been projected from their measurement location to the position of the PCR (mid-plane) by correcting the radial electric field due to magnetic flux surface compression. It is important to emphasize that the DR measures at higher wavenumber $k_\perp = 9$–$16\,\mathrm{cm}^{-1}$ compared to the PCR with $k_\perp = 0$–$3\,\mathrm{cm}^{-1}$. A dependence of $v_\perp$ on the wavenumber $k_\perp$ could arises from a change in the turbulent phase velocity Δv_{ph}, but PCR and DR yield similar values and the same trend (figure 7.1a). The difference in the core region $\rho_{\mathrm{pol}} = 0.7$–$0.92$ is small (< 0.3 km/s) and inside the error bars of the measurements. However, the difference in the edge ($\rho_{\mathrm{pol}} = 0.98$–$1.00$) of the order 0.5 km/s (figure 7.1b) might be related to different phase velocities of the turbulence.

Since in the core ($\rho_{\mathrm{pol}} = 0.7$–$0.9$) both PCR and DR measure similar velocities independent of $k_\perp$ it might be possible to estimate v_{ph} from the difference with the neoclassic calculation of the $E \times B$ drift velocity $v_{E\times B}$ obtained by the code NEOART [60] which includes fluid toroidal rotation measurements from charge exchange recombination spectroscopy. The result shown in figure 7.1a (black triangles) suggests that the neoclassical $v_{E\times B}$ and $v_\perp$ by PCR are very close again. The phase velocity is smaller

than the error bars of the NEOART calculations ($\approx 0.5\,\mathrm{km/s}$). Such a small phase velocity is in agreement with gyrokinetic calculations [37, 52] for trapped electron mode and ion temperature gradient turbulence which are theoretically predicted to be unstable in the plasma core. The NEOART code has been compared previously with fluid velocity measurements from charge exchange recombination spectroscopy [57, 131] and has shown good agreement. The absolute value of the phase velocity v_{ph} and its dependence on the perpendicular wavenumber $k_\perp$ in the edge region are investigated in the next section.

7.1.2 Phase velocity in the edge region of AUG

A cross-phase spectrum $\Delta\phi(f)$ between different antennas of the PCR permits the estimation of the dispersion relation $k_\perp(f) = \Delta\phi(f)/\varepsilon_\perp$ of the propagating density fluctuations (see section 6.3). Such a dispersion relation is shown in figure 7.2a at $\rho_{\mathrm{pol}} = 0.985$ for discharge #32520. The combination BD used for this case has a perpendicular separation of $\varepsilon_\perp = 15\,\mathrm{mm}$. However, any other combination can be used, showing similar results. The slope of the dispersion relation (fitted red line) is almost linear. This suggests that turbulent modes with different $k_\perp$ rotate with the same velocity

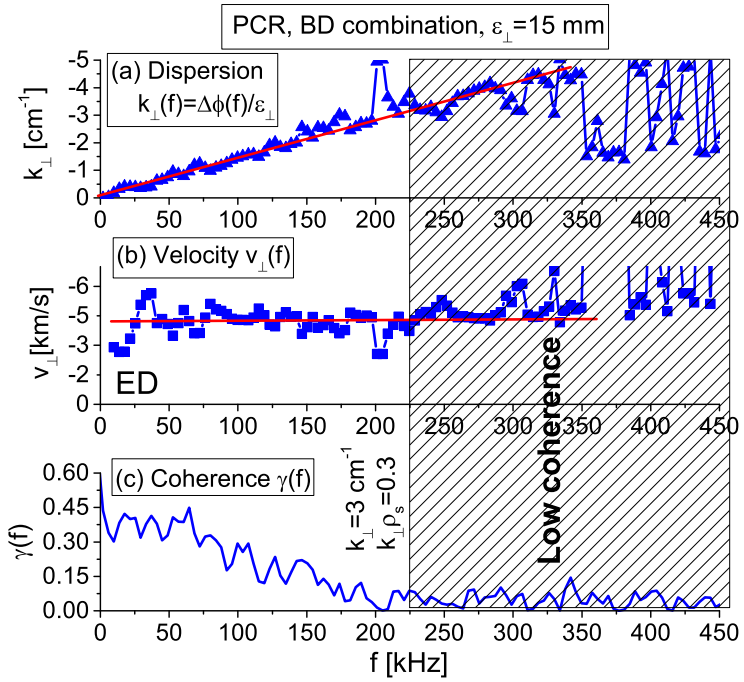

Figure 7.2: From top to bottom, the following quantities are shown: (a) dispersion relation, (b) perpendicular velocity and (c) amplitude of spectral coherence as function of frequency.

$v_\perp$. Figure 7.2b shows the velocity as a function of frequency $v_\perp(f) = 2\pi f / k_\perp(f)$. It can be concluded that $v_\perp = v_{E\times B} + v_{ph}(k_\perp)$ and hence $v_{ph}(k_\perp)$ do not depend on the perpendicular wavenumber within the range of $k_\perp$ = 0–3 cm^{-1}. The maximum $k_\perp$ the PCR system is limited by the sensitivity $S(k_\perp)$, which results in $k_\perp \approx 3$ cm^{-1} (see section 6.4.2). At this value the amplitude of the spectral coherence is small (see figure 7.2c). Note, however, that even this small level of spectral coherence gives a reasonable estimate of the cross-phase and the dispersion relation up to $k_\perp = 4.5$ cm^{-1}.

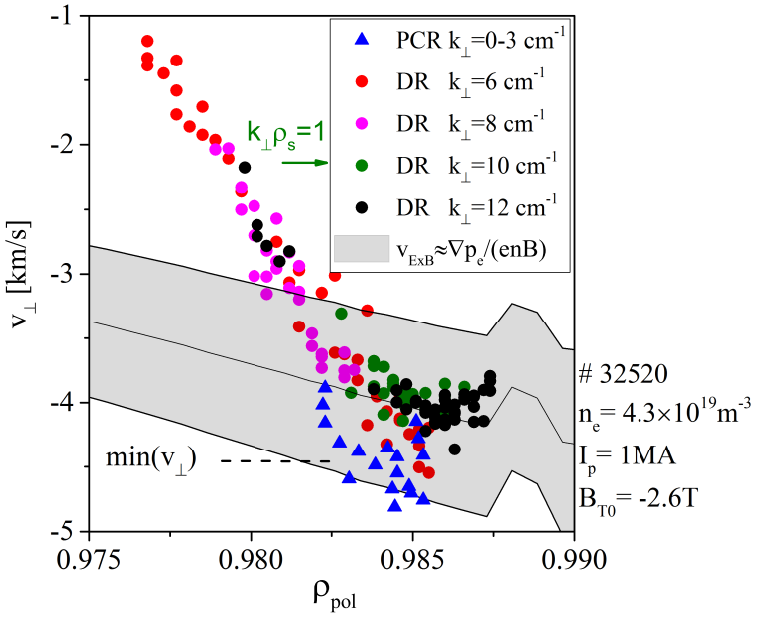

Figure 7.3: Comparison of measured velocities at different $k_\perp$ in the edge region using poloidal correlation reflectometry ($k_\perp$=0–3 cm^{-1}) and Doppler reflectometry ($k_\perp$=6, 8, 10, 12 cm^{-1}).

To increase the measured region further, a dependence of $v_\perp(k_\perp)$ has been obtained using a DR diagnostic with a movable mirror [93]. The measured radial profiles of $v_\perp(k_\perp)$ at $k_\perp$ = 6, 8, 10 and 12 cm^{-1} with DR are shown in figure 7.3. The measurement obtained by the PCR for $k_\perp$ = 0–3 cm^{-1} is also plotted in the same figure. The data cover the region $k_\perp \rho_s$ = 0–1.2. The result suggest that the dependence of $v_{ph}(k_\perp)$ is weak ($\Delta v_{ph} \lesssim 0.5$ km/s in ED direction between $k_\perp$ = 0–3 and 10–12 cm^{-1}).

The magnitude of the turbulent phase velocity v_{ph} in the edge is estimated from the difference of the measured $v_\perp$ and the neoclassical estimate of the $E \times B$ velocity $v_{E\times B}$. Here, the simple approximation $v_{E\times B} \approx \nabla p_i / enB \approx \nabla p_e / enB$ in the plasma edge has been used (see section 2.6). It is assumed that $T_e \approx T_i$, which is in agreement for

line average density around 4.3×10^{19} m^{-3} due to high electron-ion collisional energy exchange $p_{ei} \propto n^2(T_e - T_i)/T_e^{3/2}$, as shown in [132] and discussed in [21]. The dilution of the ions by impurities does not play a significant role because $\nabla n_i/n_i \approx \nabla n_e/n_e$ giving that concentration of the impurity weakly depends on radius within $0.97 < \rho_{pol} < 0.99$ as shown in [57]. The neoclassical $E \times B$ velocity in the edge (gray shadow in figure 7.3) is close to the DR values at high $k_\perp = 12$ cm^{-1}, however, slightly smaller (≈ 0.5 km/s) compared to the lower PCR values of $k_\perp = 0$–3 cm^{-1}. This suggests that v_{ph} at the position of $\min(v_\perp)$ is small ($\lesssim 0.5$ km/s in ED direction). It should be noted, that the shape of the $\nabla p_e/enB$ and the measured $v_\perp$ profiles are different. A similar observation was obtained in [133] in an L-mode plasma with electron cyclotron resonance heating. The difference at $\rho_{\mathrm{pol}} = 0.975$ probably a result of the toroidal rotation contribution to $v_{E\times B}$ which increases towards the plasma core (see section 2.6).

The dependence of the measured $\min(v_\perp)$ for different line averaged densities $\bar{n}_e$ and plasma currents I_p is shown in figure 7.4. It is found that $\min(v_\perp)$ increases with $\bar{n}_e$, which can be explained by an increase in ion pressure gradient. On the other hand $\min(v_\perp)$ decreases with I_p which contradicts to the intuitive expectation that T_e increases with I_p. As discussed in [21] and [133] at low density ($n < 3.0 \times 10^{19}$ m^{-3}) the collisional energy exchange for small I_p is higher because T_e is lower. This may lead to an increase in T_i and hence of $v_{E\times B} \approx \nabla p_i/enB$. However, T_i in the edge has not been measured for the present discharges. Note that the power threshold for the L-H transition at low density is also lower for small values of I_p [21]. Observations in this section demonstrate that $v_\perp$ is dominated by $v_{E\times B}$, i.e. the turbulent phase velocity in the edge region is small.

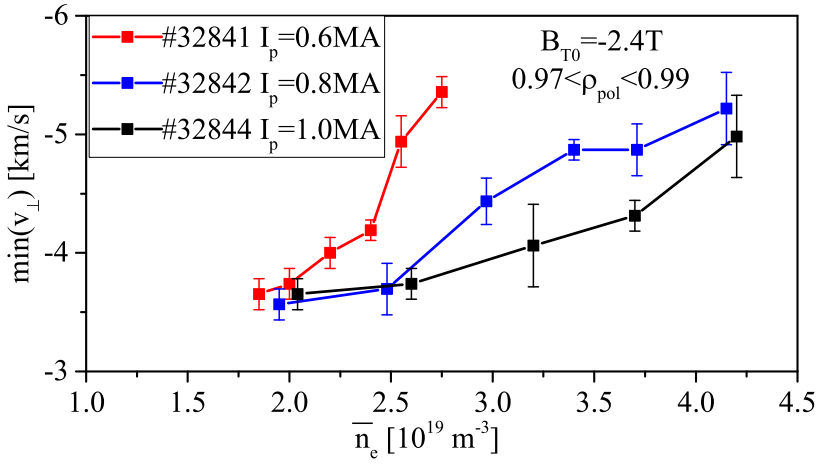

Figure 7.4: Dependence of $\min(v_\perp)$ at the edge on line averaged density $\bar{n}_e$ and plasma current I_p.

7.1.3 Comparison of v_{ph} with linear predictions and with GEMR code

The measured turbulent phase velocity of $v_{ph} \lesssim 0.5$ km/s in the edge region has been compared with theoretical expectations. According to equation 2.10 linear electron drift wave theory yields a value of 4 km/s at $k_\perp = 1$ cm^{-1} in the ED direction, which is clearly too large. Moreover, a strong $k_\perp$ dependence is expected, which is not observed experimentally. One approach to investigate the difference is to cross-check with nonlinear turbulence simulations.

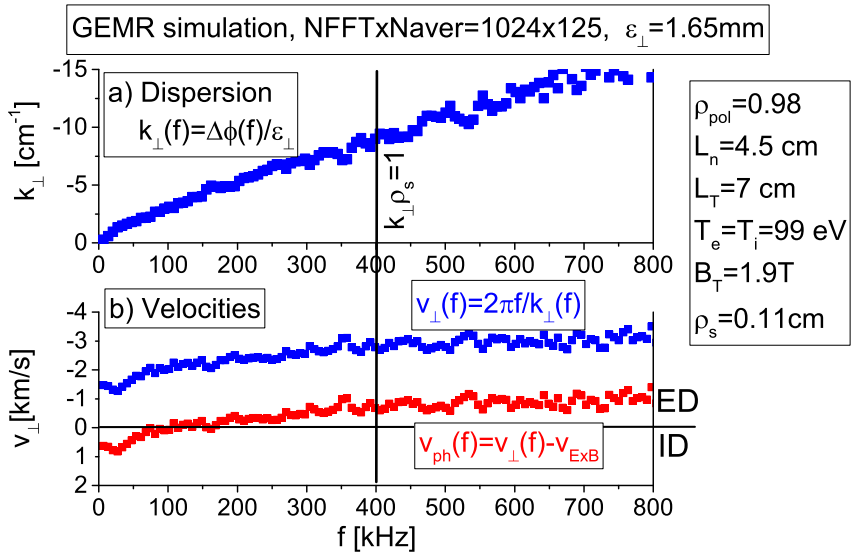

Figure 7.5: Results from the turbulence code GEMR. (a) The dispersion relation, (b) the perpendicular velocity (blue) and the phase velocity (red).

Turbulent fluctuations in the tokamak edge can be simulated with the code GEMR [17, 18]. GEM is a gyrofluid electromagnetic model for electrons and ions; the 'R' refers to global (radially dependent) geometry. Further information on the GEM model can be found in [134]. Only a brief description of the GEMR code is given in this section. GEMR solves the gyrofluid equations in three dimensional space (r, $\perp$, $\|$) simultaneously for electrons and ions. The equations for electrostatic potential and parallel magnetic potential are also included in a self-consisted manner. The code can simulate the electron drift wave and ion temperature gradient turbulence. The code does not include a model for trapped particles and therefore trapped electron mode turbulence cannot be simulated, however, trapped electron modes are expected to be damped due to high collisionality in the edge region (see figure 3.6). The field-aligned approach of GEMR does not allow simulations in X-point geometry, thus all simulations

are performed with a circular plasma cross-section.

Minor radius, major radius and magnetic field are taken from a typical L-mode AUG discharge ($R = 1.65$ m, $a = 0.5$ m, $B_{T0} = 2.4$ T). The gradients of temperature and density were set close to experimentally measured values, however, the self-consistent solutions of GEMR have reduced gradients. The plasma parameters of the simulation are given in the right frame of figure 7.5. The simulation grid was 128×512×16 points with a point separation of $\Delta_r = 0.39$ mm, $\Delta_\perp = 0.33$ mm and $\Delta_\parallel = 2.98$ m. The simulated data is written out with a time step of $\Delta t = 0.144$ μs for subsequent analysis. It should be noted that due to the different plasma cross-section (circular instead of D shaped) the results cannot be used for a detailed quantitative comparison. Furthermore the gradients in simulations were smaller than in experiment ($L_n = 4.5$ instead of 2.5 cm and $L_T = 7$ instead of 5 cm).

Figure 7.5a shows the dispersion relation obtained from the simulated density fluctuations at $\rho_{\mathrm{pol}} = 0.98$. Similar to the procedure used for the experimental data the dispersion relation $k_\perp(f) = \Delta\phi(f)/\varepsilon_\perp$ has been obtained from the cross-phase $\Delta\phi(f)$ of density fluctuations between two separated volumes. The perpendicular separation $\varepsilon_\perp = 1.65$ mm has been selected to be shorter than in the experiment. This was required in order to reconstruct the dispersion relation up to $k_\perp = 15$ cm^{-1}. However, an estimation of the dispersion relation from longer separations yields similar results. Figure 7.5b (blue line) shows the perpendicular velocity $v_\perp(f) = 2\pi f/k_\perp(f)$, which varies between -1.5 km/s (ED direction) at $k_\perp \approx 0$ cm^{-1} to -2.6 km/s at $k_\perp = 15$ cm^{-1}.

The turbulent phase velocity (red line) was obtained by subtracting the $E \times B$ drift velocity from the total perpendicular velocity. Here, $v_{E\times B}$ has been calculated from the

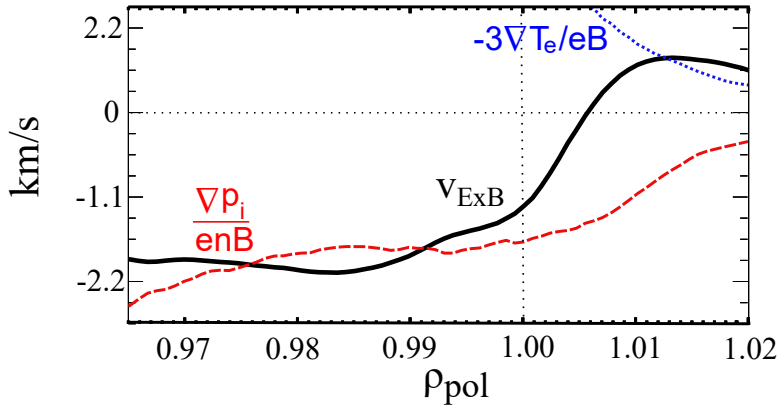

Figure 7.6: Comparison of GEMR $E \times B$ drift velocity $v_{E\times B}$ with simple neoclassical estimate $\nabla p_i/enB$.

derivative of the background electrostatic potential at the same radial position. At this particular position it is $v_{E\times B} \approx 2$ km/s in the ED direction. Note that $v_{E\times B}$ is smaller compared to the experimental result due to lower gradients in the temperature and density profiles, however, as in experiment $v_{E\times B}$ agrees with the simple neoclassical estimate $\nabla p_i/enB$ (figure 7.6). The GEMR phase velocity is small, $v_{ph} < 0.7$ km/s but it changes sign from the ED direction at $k_\perp > 3$ cm^{-1} to the ID direction at $k_\perp < 3$ cm^{-1}. Therefore, a small phase velocity v_{ph} can be reproduced in nonlinear simulations in principle. More detailed studies are needed to understand the reason for these small phase velocities v_{ph}.

7.1.4 GAM velocity oscillation

The Geodesic Acoustic Mode (GAM) is a radially localized ($k_r \neq 0$) oscillating $v_{E\times B}$ shear flow with an $m = n = 0$ perturbation in the potential (m, n the poloidal and toroidal numbers). The GAM has the potential to suppress turbulence via flow shearing mechanism or acting as a turbulence energy sink (see section 2.5). Therefore, it is of interest to test the feasibility of detecting GAM oscillations with the PCR diagnostic. At ASDEX Upgrade GAMs exhibit frequencies in the range of 5–20 kHz [135, 136, 137]. To detect such high frequencies only a short time window for the calculation of the peak correlation time delay τ_m can be used. We tested several discharges at $\rho_{\text{pol}} = 0.95$–0.99, where τ_m was calculated from a 20 μs (40 points) correlation windows. In order to achieve low statistical noise the antenna combinations with the shortest perpendicular separation (EC and BD) have been used. The spectrum has been calculated with 512 points of τ_m and averaged over 30 sub-windows without overlap. The GAM spectral

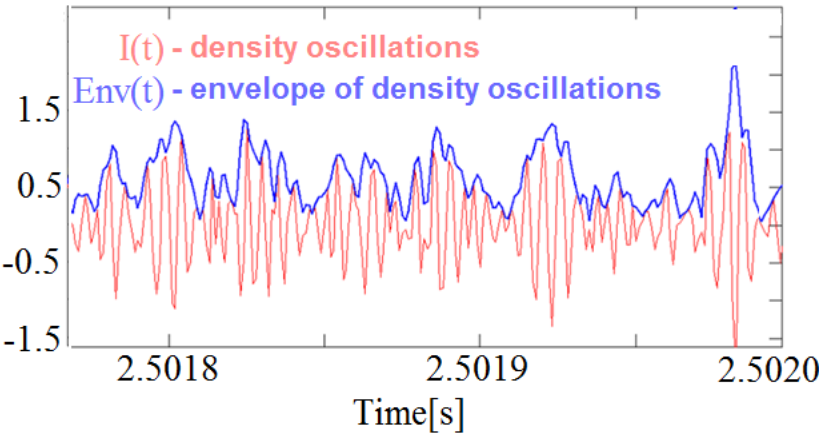

Figure 7.7: The filtered density fluctuations from 250 to 450 kHz (blue) and their envelope (red) for antenna B.

peak has not been found in τ_m spectra, although the GAM has been observed by the DR diagnostic which measure $v_\perp$ oscillation. The probable reason could be connected with a high statistical noise caused by the small size of the correlation window used for the τ_m estimation. Advanced algorithms for time delay analyses, such as a generalized cross-correlation phase transform [138] can be attempted in the future to decrease the statistical noise and improve the time resolution of the time delay measurements.

Nevertheless the GAM oscillation is found in the modulation of the high frequency density fluctuations. Here, one can use the observation that high frequency density turbulence is expected to be modulated by the GAM, as proposed by Nagashima who used the envelope of high frequency density oscillations from electrostatic Langmuir probes [139]. The envelope is given by $\mathrm{Env}(t) = \sqrt{I(t)^2 + H(I(t))^2}$. Here $I(t)$ is the high frequency component (250–450 kHz) of the in-phase signal and its Hilbert transform is $H(I(t))$. Figure 7.7 shows an example of $I(t)$ and $\mathrm{Env}(t)$ for antenna B. The GAM frequency can be seen in the spectrum of the envelope (figure 7.8a). Note, that the envelope shows only a small peak around 13 kHz. However, the coherence between envelopes from two different antennas (B and D) shows clearly the GAM frequency (figure 7.8b). The method has been compared with DR flow measurements

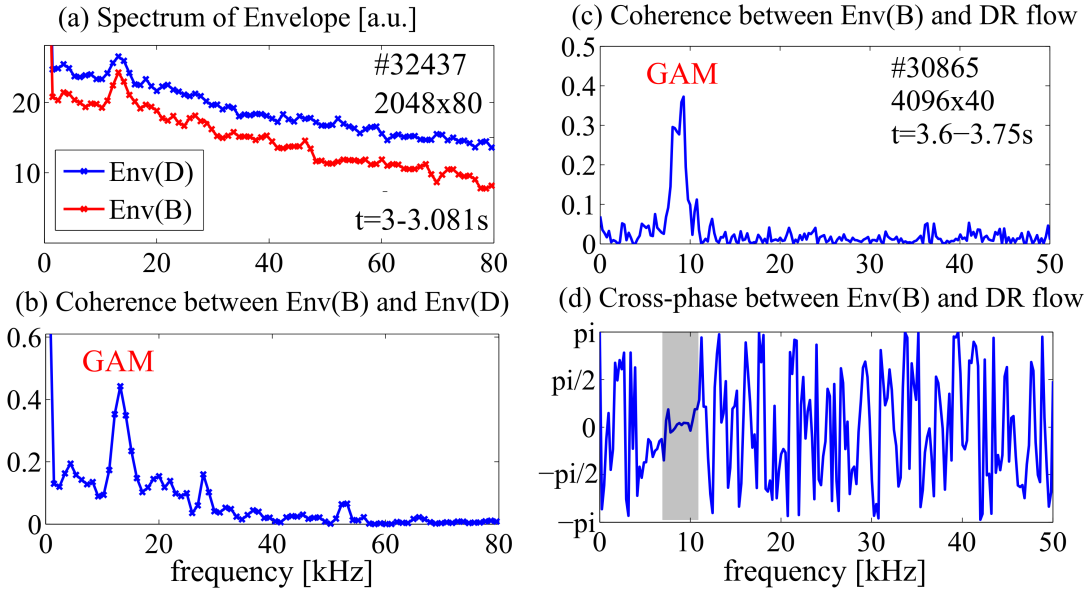

Figure 7.8: (a) The spectrum of the envelope for antennas B and D. (b) Coherence between the envelops from antennas B and D. (c) Coherence between envelope of antenna B and flow measurement by DR. (d) Cross-phase between envelope of antenna B and flow measurement by DR.

traditionally used for investigations of GAMs at AUG [135]. The flow (DR) and the envelope modulation (PCR) are perfectly in phase (see figure 7.8d). This fact is in contradiction to the study by Nagashima et al. [139], who found a cross-phase of $\pi/2$ between flow and envelope. This observation suggests that in the case of AUG a modulation of the high frequency turbulence is observed due to a width modulation of the frequency spectrum caused by convection (assuming $\omega = k_\perp v_\perp$), and not due to a real modulation of the turbulence energy.

7.2 The magnetic field pitch angle measurements

7.2.1 Dependence of measured α on plasma current and magnetic field

The dependence of the inclination of the turbulent eddies in poloidal-toroidal plane, being a measure of the field line pitch angle α, has been investigated on AUG with the PCR. Here the Bayesian approach, explained in detail in section 6.2.4, has been applied to obtain α and its error σ_α. The sign of α coincides with the expected direction of the magnetic field line. In figure 7.9a an inversion of α with the reversal of B_{T0} is observed. For this case two discharges (#33578 and #33579) are analyzed. Both discharges have the same plasma parameters (upper single null, $I_p = 0.6$ MA, measurement position $\rho_{\text{pol}} = 0.98$) and differ only in the direction of B_{T0} as shown by the blue arrows. Note that the value of $|\alpha|$ for negative B_{T0} is slightly higher compared to that for positive B_{T0} ($\Delta\,|\alpha| \approx 1°$). The expected increase of α with I_p is observed as well. This is shown

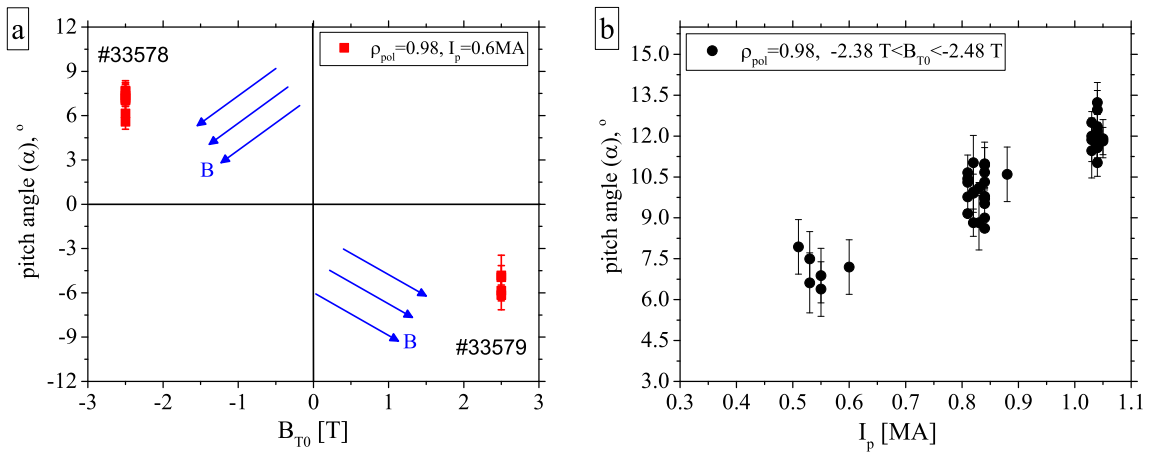

Figure 7.9: (a) Inversion of the measured pitch angle with a change of magnetic field. (b) Variation of the measured pitch angle for different plasma currents at AUG.

in figure 7.9b, where a series of discharges with different I_p are analysed. The magnetic field strength varied only slightly (2.38 T< $|B_{T0}|$ < 2.48 T). The analysis is performed in the edge region at $\rho_{\mathrm{pol}} = 0.98$. A linear dependence is found. The dependence of α on the magnetic field strength has also been studied. Here, a decrease of α with increasing B_{T0} is observed (not shown here).

7.2.2 Pitch angle profiles at TEXTOR

In this section results from the TEXTOR tokamak are presented. Figure 7.10a shows an example of α profiles obtained from the top (circles) and LFS (squares) antenna arrays of the TEXTOR tokamak. Plasmas with $B_{T0} = 1.9$ T and different densities $\bar{n} = [1,\ 1.5,\ 2.0]\times 10^{19}$ m^{-3} have been investigated. During the discharges a current ramp from 400 down to 250 kA was performed. The LFS and top measurements at $r/a = 0.8$ yield similar pitch angle values (i.e. the helicity is constant), although, the values measured with the LFS at $r/a = 0.7$ are slightly higher compared to those from the top antennas. This may be linked to the magnetic flux surface compression on the LFS due to the Shafranov shift.

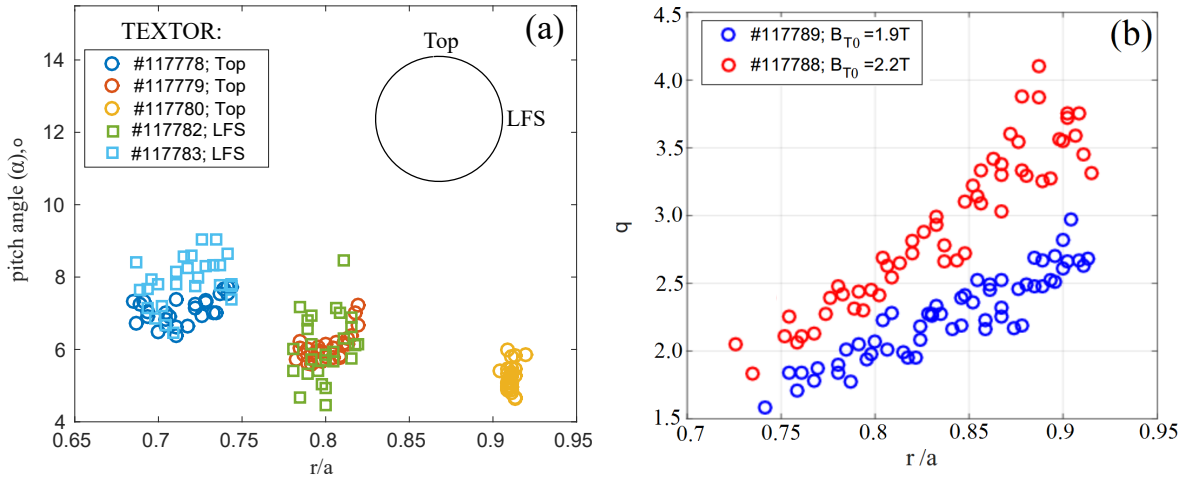

Figure 7.10: (a) Scaling of α with r/a from top (circles) and LFS (squares) antenna array positions at TEXTOR. (b) Estimation of $q(r)$ from top antenna array at TEXTOR for two values of the toroidal magnetic field.

For TEXTOR, with its circular plasma shape, the local q profile has been estimated from α using the following equation for the top antenna array

$$q(r) = \frac{r}{R_0 \tan(\alpha)}, \tag{7.1}$$

where the minor radius of the plasma is denoted by r, and the major radius is $R_0 = 1.75$ m. Note that this equation is not applicable for the AUG tokamak due to the non-circular plasma cross-section. In figure 7.10b the evolution of the q profile with respect to the reflection layer and for 2 different magnetic field strengths is shown (top antenna array, #117788-89). This has been achieved by applying a density ramp from $\bar{n} = 1.5$ to 3.0×10^{19} m^{-3} at fixed probing frequency. As expected the q values for $B_{T0} = 1.9$ T are lower than those for $B_{T0} = 2.2$ T. This becomes especially clear in the plasma edge where q is higher. All observations confirm that the measured angle is closely linked to the magnetic field line pitch angle. It is interesting to note that around rational surfaces ($q = 2/1, 5/2, 3/1$) the q profile shows dips, which may be related to magnetic island formation. However, further studies are needed and are outside of the scope of this thesis.

7.2.3 Comparison with CLISTE code at AUG

For AUG, measurements of α by the PCR have been compared to α estimated by magnetic equilibrium reconstruction from the CLISTE code [76]. Here, the α profile from CLISTE is computed directly from the magnetic field components (B_R, B_Z, B_T) from the equilibrium reconstruction at the corresponding PCR measurement location

$$\alpha = \arctan\left(\frac{B_\theta}{B_T}\right) = \arctan\left(\frac{\sqrt{B_R^2 + B_Z^2}}{B_T}\right). \tag{7.2}$$

For typical L-mode plasmas the α profile from the CLISTE reconstruction over the range ρ_{pol} =0.7–1.0 is almost flat. Both the α profile and the parametric dependence of α at fixed radius have been compared for different discharges.

Figure 7.11a shows a comparison of α measured by the PCR with the one obtained by equilibrium reconstruction in the plasma edge at ρ_{pol} =0.97–0.99 for 20 discharges. In general both values and the trend are reproduced approximately. For each discharge a plasma time interval ($\simeq$ 20 ms long) has been selected with stable plasma parameters in terms of plasma current, magnetic field and density. Across the database B_{T0} varied between 1.55 and 2.9 T and I_p between 0.5 and 1.05 MA. To minimize the effect of the density profile, only discharges with averaged line density in the range $\bar{n} = 2.5$–3.2×10^{19} m^{-3} have been included. This constraint ensures (i) the same radial resolution for the measurement and (ii) the same poloidal and toroidal separation between the measurement positions of the antennas. The discharges with significant deviations between measured and equilibrium α cannot be explained by the measurement error bars. Indeed, during individual discharges with the constant measurement position of the PCR the difference between PCR and CLISTE remains constant. The pitch

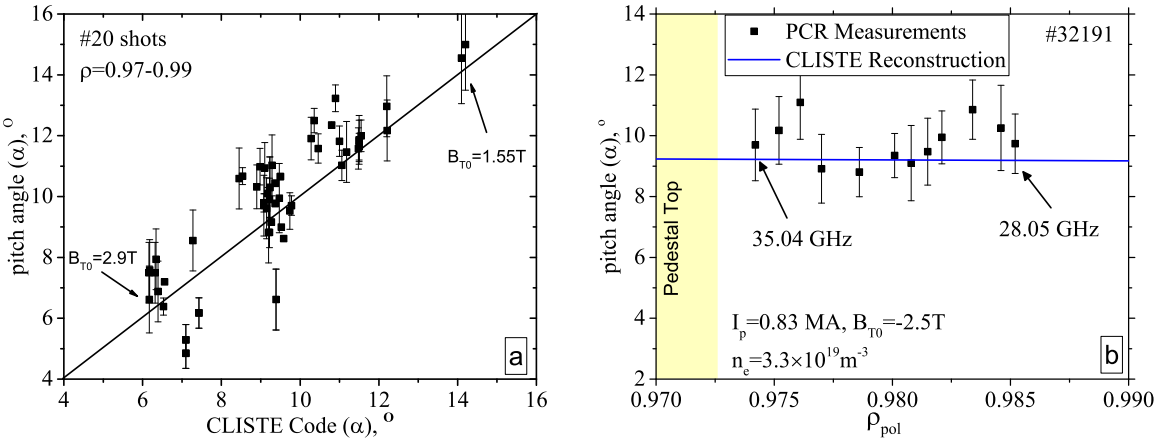

Figure 7.11: (a) Comparison of α measured by the PCR with reconstructed values from the CLISTE equilibrium code. 20 different discharges have been compared in the edge region. (b) Profile of α in the edge region of the plasma.

angle profile at the edge in figure 7.11b shows similar values for all probing frequencies across the plasma edge region, which are in good agreement with the CLISTE results. This demonstrates that the method gives the same results independent of the probing frequency used.

Figure 7.12a shows a comparison of PCR and CLISTE radial pitch angle profiles for the core plasma region ρ_{pol} =0.7–0.94 of discharge #32212. Two frequency sweeps were made during a stable flat density phase and both profiles show a similar shape. Deviations from the constant CLISTE value are found at $\rho_{\mathrm{pol}} = 0.85$–$0.95$ (inside of the density pedestal position) reaching values of about 2–3°. However, these deviations decreases towards the core. Similar observations are obtained when using a density scan with a fixed probing frequency instead of a frequency scan with fixed density, as shown for discharge #31427 in figure 7.12b.

In the following, different effects are discussed which could be the cause for the discrepancy.

1. In order to increase the calculated pitch angle by CLISTE, the current density around the pedestal position would need to be increased. To get agreement between PCR and CLISTE the integrated plasma current $\int j(r)\mathrm{d}r$ would have to be increased by 150–200 kA. This change is unrealistically large in L-mode plasmas compared to the total plasma current of 800 kA. The effect of the edge bootstrap current was evaluated to be $< 0.25°$ using the method from [140].

2. The difference between PCR and CLISTE could appear because CLISTE produces an axisymmetric reconstruction, while the PCR angle measurements

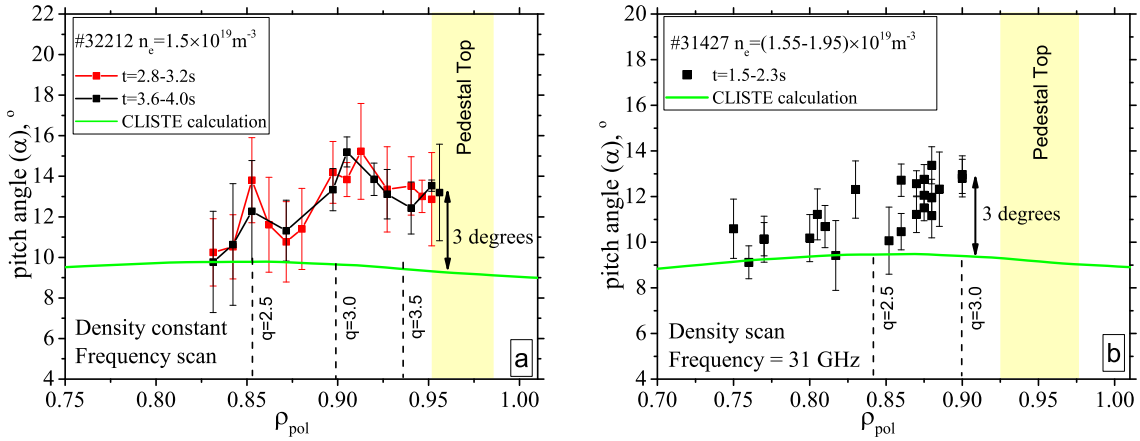

Figure 7.12: Comparison of α profiles for the core region of the plasma: (a) from 2 Ka-band frequency sweeps with constant density and (b) during a density ramp with fixed probing frequency.

are (toroidally) local. The toroidal magnetic field ripple effect could create a difference. If this was the reason, local PCR angles might be used as an additional parameter for a better 3D equilibrium reconstruction. However, calculations by Strumberger [141] suggest that the magnetic field ripple effect is small ($< 1\,\%$) and thus cannot explain the difference.

3. The measured angle is a superposition of the magnetic field pitch angle and an additional turbulence inclination angle (section 2.3.1). To obtain a 2–3° declination for turbulent structures with $k_\theta \approx 0.5$–1 cm^{-1} a short parallel correlation length of 2–4 m is necessary. The decrease of the difference in α towards the core could be due to an increase in parallel correlation length according to equation 2.9. A parallel correlation length of 2–4 m would be rather short compared to result from previous studies [39, 40, 41, 42], but not impossible.

It is interesting to note that the profile shows a weak wavelike radial structure. This structure could be a signature of small islands around rational surfaces. In the radial region shown in figure 7.12a the rational surfaces $q = 2/1,\ 5/2,\ 3/1$ are located according to the CLISTE code. A small oscillation in the pitch angle is also observed in the result from TEXTOR (figure 7.10b).

7.2.4 Pitch angle in H-mode

The measurement of α during the high confinement mode (H-mode) is usually difficult due to (i) the low level of correlation (the edge turbulence level in H-mode is reduced)

and (ii) Edge Localized Mode (ELM) activity, when the position of measurement is constantly changing since the density profile varies during the ELM cycle. However such measurements were possible for discharge #32094 during an ELM period in H-mode. The α in figure 7.13a is not constant (as is usually observed in L-mode), but oscillates with a high amplitude of several degrees. The amplitude of the velocity modulation (figure 7.13b) is significantly smaller. Note that the comparison with equilibrium CLISTE values give smaller values by factor of two. Such a behavior is unusual and requires more experimental studies. Different radial positions and plasma parameters could be measured in future to investigate the reason for the oscillation. Conditional averaging or sample techniques between several ELM cycles could be applied to obtain ELM averaged results.

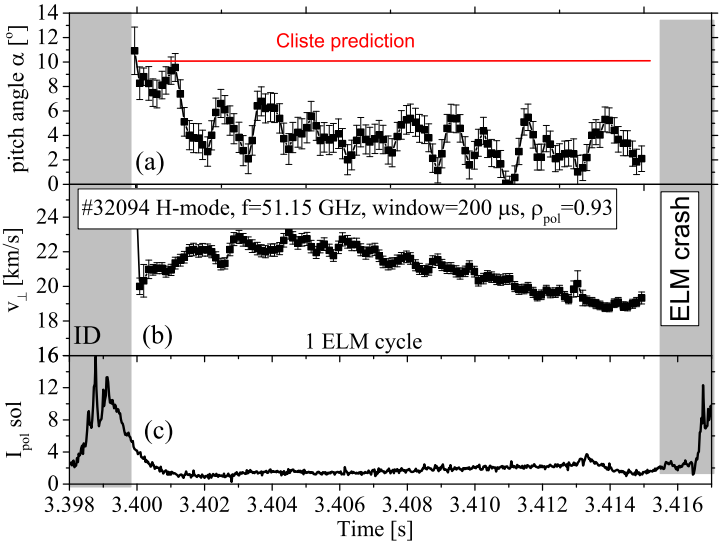

Figure 7.13: The dynamic of pitch angle α and perpendicular velocity $v_\perp$ during a edge localized mode cycle in H-mode of discharge #32094.

7.3 Discussion

This chapter presented measurements of the perpendicular velocity $v_\perp = v_{E\times B} + v_{ph}(k_\perp)$ and the magnetic field pitch angle α from L-mode plasmas in the TEXTOR and ASDEX Upgrade tokamaks.

The perpendicular velocity profile obtained with PCR and DR at AUG shows reasonable agreement with neoclassical $v_{E\times B}$ velocities from the NEOART code in the core. However, small difference of the order of 0.5 km/s (in the electron diamagnetic direction) between $v_\perp$ and the neoclassical estimate of $v_{E\times B}$ is observed in the plasma

edge, which may be connected to a turbulent phase velocity v_{ph}. The obtained turbulent phase velocity in the edge, however, is significantly lower than that predicted for linear electron drift waves from equation 2.10 ($v_{ph} \approx 4$ km/s) for the presented discharge. Nonlinear simulations of edge turbulence by the GEMR code yield small phase velocities ($v_{ph} < 0.7$ km/s) as well, which can explain the observations taking into account the error bars of the measurements. An explanation of the observed small phase velocity will be an important task for theory and future experiments.

The magnetic field pitch angle α has been measured as a function of B_{T0} and I_p and the expected dependencies have been observed. Similar profiles from the top and LFS launch antenna in TEXTOR have been obtained. The calculation of local q profiles at TEXTOR from the pitch angle profiles yields reasonable results. A comparison of α measurements by PCR with values from the equilibrium reconstruction code CLISTE at AUG shows similar values in the plasma core and edge. However, a difference in the order of 2–3 ° remains around the density pedestal position. A possible explanation for the deviation is a reduced value in the parallel correlation length. For the considered plasma condition at the pedestal position and $k_\theta \approx 0.5$–1 cm^{-1} a parallel correlation length of $\approx$ 2–4 m is needed to reconcile the experimental with equilibrium calculations. The decrease of the α difference towards the core and edge could be due to an increase in the parallel correlation length according to equation 2.9.

It is important to note that the pitch angle measurement at the edge ($\rho_{\mathrm{pol}} = 0.98$) has been additionally validated by performing long range correlation measurements between two independent reflectometer systems at AUG: the O-mode PCR located in toroidal sector 2, and an O-mode, dual-channel (Q & V-band) frequency-hopping reflectometer system in toroidal sector 5 [142, 143, 144]. The separation between the two systems amounts to 1.5 and 0.12 m in toroidal and poloidal directions, respectively. A non-zero correlation ($\approx$ 20–40 %) is measured if the two systems are measuring on the same flux surface (there is a frequency overlap between the Ka and Q-bands) and close to a connection by a magnetic field line, which can be varied by the edge q profile. The pitch angle from these measurements is in an agreement with the pitch angle obtained from the PCR system alone.

The PCR method is limited to studying fast phenomena because τ_m can be determined only for a certain correlation window size. Even the measurement of GAMs by PCR is difficult at AUG. One possibility to decrease the correlation window size is to use advanced algorithms for time delay calculations such as the generalized cross-correlation phase transform [138] (PHAT method). GAMs can be also detected and studied using the envelope of high frequency fluctuations. It was shown, that the GAM flow and the envelope are modulate in phase, which opposite to $\pi/2$ shift observed in [139]. Hence an energetic coupling between small scale turbulence and the GAM cannot to be confirmed at ASDEX Upgrade for the case of analyzed discharge.

8 Turbulence correlation properties in AUG L-mode plasma

The perpendicular correlation length $l_\perp$ and decorrelation time τ_d of turbulent eddies determine the radial transport of particles and energy. Therefore understanding of their values and dependencies is important. The PCR diagnostic can measure these quantities using methods presented in sections 6.2.5 and 6.2.6. In section 8.1 the measurements of the effective correlation length (consisting of turbulent perpendicular correlation length and detection volume size $l_{\text{eff}} = \sqrt{l_\perp^2 + l_s^2}$) for different plasma parameters in L-mode plasmas at AUG are presented, while the τ_d measurements are studied in section 8.2.

8.1 Measurement of effective correlation length

Figure 8.1 shows typical fluctuation spectra of complex signal from the core (red) and edge (green) regions analysed in this chapter. The different widths in the core and edge are mainly due to different rotation velocities. The core rotation in L-mode Ohmic plasmas is smaller than the edge one, leading to a narrow frequency spectrum. For the calculation of l_{eff} and τ_d the frequency range from 2 to 750 kHz was used.

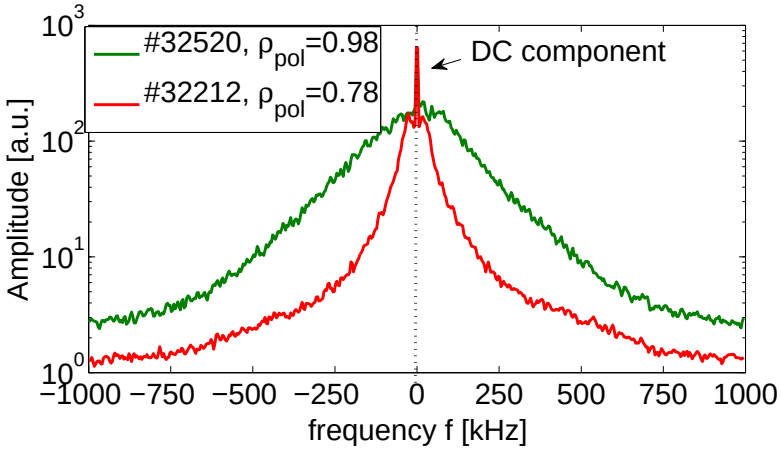

Figure 8.1: A typical fluctuation spectrum as analyzed in this chapter.

8.1.1 Radial l_{eff} profiles

Profiles of the effective correlation length $l_{\text{eff}} = \sqrt{l_\perp^2 + l_s^2}$ with the turbulence correlation length $l_\perp$ and detection volume size l_s measured with the PCR for two different densities $\bar{n} = 1.35 \times 10^{19}$ and 2.5×10^{19} m^{-3} from discharge #32841 are shown in figure 8.2 (black points). Here a frequency scan has been performed to obtain l_{eff} profiles. At

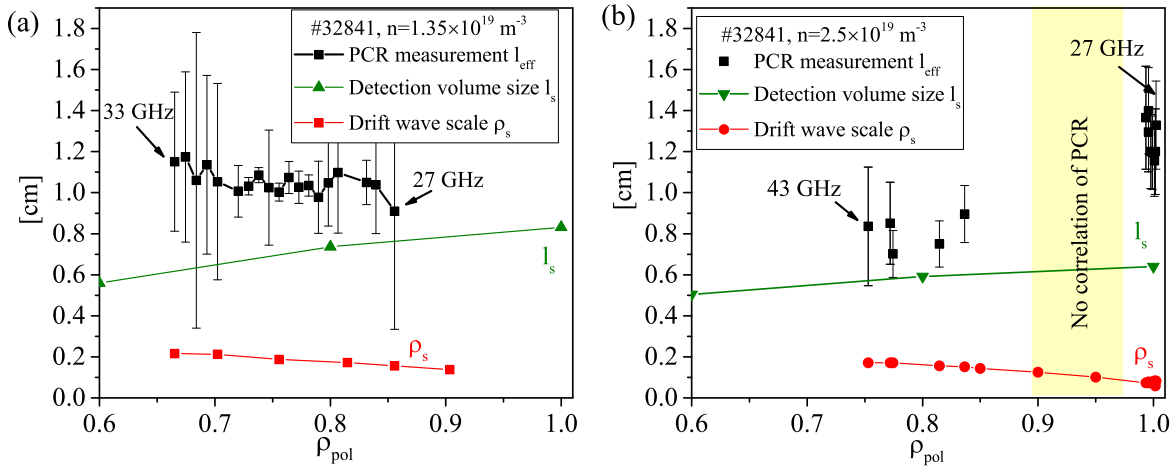

Figure 8.2: The profiles of the effective correlation length for two densities (a) $\bar{n} = 1.35 \times 10^{19}$ and (b) 2.5×10^{19} m^{-3}.

low density (figure 8.2a) l_{eff} is of order of 1 cm and increases towards the core over the region $\rho_{\text{pol}} = 0.6$–0.85. The edge region ($\rho_{\text{pol}} > 0.9$) is not covered in this example because the cut-off density is too small for the probing frequencies. The measurements at higher density (figure 8.2b) show similar values in the core ($\rho_{\text{pol}} < 0.9$), however it is interesting that l_{eff} increases at the edge ($\rho_{\text{pol}} = 0.97$–0.99). This is a typical observation seen in several discharges. One possible interpretation for the high values of l_{eff} in the edge could be the stretching of turbulent eddies along the direction of the sheared $E \times B$ flow (an example of sheared flows is shown in figure 7.1b). Note that the contribution of l_s also increases in the edge (see section 6.4.2), but less than the measured increase. The values of l_{eff} are compared with the drift wave scale ρ_s (red line). The effective correlation length in the core is $l_{\text{eff}} \approx 5\rho_s$ while in the edge it is higher, $\approx 13\rho_s$.

It is important to note that the measured value of l_{eff} is not significantly higher than the contribution of the detection volume size l_s (green line). Here l_s has been calculated using Born approximation as described in section 6.4.2. This means that the real turbulent correlation length $l_\perp$ is smaller than l_{eff}. The extraction of $l_\perp$ from l_{eff} is difficult because the value of l_s can be estimated only approximately. Rough

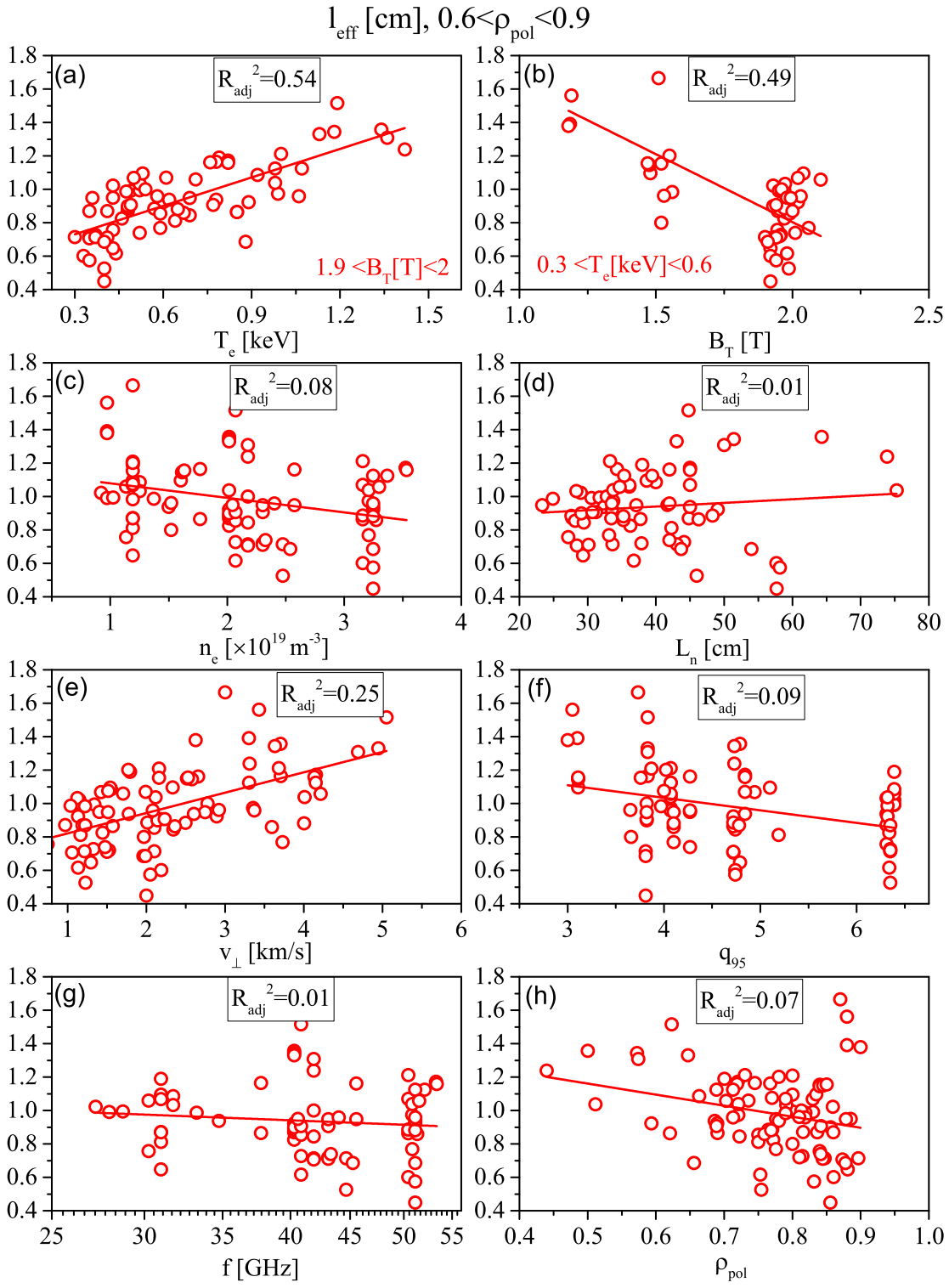

Figure 8.3: The dependence of effective correlation length in the core region $0.6 < \rho_{\mathrm{pol}} < 0.9$ on (a) electron temperature, (b) magnetic field, (c) density, (d) density scale length, (e) perpendicular velocity, (f) safety factor, (g) probing frequency and (h) radial position.

estimates gives $l_\perp \approx 3$–$4\rho_s$ in the core and $l_\perp \approx 9$–$11\rho_s$ in the edge. However, even a small contribution of $l_\perp$ to l_{eff} can be studied using regression analysis between l_{eff} and mean plasma parameters as presented in the next section.

8.1.2 The dependence of l_{eff} on mean plasma parameters

The dependence of l_{eff} on the mean plasma parameters has been investigated. A database of 12 discharges has been analysed at multiple radial positions. Across the database the mean plasma parameters such as the electron temperature T_e, magnetic field B_T, electron density n_e, density gradient length L_n, the perpendicular velocity $v_\perp$ and safety factor q_{95} are varied. Here q_{95} is the safety factor at the surface that encloses 95% of the poloidal magnetic flux. Figure 8.3 shows the dependence of l_{eff} on listed parameters in the core region $0.6 < \rho_{\text{pol}} < 0.9$. To exclude the effect of the beam (i.e. of the l_s) the dependence on probing frequency and radial position is also plotted in figure 8.3. A regression analysis has been applied to the database. Although a regression analysis in the log-log scale can provide power law dependencies, it is difficult to use this technique due to the contribution of the detection volume size. Therefore the analysis is performed in linear scale, only. The output of the regression fit are coefficients of linear dependencies and adjusted R-squared R^2_{adj}. Last parameter shows the percentage of the variation which can be explained by a linear relation [146].

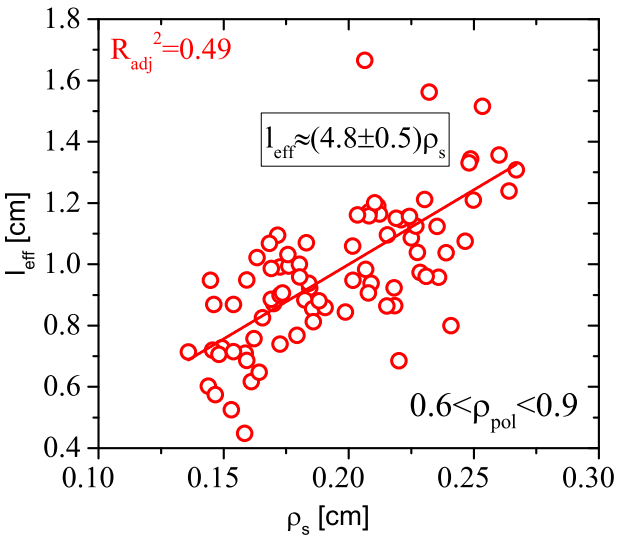

Figure 8.4: The dependence of the effective correlation length on the drift wave scale ρ_s in the core region.

l_{eff} does not correlate strongly ($< 9\,\%$) with density n_e, density gradient length L_n or

safety factor q_{95} (figure 8.3c, d and f). A weak dependence (figure 8.3e) is found on the velocity $v_\perp$ ($\approx 25\,\%$). It is not clear if this dependence has a physical nature or if it is a result of the analysis method, since in the measurement $l_{\text{eff}} = v_\perp \tau_a$. The dependence of l_{eff} on probing frequency and radial position (figure 8.3g and h), which defines l_s, is also weak ($< 7\,\%$). However, a strong correlation is found with electron temperature ($54\,\%$) and magnetic field ($49\,\%$). l_{eff} increases with T_e and decreases with B_T (figure 8.3a and b). This dependence may be attributed to a similar dependence on the drift wave scale $\rho_s = \sqrt{m_i T_e}/eB$ which is theoretically predicted as scale factor of the turbulent eddies. Actually, when l_{eff} is plotted against ρ_s (figure 8.4) a linear dependence is found with $l_{\text{eff}} \approx 5\rho_s$. Figure 8.4 includes different magnetic fields $1\,\text{T} < B_T < 2.2$ T and different temperatures $0.3\,\text{keV} < T_e < 1.5\,\text{keV}$. Note again, that due to the contribution of l_s to l_{eff}, the coefficient of proportionality between $l_\perp$ and ρ_s may be different. In general it is difficult to decouple the contributions of $l_\perp$ and l_s to l_{eff}.

The effective correlation length was also studied in the edge region ($0.97 < \rho_{\text{pol}} < 0.99$). Usually l_{eff} in the edge is higher than in the core (see figure 8.2b). However, here no clear dependence of l_{eff} on physical parameters is found. The data are scattered and do not correlate with any parameter. Figure 8.5 shows the dependence of l_{eff} on electron temperature and velocity.

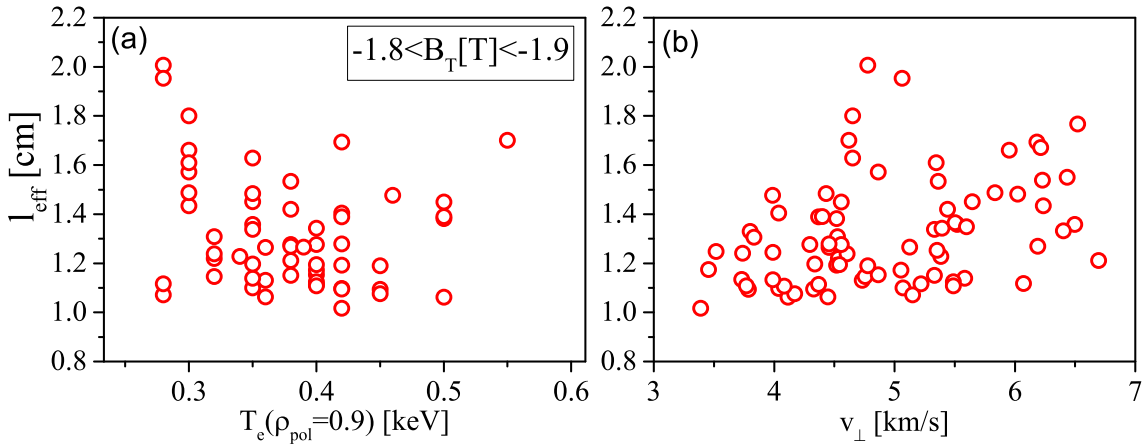

Figure 8.5: The dependence of the effective correlation length in the edge region $0.97 < \rho_{\text{pol}} < 0.99$ on (a) electron temperature calculated at $\rho_{\text{pol}} = 0.9$ and (b) perpendicular velocity.

In the edge region the density fluctuation level is usually high (see figure 8.7a and [90]). Therefore the Born approximation may not be applied and the PCR system operates in a nonlinear regime of reflectometry, where multiple scattering could occur. It is not clear how the nonlinear regime affects the response function of the instrument. It is possible that this process is responsible for the spreading of l_{eff} in the edge.

8.2 Measurement of decorrelation time

8.2.1 Radial τ_d profiles

In contrast to the effective correlation length the measured decorrelation time τ_d seems to be independent of the geometry of the microwave beams based on results from Born approximation (see appendix B). This significantly simplifies the interpretation of τ_d measurements. The radial profile of the decorrelation time τ_d measured with the PCR is shown in figure 8.6a (black points). Here a frequency scan was performed to obtain the radial τ_d profile. The plasma parameters for this discharge are: density $\bar{n} = 2.52 \times 10^{19}$ m^{-3}, magnetic field $B_{T0} = -2.5$ T and plasma current $I_p = 0.6$ MA. The decorrelation time in the core ($0.6 < \rho_{\mathrm{pol}} < 0.9$) of $\tau_d \approx 30$–50 μs is longer than that in the edge ($0.97 < \rho_{\mathrm{pol}} < 0.99$) with $\tau_d \approx 5$–10 μs. This is a typical observation seen in several discharges. The characteristic velocity profile for this case is shown in figure 7.1a. The measured decorrelation time have been compared to the autocorrelation time (red points in figure 8.6). As expected decorrelation time is longer than autocorrelaiton time ($\tau_d/\tau_a \approx 4$–6 in the region without velocity shear). A zoom in the edge region is shown in figure 8.6b, where τ_d depends on ρ_{pol} and decreases in the shear flow region.

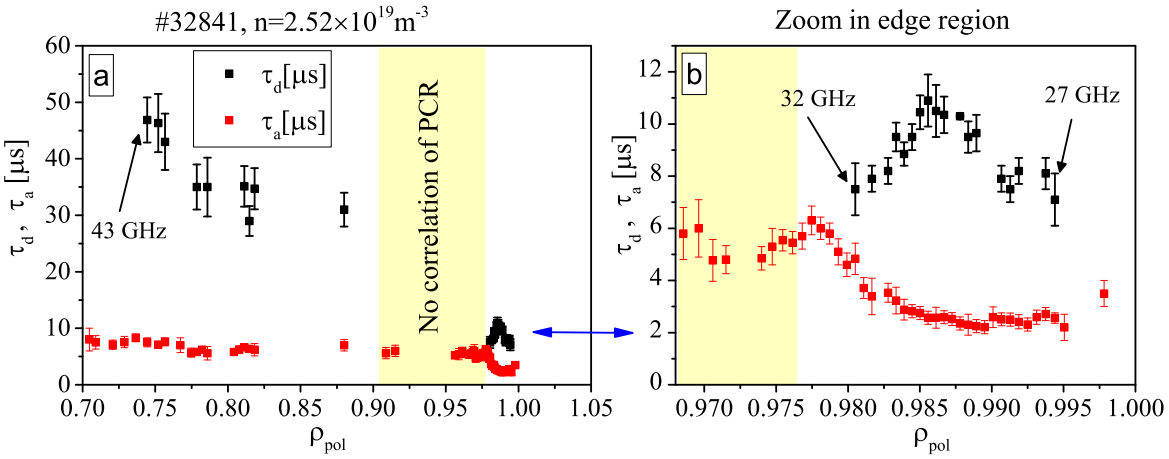

Figure 8.6: (a) The radial decorrelation time τ_d and autocorrelation time τ_a profiles from discharge #32481. (b) Zoom in the edge region of #32481.

The parameters $v_\perp$, α, τ_d and l_{eff}, analysed in this thesis have a gap in the region $\rho_{\mathrm{pol}} = 0.92$–$0.975$, which is related to a loss of correlation at these radii as illustrated by the correlation level for three different separations (8, 24 and 45 mm) from discharge #31427 shown in figure 8.7b. The measured phase fluctuation level $\sigma_\phi \sim \delta n_e/n_e$ (figure 8.7a) in this region remains strong. A possible impact of the probing frequency have been excluded, since for different density profiles the loss of correlation is observed at

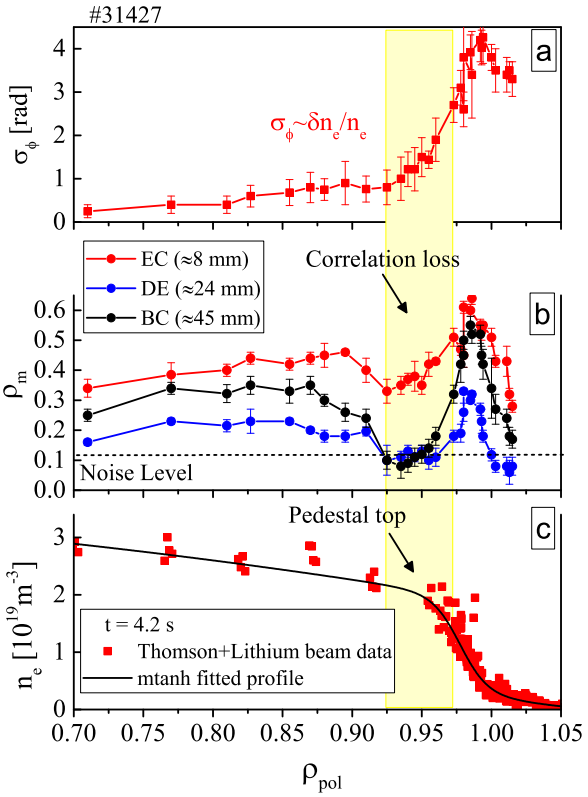

Figure 8.7: (a) Phase fluctuation level ($\sigma_\phi \sim \delta n_e/n_e$). (b) Correlation level for 3 antenna separations (8, 24 and 45 mm). (c) Electron density profile from #31427 at t=4.2s.

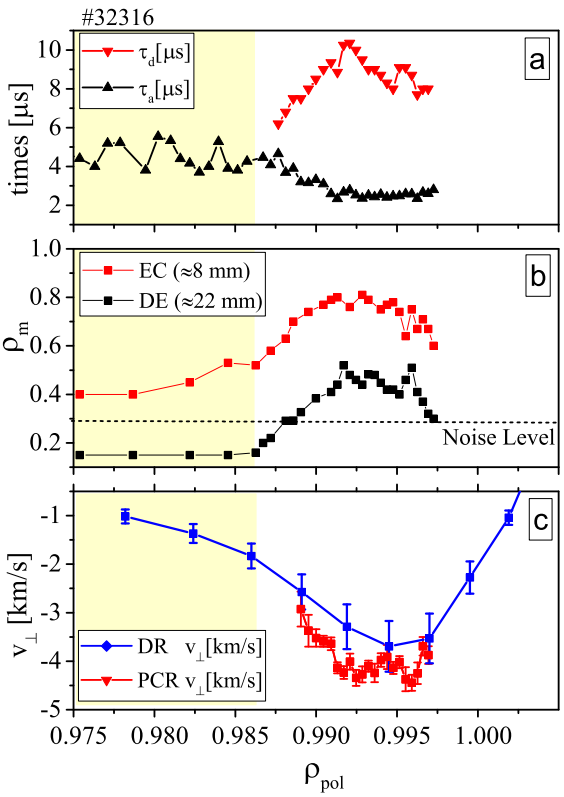

Figure 8.8: Zoom in the edge region of #32316. (a) τ_d and τ_a profiles. (b) Correlation level for 2 antenna separations (8 and 22 mm). (c) Velocity profile $v_\perp$.

different frequencies, but the same radial location. The affected frequency range always corresponds to cut-off positions around the pedestal top (marked in figure 8.7c). Note that the position of correlation loss is inside of the negative shear flow, as measured by DR and PCR systems in figure 8.8c for the same discharge.

A possible mechanism explaining the loss of correlation of the PCR is a decrease of the decorrelation time τ_d in the shear region (red line in figure 8.8a) simultaneously with a increase of the propagation time caused by decrease in $v_\perp$. For the small value of τ_d, eddies on the magnetic surface decorrelate faster than the time needed for the propagation between the measurement volumes and therefore correlation disappears. Doppler reflectometry of course does not lose the measurement capability (figure 8.8c), since it makes use of a single point for the measurement of the perpendicular velocity, only.

This hypothesis may be additionally confirmed by measurement of the autocorrelation

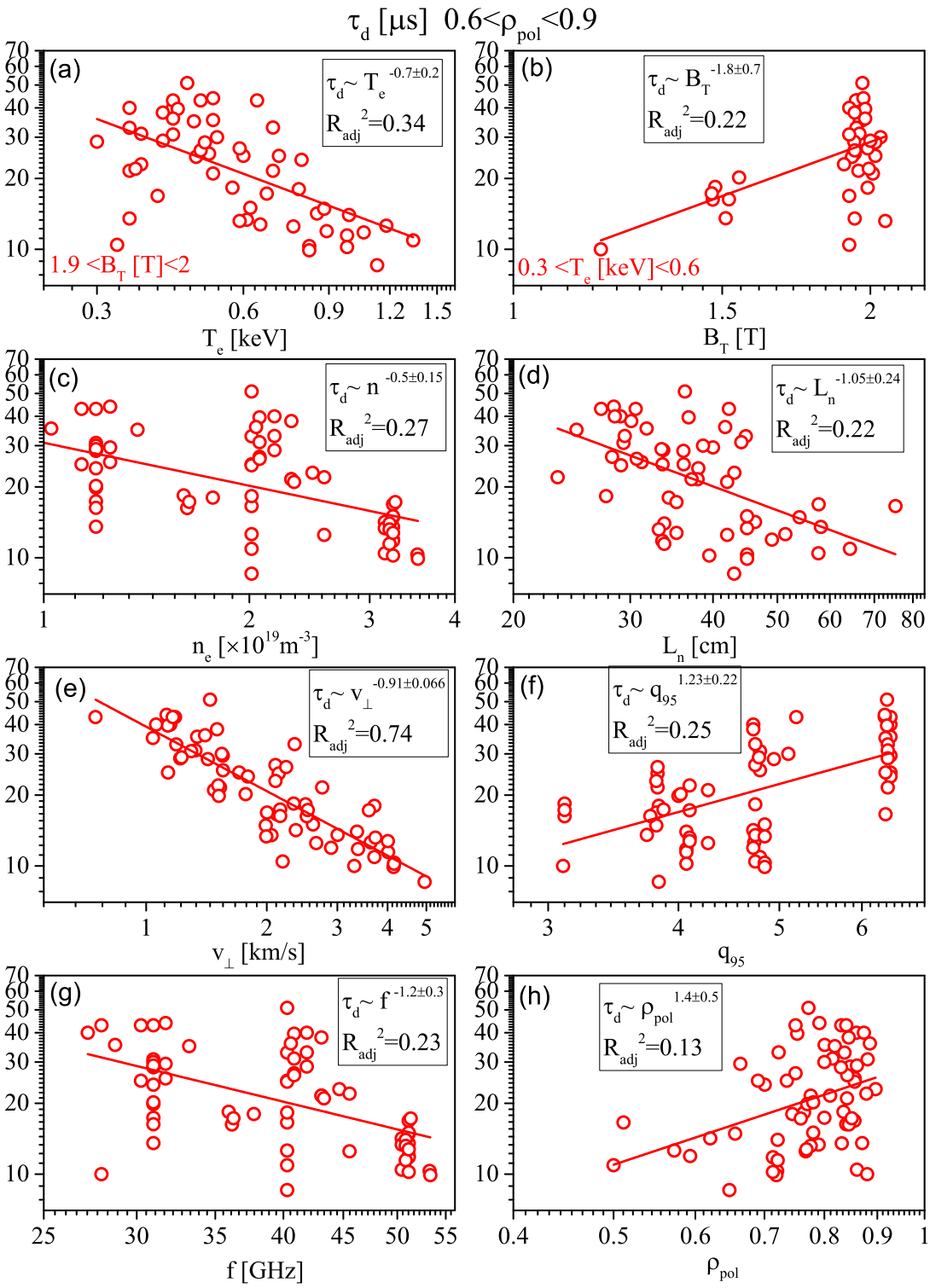

Figure 8.9: The dependence of decorrelation time in the core region $0.6 < \rho_{\mathrm{pol}} < 0.9$ on (a) electron temperature, (b) magnetic field, (c) density, (d) density scale length, (e) perpendicular velocity, (f) safety factor, (g) probing frequency and (h) radial position.

time τ_a (black line in figure 8.8a). τ_a shows an increase towards the shear region, due to the decrease of the velocity according to equation 6.10. However, at the point where $\tau_a \approx \tau_d$ the autocorrelation time doesn't increase anymore and stays constant. This can be explained by the fact that the autocorrelation time (equation 6.10) in this region is dominated by the decorrelation time of the turbulence. Figure 8.8 shows the results for the negative shear region, however, in figure 8.6b similar observations have been obtained for the positive shear as well. The results presented in this section demonstrate that τ_d decreases in the $E \times B$ shear flow region.

8.2.2 The dependence of τ_d on mean plasma parameters

The dependence of τ_d on the mean plasma parameters has also been investigated. Similar to section 8.1.2 a database of 12 discharges at multiple radial positions has been created. Figure 8.9(a–f) shows the dependence of τ_d in the core ($0.6 < \rho_{\mathrm{pol}} < 0.9$) on electron temperature, magnetic field, electron density, gradient length of density, the perpendicular velocity and safety factor q_{95}. The probing frequency and radial position are also plotted in figure 8.9(g–h) across the database. In contrast to section 8.1.2 the regression analysis is performed on the log-log scale. This permits to find power-law dependencies of τ_d. R^2_{adj} gives the variation in percent which can be explained by the power law dependencies [146].

τ_d shows a low level of correlation ($< 25\,\%$) with magnetic field, gradient density scale length, safety factor, probing frequency f and radial position (see figure 8.9b, d, f, g and h). A small level of correlation is found with electron temperature $\tau_d \propto T_e^{-0.7\pm0.2}$ ($\approx 34\,\%$) and density $\tau_d \propto n_e^{-0.5\pm0.15}$ ($\approx 27\,\%$). A very high correlation level ($\approx 74\,\%$) is found with the perpendicular velocity, $\tau_d \propto v_\perp^{-0.91\pm0.066}$. The dependence of τ_d on velocity is clearly visible not only in log-log scale, but also in linear scale (see red points in figure 8.10), where we find $\tau_d \approx 40/v_\perp$ (here τ_d is in μs and $v_\perp$ in km/s).

In the edge E_r well region a correlation of decorrelation time with velocity as $\tau_d \approx 40/v_\perp$ is also observed (see blue dots in figure 8.10). Note that the direction of rotation in the edge (electron diamagnetic direction) is opposite to the core rotation (ion diamagnetic direction). It means that the dependence on $v_\perp$ is fundamental and does not depends on the velocity sign or the plasma region. The edge velocity in the E_r well region of Ohmic plasmas is usually higher compared to that in the core and this explains why τ_d in the edge is lower compared to the core.

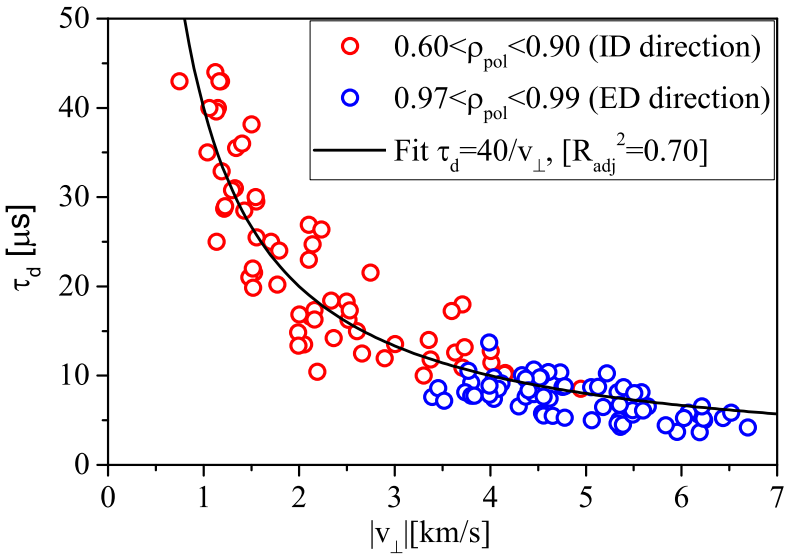

Figure 8.10: Dependence of decorrelation time on the velocity at the core $0.6 < \rho_{\mathrm{pol}} < 0.9$ (red) and edge $0.97 < \rho_{\mathrm{pol}} < 0.99$ (blue) regions of plasma. Sign of velocity in the edge (electron diamagnetic) is opposite to the core (ion diamagnetic).

8.2.3 Comparison of τ_d with theoretical expectations

For fluid turbulence, Xin Zhao analytically calculated τ_d using a quasi-normal approximation of the Navier-Stokes equation taking into account the shear flow [123]. He obtained for small values of the shear flow that the decorrelation time is given by

$$\tau_d^{-2} = \frac{1}{l^2}\int_0^\infty E(k)\mathrm{d}k + \left(\frac{\partial v}{\partial r}\right)^2. \tag{8.1}$$

The equation shows that τ_d depends on both the mean turbulence energy and the shear in velocity. The values of τ_d in the case of plasma turbulence have been discussed by Terry [10]. He suggest that the decorrelation time in plasma, without shear, is given by

$$\tau_d^{-1} = \tau_t^{-1} = \frac{\delta u}{l_r} = \frac{1}{l_r l_\theta}\frac{\delta\phi}{B}. \tag{8.2}$$

Here δu is the fluid velocity and $\delta\phi$ the electric potential fluctuation levels. This time is also called eddy turnover time because it defines the time that an eddy needs to rotate by 2π. The equation 8.2 qualitatively agrees with the first term of equation 8.1, because higher electric potential fluctuations mean a higher turbulence energy. In the strong shear environment Terry suggests that the decorrelation time changes to

coincide with the shear strain time

$$\tau_d^{-1} = \tau_s^{-1} \equiv \frac{l_r}{l_\theta}\frac{\partial v}{\partial r}. \tag{8.3}$$

In terms of the ambient shear rate, Terry suggests that the decorrelation time can be written as the geometric mean $\tau_d = \tau_t^{1/2}\tau_s^{1/2}$.

The dependence of τ_d from equations 8.1 and 8.3 on the velocity shear can explain the decrease of τ_d in the shear region observed in section 8.2.1. However, these equations cannot explain the dependence of τ_d on velocity $v_\perp$. The following hypotheses are proposed to explain the velocity dependency of the decorrelation time $\tau_d \approx 40/v_\perp$:

1. If $v_\perp \propto \partial v_\perp/\partial r$ is fullfield then also a correlation between τ_d and $v_\perp$ is expected. Indeed, equations 8.1 and 8.3 suggest a decrease of τ_d with flow shear, which is in agreement with the measurements. However, a clear correlation between $v_\perp$ and $\partial v_\perp/\partial r$ is not found.

2. The $v_\perp$ can correlate with the turbulence fluctuation level. Both the measured fluctuation level (figure 8.7a) and the perpendicular velocity (figure 7.1a) are higher in the edge E_r well region than in the core. Furthermore it is expected that both turbulence drive and perpendicular velocity depend on gradients in the plasma parameters. In agreement with equations 8.1 and 8.2 the increase in the turbulence fluctuation level will decrease the decorrelation time [123].

8.3 Discussion

In this chapter the PCR was applied to study the decorrelation time τ_d and the effective correlation length, consisting of turbulent perpendicular correlation length and detection volume size $l_{\text{eff}} = \sqrt{l_\perp^2 + l_s^2}$. The results are shown for the core $0.6 < \rho_{\text{pol}} < 0.9$ and the edge $0.97 < \rho_{\text{pol}} < 0.99$ regions of AUG plasmas.

l_{eff} varies from 0.6 to 1.4 cm in the core and from 1.0 to 2.0 cm in the edge. The contribution of the detection volume size l_s^2 to l_{eff}^2 is significant (50–70 %) and therefore the extraction of $l_\perp$ from l_{eff} is difficult. Nevertheless, the dependence of l_{eff} on mean plasma parameters is studied. In the core it correlates with electron temperature T_e and magnetic field B_T such that $l_{\text{eff}} \approx 5\rho_s \propto \sqrt{T_e}/B_T$. No correlation of l_{eff} with mean plasma parameters in the edge is found. However, l_{eff} in the edge is higher than in the core. This might be explained by a stretching of turbulent eddies by the sheared $E \times B$ flow in the edge.

In the core $\tau_d \approx$ 10–50 μs is higher than in the edge $\tau_d \approx$ 4–10 μs. It was found that τ_d correlates with the perpendicular velocity as $\tau_d \approx 40/v_\perp$ (τ_d is in μs and $v_\perp$ in

km/s), for both core and edge regions. The flow velocity in the E_r well region of Ohmic plasmas is usually higher than the core and thus explains a lower τ_d in this region. It is also observed that τ_d additionally decreases in the shear flow layer in agreement with theory expectations.

An important limitation of the method is related to the finite value of l_s. In order to improve the measurement resolution of the PCR by decreasing the detection volume size l_s a new antenna cluster can be designed in future. The optimal horn geometry can be found using calculations of l_s in Born approximation, as described in appendix B. Different antenna mouth sizes and curvature radii can be tested to find the optimal geometry of the antenna. An alternative possibility to improve the resolution of the PCR is to use the upper X-mode cut-off. The frequencies satisfying this cut-off are significantly higher. This would allow the use of smaller aperture antennas, which decreases l_s. However, it should be noted, that even small density fluctuations in X-mode can cause a transition to the nonlinear regime of reflectometry, where intrepretation of PCR measurements is more challenging.

The presented studies focus on lower single null L-mode AUG plasmas with ion ∇B drift oriented towards the X-point. Since the L-H transition power threshold depends on the ∇B drift direction [145] it is important to extent these studies to plasma configurations where the ∇B direction is reversed. Different confinement regimes such as the I-mode and the H-mode are also of high interest. Although the application of the PCR system in H-mode is difficult due to edge localized modes, the conditional averaging technique may be applied to obtained ELM averaged values of l_{eff} and τ_d.

9 Turbulence characterization during the LOC-SOC transition

Several tokamaks report a linear increase of the energy confinement time τ_E of Ohmic plasmas with the line averaged electron density $\bar{n}_e$ [12, 58, 147, 148]. However, above a critical density τ_E saturates and does not increase significantly anymore. The corresponding regimes are named Linear Ohmic Confinement (LOC) and Saturated Ohmic Confinement (SOC) respectively. The transition from LOC to SOC happens at a certain effective collisionality $\nu_{\text{eff}} = \nu_{ei}/(c_s/R) \propto n_e/T_e^2$ (ν_{ei} is the electron-ion collision frequency and c_s the sound speed) [58]. In addition the LOC-SOC transition is observed for different plasma currents I_p at different $\bar{n}_e$ [58, 149] ($\bar{n}_{LOC-SOC}\,[10^{19}\ \text{m}^{-3}] \approx 3I_p\,[\text{MA}]$ for AUG plasma) related to different Ohmic heating in the plasma. Figure 9.1 shows the dependence of τ_E on $\bar{n}_e$ for two discharges at different values of I_p at AUG.

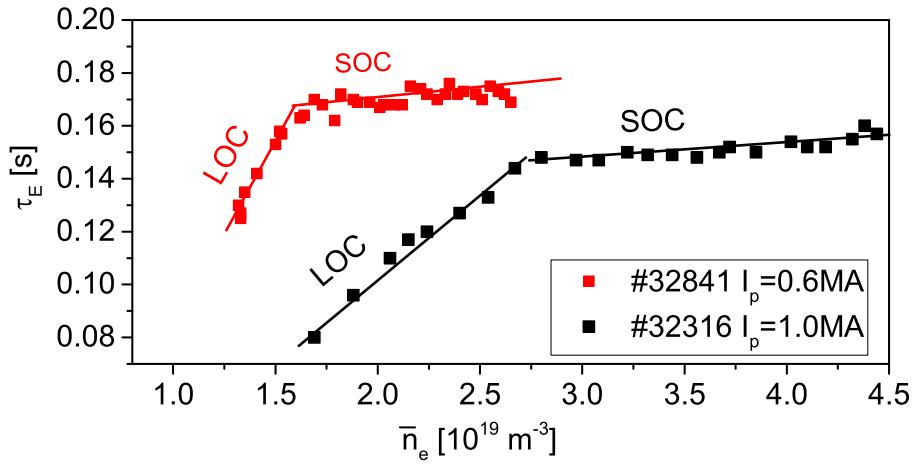

Figure 9.1: Energy confinement time versus electron density for two discharges with different plasma currents at AUG.

One hypothesis for the LOC-SOC transition is a change in the dominant turbulence from trapped electron mode (TEM) to the ion temperature gradient (ITG) regime [12] associated with the change of collisionality ν_{eff}. An increase in ν_{eff} leads to (i)

the de-trapping of the trapped particles (reducing TEM drive) and (ii) an increase in the ion temperature gradient ∇T_i (increasing ITG drive). The increase of ∇T_i with ν_{eff} has its origin in an improved coupling between electrons and ions [58]. An indication for a possible TEM-ITG transition due to the increase of ν_{eff} has been observed in GS2 gyro-fluid turbulence simulations and from heat pulse propagation analyses [150]. However, the evolution of turbulence parameters during the transition is poorly documented. This chapter reports the correlation properties of turbulent density fluctuations during the LOC-SOC transition from the PCR system.

9.1 Rotation in different regimes

Even in the absence of an external torque (e.g. due to NBI) the $v_{E\times B}$ velocity in the L-mode plasma core is defined not only by the $-\nabla p_i/(enB)$ term, but has an additional component due to intrinsic toroidal rotation u_{Ti} of the main ions (see section 2.6). It was observed that u_{Ti} and $v_{E\times B}$ reverse direction in the plasma core close to the point of the LOC-SOC transition [58, 147, 148]. Several symmetry breaking mechanisms have been proposed to explain the generation of u_{Ti} [151]. One of them is the residual stress which is due to tilting of the turbulent eddies in the radial-poloidal plane [152]. The tilting appears due to the dependence of the turbulence phase velocity v_{ph} on the underlying instability and changes sign for different turbulence regimes (TEM and ITG), resulting in a reversed direction of the residual stress. This may reverse the direction of u_{Ti} and $v_{E\times B}$ as well if the residual stress is sufficiently large. However, it

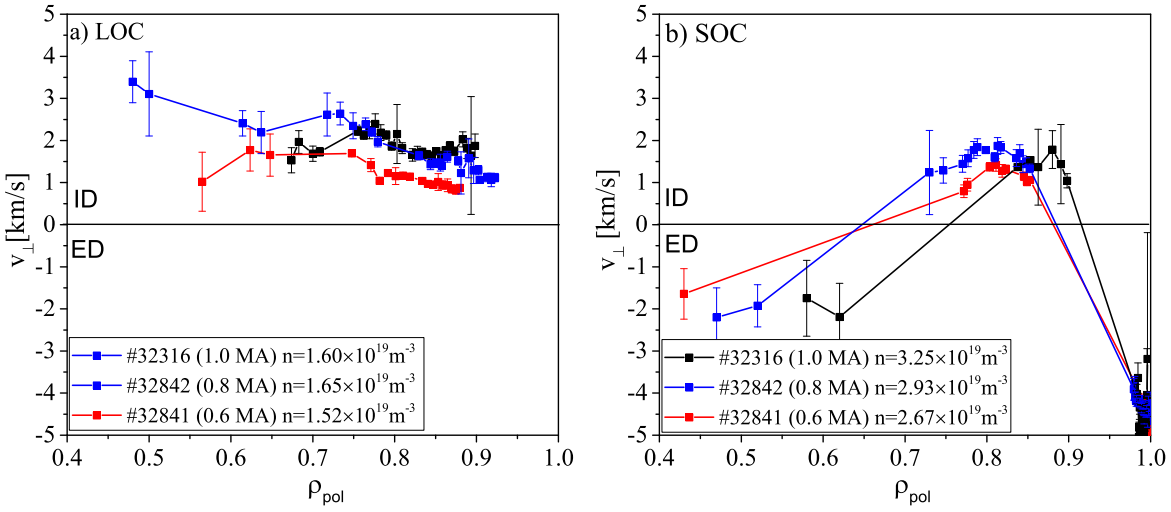

Figure 9.2: Perpendicular velocity profiles measured by the PCR diagnostic.

is not clear if this effect plays a dominant role [58].

The PCR system permits to measure the fluctuation propagation velocity $v_\perp = v_{E\times B} + v_{ph}(k_\perp)$ with $k_\perp = 0$–3 cm^{-1} by means of time delay estimations. Figure 9.2 depicts profiles of $v_\perp$ obtained using frequency sweeps in the LOC and SOC regimes of AUG discharges #32841 ($I_p = 0.6$ MA), #32842 ($I_p = 0.8$ MA) and #32316 ($I_p = 1.0$ MA). In the LOC regime $v_\perp$ is in the ion diamagnetic (ID) direction at the majority of the radial positions ($\rho_{\text{pol}} < 0.9$). It should be noted that rotation in the ID direction is observed even without external momentum input. $v_\perp$ in the SOC regime inverts to the electron diamagnetic (ED) direction for $\rho_{\text{pol}} < 0.65$, however, it stays in the ID direction for $0.65 < \rho_{\text{pol}} < 0.9$. Note that for the plasma region $0.6 < \rho_{\text{pol}} < 0.7$ in SOC $v_\perp$ cannot be measured due to the low correlation level between different antennas. This is believed to be related to a large propagation time compared to the decorrelation time τ_d of the turbulence (similar to the observations in section 8.2.1). These observations are in agreement with studies by Doppler reflectometry [52] and the CXRS diagnostics [58].

The PCR profiles have been compared with measurements of $v_{E\times B}$ from the CXRS diagnostic [153, 154] where agreement has been obtained suggesting that the turbulence phase velocity is small in both regimes. Gyro-kinetic simulations predict a phase velocity of $v_{ph} < 1.0$ km/s [37, 52]. Such small values are difficult to measure taking into account the error bars of both diagnostics. Further analysis of the density fluctuations have been performed in the region $0.65 < \rho_{\text{pol}} < 0.9$ where $v_\perp$ remained in the ID direction in both regimes.

9.2 Turbulence properties in different regimes

If the turbulence regime changes from TEM to ITG one might expect a change in the correlation properties of the turbulent eddies, such as the perpendicular correlation length $l_\perp$ and the decorrelation time τ_d. In this section an analysis of the effective correlation length l_{eff} and decorrelation time τ_d are performed with PCR for the region $0.65 < \rho_{\text{pol}} < 0.9$. The analysis is based on the same discharges as in the previous section, but additionally was included #32844 ($I_p = 1.0$ MA). The results for both LOC and SOC regimes are depicted in figure 9.3. $l_{\text{eff}} \approx 5\rho_s$ is found in the plasma core. This dependence is in agreement with results from section 8.1.2. The dependence of l_{eff} does not change between LOC and SOC regimes, however, l_{eff} in the SOC regime is smaller. This is probably attributed to the smaller electron temperature in the SOC regime (see figure 3.5). The independence of l_{eff} on the turbulent regime is unexpected, but could also be due to similar injection scales for both TEM and ITG modes. The decorrelation time τ_d in figure 9.3b is found to be dependent on velocity as $\tau_d \approx 40\, v_\perp^{-1}$

in agreement with section 8.2.2. Similar dependencies are found in both LOC and SOC regimes, however, τ_d in the SOC regime is slightly smaller.

The results obtained in this section will be used for comparison with nonlinear gyrokinetic simulations in the future.

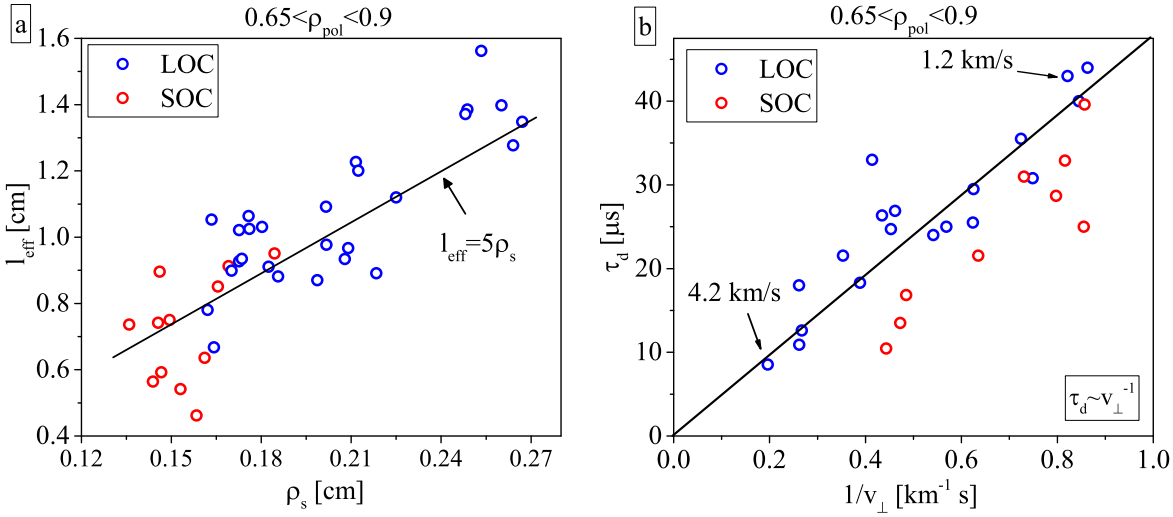

Figure 9.3: (a) The effective correlation length l_{eff} and (b) decorrelation time τ_d (b) in different regimes.

9.3 Role of quasi coherent structures

In the Tore Supra tokamak a Quasi-Coherent (QC) mode in the density fluctuation spectra[1] has been observed in the LOC regime at low ν_{eff}. The mode disappears in the SOC regime [155]. Similar observations were obtained recently at HL-2A and J-TEXT tokamaks [156]. A QC mode is defined as a broad spectral peak with a full-width comparable to the mean frequency. It was suggested that QC mode appears as nonlinear features of a developing TEM instability [155]. Nonlinear gyro-kinetic GENE simulations have been performed for the conditions of the Tore Supra discharges and QC mode has been found in the density fluctuations spectra for TEM driven turbulence, but not for ITG driven turbulence [157]. The reason why TEM driven turbulence exhibits a QC modes is not investigated and needs further studies.

This section reports on the observation and properties of QC modes at AUG in the LOC regime. The analysis of experimental density fluctuation spectra is performed over $\rho_{\text{pol}} = 0.65$–0.9 where $v_\perp$ remains approximately constant (ID direction) in both regimes. Figure 9.4a shows density fluctuation power spectrum measured at $\rho_{\text{pol}} \approx 0.75$

[1]The measurements were obtained using a reflectometry diagnostic operated in X-mode.

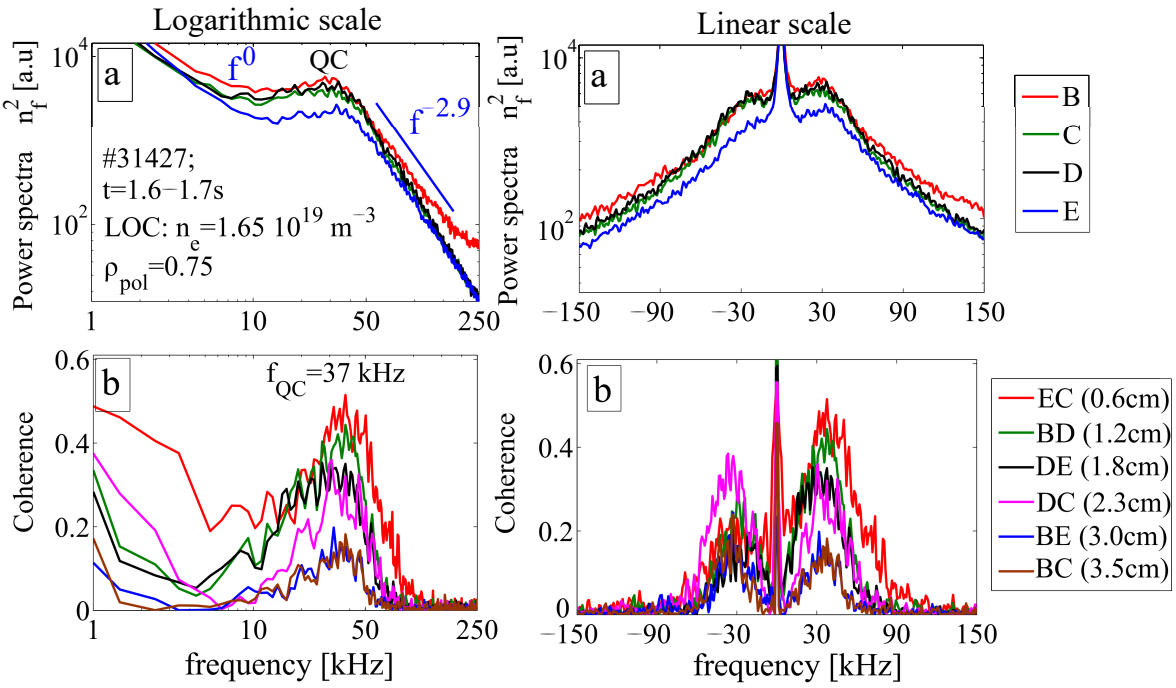

Figure 9.4: (a) Power spectrum of density fluctuations (δn_e) measured from 4 antennas in logarithmic (left) and linear (right) scale. (b) Coherence between antennas at different perpendicular separation.

from 4 different antennas in logarithmic (left) and linear (right) scale. Each spectrum is calculated with 1024 samples and averaged over 100 windows without overlap. The separation between the measurements in the perpendicular direction amounts to $\varepsilon_\perp = (0.6, 1.2, 1.8, 2.3, 3.0, 3.5)\,\mathrm{cm}$. All spectra look similar and the QC is barely visible. However, calculating the spectral coherence $\gamma(f)$ from equation 6.22 between density fluctuations with different separations shows a clear QC peak (figure 9.4b). The result suggest that the QC mode is not clearly visible in the density fluctuation spectra because it is weak and partly hidden by uncorrelated broadband density fluctuations. Only a coherence analysis allows to highlight this mode. In [157, 158, 159] full wave simulation of the reflectometry using turbulence from the GENE code have shown that due to 2D effects of reflectometry the QC mode can be weaker in the phase fluctuation spectrum, than in the real density fluctuations. The QC mode in Tore Supra was stronger [157], perhaps because the collisionallity was lower. Note that the QC peak is located around the knee point of the density fluctuation spectra. This could be an indication of a connection of the QC mode with the injection instability. It is worthwhile to note that if the QC mode exists, the low frequency components ($4\,\mathrm{kHz} < f < 10\,\mathrm{kHz}$) of the spectra have low level of correlation.

At AUG the QC structures can be observed at several radii simultaneously. Figure 9.5b shows the spectral coherence amplitude γ_{BD} as function of time for antenna combimation BD ($\varepsilon_\perp \approx 1.2$ cm). During the discharge a density ramp was performed and the probing frequency was fixed at $f = 31$ GHz. Due to the dependence of the reflection position on density the radial position is scanned. Figure 9.5a shows the corresponding measurement position as the density increases from $\bar{n}_e = 1.5 \times 10^{19}$ to 2.0×10^{19} m^{-3}. Despite of a small density variation the plasma remains in the LOC regime. The QC structure in figure 9.5b is observed between $\rho_{\mathrm{pol}} = 0.65$ and 0.9. This region corresponds to safety factor values between $2 < q < 3$. The frequency of the

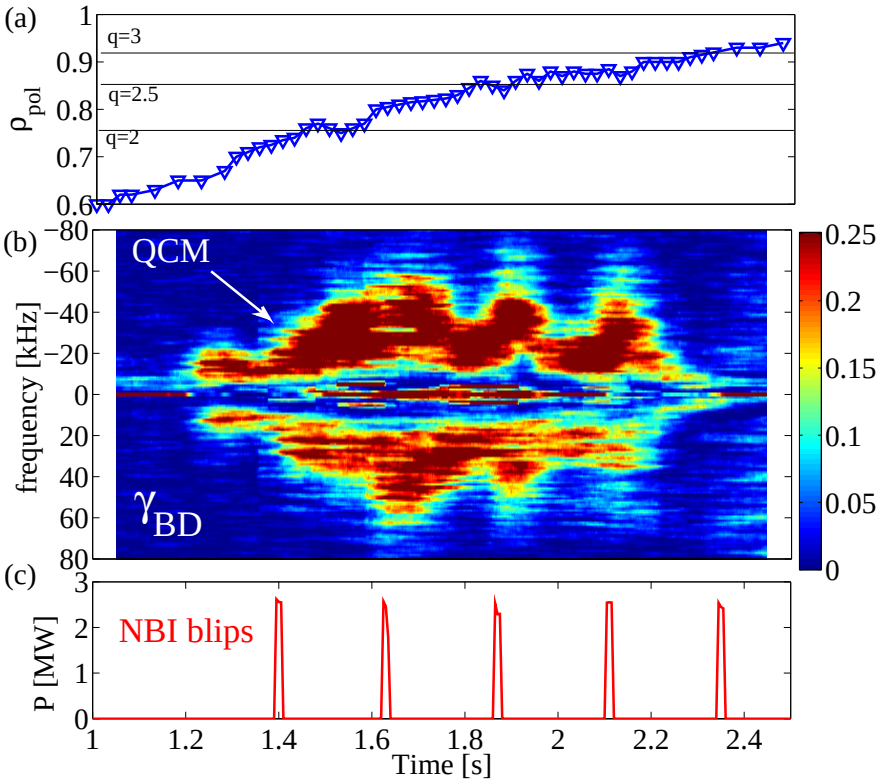

Figure 9.5: (a) The radial position of the measurement from discharge #31427 ($I_p = 0.8$ MA) as function of time. (b) The spectral coherence amplitude for the combination BD. The spectrum is calculated from 1024 samples and averaged over 100 windows. c) Applied NBI blips.

QC mode is not constant but shows a variation connected to the local $v_\perp$ variation due to applied NBI blips (figure 9.5c). The absence of the QC peak deeper in the core ($\rho_{\mathrm{pol}} < 0.6$) may be related to a zero rotation, when the QC peak approaches zero frequency and thus is not resolvable.

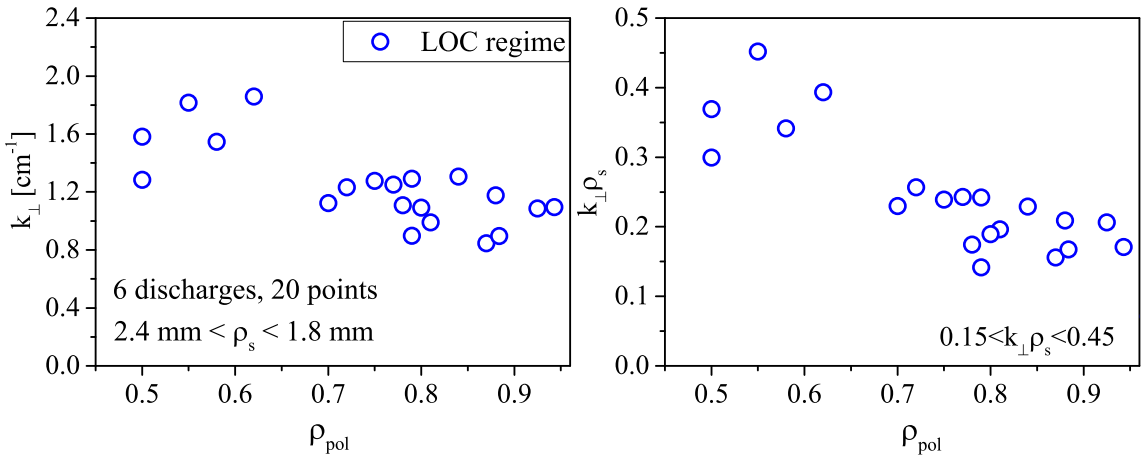

Figure 9.6: Radial dependence of the perpendicular wavenumber $k_\perp$ and normalized perpendicular wavenumber $k_\perp \rho_s$ of the QC mode.

The perpendicular wavenumber of the QC structures has been calculated using the measured velocity as $k_\perp = 2\pi f_{QC}/v_\perp$. The dependence of $k_\perp$ and $k_\perp$ normalized to the local drift wave scale $\rho_s = \sqrt{T_e m_i}/eB_T$ are shown in figure 9.6. The dataset consists of 6 discharges, where the ρ_s value was varied between 1.8 and 2.4 mm. It is interesting to note that the value of $k_\perp \rho_s \approx 0.2$–$0.4$ is close to the most unstable TEM mode predicted by gyrokinetic simulations [155, 160].

Figure 9.7 shows the measured density fluctuation power and coherence spectra between different antennas obtained for different time points during the LOC-SOC transition. Here a frequency scan was performed for discharge #32841 ($I_p = 0.6$ MA) (see figure 9.1) to obtain the same reflection position at different $\bar{n}_e$. The spectra are calculated with 512 samples and averaged over 20 windows. As expected the QC peak is visible in the coherence spectra for the LOC case (figure 9.7a). In figure 9.7b a weak QC peak is also visible in the coherence, despite of a previous transition to the SOC regime. However, at very high collisionality (figure 9.7c) the local QC peak disappears. Therefore it can be concluded that the QC peak indeed disappears with collisionality, but not exactly at the point of the global LOC-SOC transition. With the present set of data it is difficult to answer if QC modes are related to a expected change of the main turbulence drive from TEM to ITG modes.

9.4 Discussion

In this chapter the properties of density fluctuations have been studied over $0.65 < \rho_{\mathrm{pol}} < 0.9$ in the LOC and SOC regimes. The measured phase velocity is small (< 1 km/s)

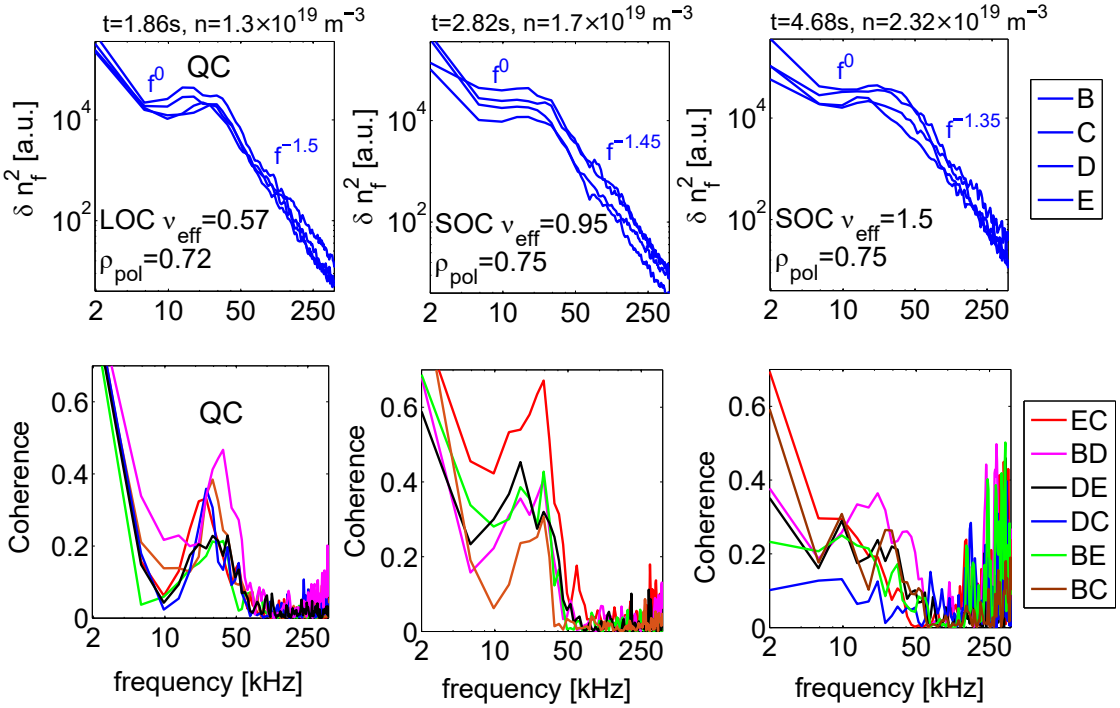

Figure 9.7: Measured spectra (top) and coherence (bottom) at different collisionality in plasma from discharge #32841($I_p = 0.6$ MA).

and therefore its extraction from the difference between $v_\perp$ and $v_{E\times B}$ is difficult taking into account the error bars of the PCR. The perpendicular correlation length and decorrelation time of the eddies do not change their dependence on plasma parameters between the two regimes. Furthermore, the existence of core located QC modes (in the coherence spectra) have been found in the LOC regime. The perpendicular wavenumber of the QC modes and their radial localization were presented. The perpendiculars wavenumber is consistent with that of unstable modes predicted by simulations of TEM turbulence. The QC mode disappears with increasing collisionality, however, not exactly at the LOC-SOC transition. Hence, the explanation of the LOC-SOC transition by a sudden change of the turbulence regime may be an oversimplification.

It should be noted that the presented results are preliminary and more studies are needed. The observations could be used for a detailed cross-comparison with nonlinear gyro-kinetic turbulence simulations. This may help in explaining the QC mode and its impact on particle and energy transport. From the experimental point of view a transition from TEM to ITG can be studied via ECRH rather than via a density scan. Such experiments are more convenient for reflectometry measurements because the coliisionality can be varied over a wide range for a fixed measurement position.

10 Conclusions and outlook

The aim of this thesis was to investigate the turbulent density fluctuations and their interaction with E×B drift velocity shear in low confinement mode (L-mode) plasmas of the ASDEX Upgrade (AUG) and TEXTOR tokamaks. The understanding of their nature and properties is of fundamental importance because they cause enhanced radial transport of particles and energy and thereby degrade magnetic confinement of plasma. In this work the correlation characteristics of density fluctuations such as perpendicular correlation length $l_\perp$ (characteristic size of the turbulent eddies), the decorrelation time τ_d (characteristic lifetime of the turbulent eddies), the inclination of the eddy α in poloidal-toroidal plane, being a measure of the pitch angle of magnetic field lines, and the perpendicular velocity $v_\perp$ are investigated.

For the presented studies, during this thesis, a new poloidal correlation reflectometry (PCR) diagnostic was developed and installed at AUG, which measures the reflected microwave beam with a cluster of 4 receiving antennas, distributed poloidally and toroidally with respect to the launching antenna. The varitation in received reflectrometry signals allows the measurement of density fluctuations at 4 positions separated by small distances in the poloidal and toroidal directions. The system now routinely provides measurements over both Ka- (24–37 GHz) and U-bands (40–57 GHz) which cover a cutoff density range of 0.9–4×10^{19} m^{-3} for O-mode polarization. To evaluate the density fluctuation properties, such as $v_\perp$, α, $l_\perp$ and τ_d, numerical algorithms using cross-correlation and spectral coherence analysis have been developed. All measurements were interpreted taking into account the transfer function of reflectometry in the Born approximation.

Conclusions

The typically measured perpendicular velocity profile of a low collisionality L-mode plasmas $v_\perp = v_{E\times B} + v_{ph}$, composed of the background $E \times B$ drift and the intrinsic phase velocity of the turbulence, is in the ion diamagnetic direction in the plasma core, $0.6 < \rho_{\mathrm{pol}} < 0.92$, but in the electron dimagnetic direction in the plasma edge, $0.97 < \rho_{\mathrm{pol}} < 1$. The region in-between has a negative $v_\perp$ shear layer. The dispersion relation of propagating density fluctuations is found to be almost linear between perpendicular wavenumbers of $k_\perp = 1$ and 12 cm^{-1} in both the core and

edge regions. $v_\perp$ profiles in the core show reasonable agreement with $v_{E\times B}$ calculated from neoclassical theory. However, a small difference of the order of 0.5 km/s (in the electron diamagnetic direction) between $v_\perp$ and the neoclassical estimate of $v_{E\times B}$ is observed in the plasma edge, which may be connected to a turbulent phase velocity v_{ph}. The measured phase velocity in the edge, however, is significantly lower than that predicted for linear electron drift waves ($v_{ph} \approx 4$ km/s) for the presented discharge. Nonlinear simulations of edge turbulence with the GEMR code have been performed to investigate this difference. GEMR is found to reproduce the small phase velocity. An understanding of the physical mechanism leading to the small phase velocity will be an important task for theory and future experiments.

The turbulent density structures are found to be nearly aligned with the mean magnetic field lines. The measured magnetic field line pitch angle α from the inclination of the eddies shows the expected inversion with the reversal of the direction of the magnetic field B_{T0} or the plasma current I_p. The calculation of local safety factor q profiles at the TEXTOR tokamak from α measurements also yields the expected shape. However, comparison of α measurements at AUG with results from the equilibrium reconstruction code CLISTE suggests an additional angle of the order of 2–3 ° at the pedestal location. This additional angle decreases towards the core and towards the edge. A possible explanation for the deviation is a reduced value in the parallel correlation length when density structures decline from magnetic field lines. For the considered plasma condition at the pedestal position and a measured wavenumber $k_\theta \approx 0.5$–1 cm^{-1} a parallel correlation length of $l_\parallel \approx 2$–4 m is needed to reconcile the experimental results with the equillibrium calculation.

It is shown that the Geodesic Acoustic Mode (GAM) can be detected and studied using the envelope of high frequency density fluctuations measured by the PCR system. The observed envelope modulation and GAM velocity component from Doppler reflectometry measurements are in phase. This is in variance with the phase shift of $\pi/2$ observed on the tokamak JFT-2M [139]. Hence an energetic coupling between small scale turbulence and the GAM cannot to be confirmed at ASDEX Upgrade for the case of the analyzed discharges.

The measured effective correlation length $l_{\text{eff}} = \sqrt{l_\perp^2 + l_s^2}$, with the turbulence correlation length $l_\perp$ and the detection volume size l_s, is found to vary from 0.6 to 1.4 cm in the core and from 1.0 to 2.0 cm in the edge. It is shown that the contribution of l_s^2 to l_{eff}^2 is significant (50–70 %) and therefore the extraction of $l_\perp$ is difficult. Nevertheless, the dependence of l_{eff} on mean plasma parameters was studied. l_{eff} in the core is found to scale as $l_{\text{eff}} \approx 5\rho_s \propto \sqrt{T_e}/B_T$ as theoretically expected for the size of turbulent eddies. No correlation of l_{eff} with mean plasma parameters in the edge is found, however, the values are higher compared to the core values. This might be explained by a stretching

of the turbulent eddies by the sheared $E \times B$ flows present in the edge.

The decorrelation time of the eddies in the core of $\tau_d \approx 10$–$50\,\mu$s is found to be longer than in the edge $\tau_d \approx 4$–$10\,\mu$s. The regression analyses between τ_d and mean plasma parameters have shown that τ_d correlates with the perpendicular velocity as $\tau_d \approx 40/v_\perp$ (τ_d is in μs and $v_\perp$ in km/s), for both core and edge regions. In the strong flow shear region τ_d additionally decreases, that leads to lost of correlation between different antennas. This is in agreement with theoretical expectations.

Finally, the density fluctuations have been studied in two different confinement regimes: linear Ohmic confinement and saturated Ohmic confinement. The measured phase velocity is small ($< 1\,$km/s) and therefore its extraction from the difference between $v_\perp$ and $v_{E\times B}$ is difficult taking into account the error bars of the PCR. The perpendicular correlation length and decorrelation time of the eddies do not change their dependencies on plasma parameters between the two regimes. Furthemore, the existence of the core located quasi coherent (QC) modes in the coherence spectra at low collisionality was observed. The radial localization of the QC modes was presented. The scale of the modes of $k_\perp \rho_s \approx 0.2$–$0.4$ is found to be close to that of the most unstable trapped electron mode (TEM) predicted by gyrokinetic simulations. The QC mode disappears with increasing collisionality, but not exactly at the LOC-SOC transition. With the present set of data it is difficult to answer if QC modes are related to a expected change of the main turbulence drive from TEM to ion temperature gradient modes.

In summary, in this thesis it is shown that poloidal correlation reflectometry can be used to reliably measure the turbulence parameters such as the perpendicular velocity, the perpendicular correlation length, the decorrelation time and the inclination of the turbulent eddies, being a measure of the magnetic field pitch angle. Here the diagnostic has been used to study these parameters in the edge region of ASDEX Upgrade and TEXTOR tokamaks. The characterization of turbulence structure in the edge of fusion plasma from this work can be used as basis of a detailed comparison with turbulence simulation codes. This will help to test the physical models in these codes and to explain formation of the turbulence and the associated radial transport.

Outlook

The results obtained during this thesis leave some unanswered questions. The small phase velocity in the edge of AUG ($\rho_{pol} = 0.98$) from both measurements and GEMR turbulence simulation is not fully understood and needs further investigation. The gradients of the density and temperature can be varied in the GEMR code in the future to cross-check for possible transitions between different unstable modes. Furthermore, the measurements of the perpendicular correlation length and decorrelation time should

be compared to turbulence simulations. To check for possible diagnostic effects, a synthetic PCR diagnostic (e.g. using the Born approximation) can be applied to simulated data in order to enable cross-comparisons of equivalent quantities.

The presented studies focus on lower single null L-mode plasmas with the ion ∇B drift oriented towards the X-point. Since the L-H transition power threshold depends on the ∇B drift direction [145] it is important to extent these studies to plasma configurations where the ∇B direction is reversed. Furthermore the measurement of turbulent quantities over the L-H mode transition may help to understand transition from a microscopic point of view, i.e. from observations of changes in the turbulence characteristics. Different confinement regimes such as the I-mode [167, 168] and the I-phase [117] are also of high interest. The dynamics of the pitch angle during H-mode is also of importance. Here, a conditional averaging technique may be applied to obtain ELM averaged measurements. Knowledge of the pitch angle profile is particularly important for studying bootstrap current dependences [161], internal transport barrier formation [162], and the physics of magnetohydrodynamic (MHD) modes [163]. Although the temporal resolution of the pitch angle measurements is limited by statistics, it can be improved using advanced algorithms for time delay calculation such as the generalized cross-correlation phase transform [138] (PHAT method).

The PCR diagnostic installed during this thesis was applied to investigate the perpendicular correlation of density fluctuations only. Recently, a new radial channel was added to PCR system. This permits the investigation of turbulent structures simultaneously in the perpendicular and radial directions. Furthermore, long range correlation measurements between two independent reflectometers at AUG: the O-mode PCR located in toroidal sector 2, and an O-mode reflectometer system in toroidal sector 5 [142, 144] may be used to obtain the parallel correlation length. Thus, structures can be studied in all dimensions.

The measurement methodology developed in this thesis can be also applied to a recently installed multichannel reflectometer in the ICRF antenna [164, 165]. Such measurements can be used to cross-check results obtained in this thesis. Last, but not least, the PCR diagnostic can be applied not only for turbulence structure measurements but also for studies of the geodesic acoustic mode (e.g. using envelope technique) or long-wavelength MHD instabilities. Obviously there is a lot of interesting physics that can be investigated with the PCR system!

Bibliography

[1] United Nations, Department of Economic and Social Affairs, Population Division, http://www.un.org/esa/population

[2] Statistical Review of World Energy, http://www.bp.com/

[3] World Energy Council 2013, World energy resources: 2013 survey

[4] Hansen J, Ruedy R, Sato M and Lo K 2010 "Global surface temperature change", *Rev. Geophys.* **48**, RG4004

[5] Wesson J 2004 "Tokamaks", Third Edition, Clarendon Press, Oxford

[6] Freidberg J P 2007 "Plasma physics and Fusion Energy", Cambridge University Press, 2007

[7] International Thermonuclear Experimental Reactor, https://www.iter.org

[8] Tamm I E, Sakharov A D 1959 "Theory of the magnetic thermonuclear reactor, part 1–3", New York: Pergamon

[9] Stroth U 2011 "Plasmaphysik", Vieweg+Teubner Verlag

[10] Terry P W 2010 "Suppression of turbulence and transport by sheared flow", *Rev. Mod. Phys.* **72**, 109

[11] Hugil J 1983 "Transport in tokamaks – a review of experiment", *Nucl. Fusion* **23**, p.331

[12] Wagner F, Stroth U 1983 "Transport in toroidal devices-the experimentalist's view", *Plasma Phys. Control. Fusion* **35**, p.1321

[13] Waltz R E, Candy J M 2002 "Gyrokinetic turbulence simulation of profile shear stabilization and broken gyroBohm scaling", *Phys. Plasmas* **9**, p.1938

[14] General Atomics Fusion Group, https://fusion.gat.com/theory/Gyromovies

[15] Görler T, Lapillonne X, Brunner S, Dannert T, Jenko F, Merz F, Told D 2002 "The global version of the gyrokinetic turbulence code GENE", *Journ. of Comp. Phys.* **230**, p.7053

[16] Janhunen S 2013 "Gyrokinetic particle simulation for thermonuclear plasma turbulence studies in magnetic confinement", *PhD thesis*, Aalto University, Finland

[17] Zweben S J, Scott B D, Terry J L, LaBombard B, Hughes J W and Stotler D P 2009, "Comparison of scrape-off layer turbulence in Alcator C-mod with three dimensional gyrofluid computations", *Phys. Plasmas* **16**, 082505

[18] Manz P, Ribeiro T T, Scott B D, Birkenmeier G, Carralero D, Fuchert G, Müller S H, Stroth U, Wolfrum E 2015 "Origin and turbulence spreading of plasma blobs", *Phys. Plasmas* **22**, 022308

[19] Wagner F et al 1982 "Regime of Improved Confinement and High Beta in Neutral-Beam-Heated Divertor Discharge of the ASDEX tokamak", *Phys. Rev. Lett.* **49**, 1408

[20] Ryter F, Pütterich T, Reich M, Scarabosio A, Wolfrum E, Fischer R, Gemisic Adamov M, Hicks N, Kurzan B, Maggi C, Neu R, Rohde V, Tardini F and the ASDEX Upgrade TEAM 2009 "H-mode threshold and confinement in helium and deuterium in ASDEX Upgrade", *Nucl. Fusion* **49**, 062003

[21] Ryter F, Rathgeber S K, Barrera Orte L, Bernert M, Conway G D, Fischer R, Happel T, Kurzan B, McDermott R M, Scarabosio A, Suttrop W, Viezzer E, Willensdorfer M, Wolfrum E and the ASDEX Upgrade Team 2013 "Survey of the H-mode power threshold and transition physics studies in ASDEX Upgrade", *Nucl. Fusion* **53**, 113003

[22] Schirmer J "Plasma Turbulence Studies Using Correlation Doppler Reflectometry on the ASDEX Upgrade Tokamak", *PhD thesis* Technical University Munich, Germany

[23] Wagner F 2007 "A quarter-century of H-mode studies", *Plasma Phys. Control. Fusion* **49**, B1–B33

[24] Karman T 1963 "Aerodynamics", *McGraw Hill*

[25] Falkovich G 2011 "Fluid Mechanics", *Cambridge University Press*, p. 65

[26] Happel T 2010 "Design of an Optimized Doppler Reflectometer and its Application to Turbulence and Radial Electric Field Studies", *PhD thesis*, Madrid, Spain

[27] Champagne F.H. 1978 "The fine-scale structure of the turbulent velocity field", *Fluid Mechanics* **86**, p67

[28] Kraichnan R.H. 1971 "Inertial-range transfer in two- and three-dimensional turbulence", *Fluid Mechanics* **47**, p525

[29] Lechte C, Niedner S and Stroth U 2002 "Comparison of turbulence measurements and simulations of the low-temperature plasma in the torsatron TJ-K", *New J. Phys.* **4**, 34.1–34.16

[30] Stroth U, Greiner F, Lechte C, Mahdizadeh N, Rahbarnia K and Ramisch M 2004 "Study of edge turbulence in dimensionally similar laboratory plasmas", *Phys. Plasmas* **11**, 10.1063

[31] Happel T, Estrada T, Blanco E, Hidalgo C, Conway G D, Stroth U and TJ-II Team 2011 "Scale-selective turbulence reduction in H-mode plasmas in the TJ-II stellarator", *Phys. Plasmas* **18**, p.102302

[32] Hennequin P, Sabot R, Honoré C, Hoang G T, Garbet X, Truc A, Fenzi C, Quéméneur A 2004 "Scaling laws of density fluctuations at high-k on Tore Supra", *Plasma Phys. Control. Fusion* **46**, p.B121

[33] Gurchenko A D, Gusakov E Z 2010 "Evolution of ETG mode scale turbulence and anomalous electron transport in dynamic tokamak experiments", *Plasma Phys. Control. Fusion* **46**, p.B121

[34] Bretz N 1997 "Diagnostic instrumentation for microturbulence in tokamaks", *Rev. Sci. Instrum.* **68**, p.2927

[35] Ottaviani M and Manfredi G 1999 "The gyro-radius scaling of ion thermal transport from global numerical simulations of ion temperature gradient driven turbulence", *Phys. Pl.* **6**, 3267

[36] Stroth U. 2005 "Confinement, Transport and Collective Effects in Plasma Physics", *Springer-Verlag*, Berlin p.251

[37] Beer M A 1994, "Gyrofluid Models of Turbulent Transport in Tokamaks", Ph.D. thesis, Princeton University, 1995.

[38] Ribeiro T T and Scott B 2015, "Tokamak turbulence computations on closed and open magnetic flux surfaces", *Plasma Phys. Control. Fusion* **47**, 1657

[39] Mahdizadeh N, Greiner F, Happel T, Kendl A, Ramisch M, Scott B D, and Stroth U 2007, "Investigation of the parallel dynamics of drift-wave turbulence in toroidal plasmas", *Plasma Phys. Control. Fusion* **49**, 1005

[40] Ritz C P, Powers E J, Rhodes T L, Bengtson R D, Gentle K W, Lin H, Phillips P E, Wootton A J, Brower D L, Luhmann N C, Peebles W A, Schoch P M and Hickok R L 1988, "Advanced plasma fluctuation analysis techniques and their impact on fusion research", *Rev. Sci. Instrum.* **59**, 1739

[41] Birkenmeier G, Ramisch M, Fuchert G, Kohn A, Nold B, and Stroth U 2013 "Spatial structure of drift-wave turbulence and transport in a stellarator", *Plasma Phys. Control. Fusion* **55**, 015003

[42] Vershkov V, Soldatov S, Shelukhin D, and Chistiakov V 1999 "Experimental investigation of ion-temperature-gradient-like turbulence characteristics in T-10 core plasmas with toroidal and poloidal correlation reflectometry", *Nucl. Fusion* **39**, 1775

[43] Krämer-Flecken A, Soldatov S, Xu Y, Arnichand H, Hacquin S, Sabot R, and the TEXTOR team 2015 "Long-range correlation properties of quasi-coherent modes at TEXTOR", *New J. Phys.* **17**, 073007

[44] Scott B. 1997 "Three-dimensional computation of drift Alfvén turbulence", *Plasma Phys. Control. Fusion* **39**, p.1635

[45] Conner J W and Wilson H R 1994 "Survey of theories of anomalous transport", *Plasma Phys. Control. Fusion* **36**, p 719–795

[46] Scott B 2001 "Low frequency fluid drift turbulence in magnetised plasmas", *Habilitation thesis*, Düsseldorf University, Germany.

[47] Scott B. 2003 "Computation of electromagnetic turbulence and anomalous transport mechanisms in tokamak plasmas", *Plasma Phys. Control. Fusion* **45**, A385–398

[48] Horton W, Hu B, Dong J Q and Zhu P 2003 "Turbulent electron thermal transport in tokamaks", *New J. Phys.* **5**, 14

[49] Garbet X et al 2004 "Physics of transport in tokamaks", *Plasma Phys. Control. Fusion* **46**, B557–574

[50] Nordman H, Weiland J 1989 "Transport due to toroidal η_i mode turbulence in tokamaks", *Nucl. Fusion* **29**, 251

[51] Weiland J, Jarmen A B, Nordman H 1989 "Diffusive particle and heat pinch effects in toroidal plasmas", *Nucl. Fusion* **29**, 1810

[52] Conway G D, Angioni C, Dux R, Ryter F, Peeters A G, Schirmer J, Troester C, CFN Reflectometry Group and the ASDEX Upgrade Team 2006 "Observations on core turbulence transitions in ASDEX Upgrade using Doppler reflectometry", *Nucl. Fusion* **46**, S799–S808

[53] Happel T, Banon Navarro A, Conway G D, Angioni C, Bernert M, Dunne M, Fable E, Geiger B, Görler T, Jenko F, McDermott R M, Ryter F, Stroth U and the ASDEX Upgrade Team 2006 "Core turbulence behavior moving from ion-temperature-gradient regime towards trapped-electron-mode regime in the ASDEX Upgrade tokamak and comparison with gyrokinetic simulation", *Phys. Plasmas* **22**, 032503

[54] Biglari H, Diamond P H and Terry P W 1990 "Influence of sheared poloidal rotation on edge turbulence", *Phys. fluids* **2**, 1

[55] Stroth U, Manz P, Ramisch M 2005 "On the interaction of turbulence and flows in toroidal plasmas", *Plasma Phys. Control. Fusion* **53**, 024006

[56] Manz P, Ramisch M and Stroth U 2009 "Physical Mechanism behind Zonal-Flow Generation in Drift-Wave Turbulence", *Phys. Rev. Lett.* **103**, 165004

[57] Viezzer E, Pütterich T, Angioni C, Bermann A, Dux R, Fable E, McDermott R M, Stroth U and Wolfrum E 2014 "Evidence for the neoclassical nature of the radial electric field in the edge transport barrier of ASDEX Upgrade", *Nucl. Fusion* **54**, 012003

[58] McDermott R M, Angioni C, Conway G D, Dux R, Fable E, Fischer R, Pütterich T, Ryter F, Viezzer E and the ASDEX Upgrade Team 2014 "Core intrinsic rotation behaviour in ASDEX Upgrade ohmic L-mode plasmas", *Nucl. Fusion* **54**, 043009

[59] Cavedon M 2016 "The role of the radial electric field in the development of the edge transport barrier in the ASDEX Upgrade tokamak", *PhD thesis* Technical University Munich, Germany

[60] Peeters A G 2000 "Reduced charge state equations that describe pfirsch schlter impurity transport in tokamak plasma", *Phys. Plasmas* **7**, 268

[61] Kim Y B, Diamond P H, Groebner R J 1991 "Neoclassical poloidal and toroidal rotation in tokamaks", *Phys. fluids* **3**, 2050

[62] Stoschus H 2011 "Electron Transport in the Plasma Edge with Rotating Resonant Magnetic Perturbations at the TEXTOR Tokamak", *PhD thesis*, Heinrich-Heine University, Düsseldorf

[63] Neubauer O, Czymek G, Giesen B, Hüttemann P W , Sauer M, Schalt W, Schruff J 2005 "Design features of the tokamak TEXTOR", *Fus. Sci. and Techn.* **47**, 76–86

[64] Mlynek A, Schramm G, Eixenberger G, McCormick K, Zilker M, Behler K, Mlynek A, Sips K, Eheberg J and the ASDEX Upgrade Team 2010 "Design of a digital multiradian phase detector and its application in fusion plasma interferometry", *Rev. Sci. Instrum.* **81**, 039903

[65] Koslowski H R, Soltwisch H 1997 "Electron density and q profile measurements with the far-IR interferometer-polarimeter on the TEXTOR tokamak", *Fus. eng. and design* **34**, 143–150

[66] Fischer R, Wolfrum E, Schweinzer J and the ASDEX Upgrade Team 2008 "Probabilistic lithium beam data analysis", *Plasma Phys. Control. Fusion* **50**, 085009

[67] Willensdorfer M, Birkenmeier G, Fischer R, Laggner F M, Wolfrum E, Veres G, Aumayr F, Carralero D, Guimarais L, Kurzan B and the ASDEX Upgrade Team 2014 "Characterization of the Li-BES at ASDEX Upgrade", *Plasma Phys. Control. Fusion* **56**, 025008

[68] Murmann H, Götsch S, Röhr H, Salzmann H and Steuer K H 1992 "The Thomson scattering systems of the ASDEX upgrade tokamak", *Rev. Sci. Instrum.* **63**, 4941

[69] Kurzan B, Jakobi M, Murmann H and the ASDEX Upgrade Team 2004 "Signal processing of Thomson scattering data in a noisy environment in ASDEX Upgrade", *Plasma Phys. Control. Fusion* **46**, 299–317

[70] Hartfuss H J, Geist T and Hirsch M 1997 "Heterodyne methods in millimetre wave plasma diagnostics with applications to ECE, interferometry and reflectometry", *Plasma Phys. Control. Fusion* **39**, 1693–1769

[71] Rathgeber S K, Barrera L, Eich T, Fischer R, Nold B, Suttrop W, Willensdorfer M, Wolfrum E and the ASDEX Upgrade Team 2013 "Estimation of edge electron temperature profiles via forward modelling of the electron cyclotron radiation transport at ASDEX Upgrade", *Plasma Phys. Control. Fusion* **39**, 1693–1769

[72] Fonck R J, Darrow D S, Jaehnig K P 1984 "Determination of plasma-ion velocity distribution via charge-exchange recombination spectroscopy", *Phys. Rev. A* **29**, 3288

[73] Isler R C 1987 "A review of charge-exchange spectroscopy and applications to fusion plasmas", *Phys. Scripta* **35**, 650

[74] Viezzer E, Pütterich T, Dux R, McDermott R M and the ASDEX Upgrade Team 2012 "High-resolution charge-exchange measurements at ASDEX Upgrade", *Rev. Sci. Instrum.* **83**, 103501

[75] Lebschy A, McDermott R M, Geiger B, Cavedon M, Dunne M G, Dux R, Fischer R, Viezzer E and the ASDEX Upgrade Team 2015 "Indirect measurement of the poloidal rotation in the core of ASDEX Upgrade plasmas with charge exchange recombination spectroscopy", *20th EPS Conference on Plasma Physics*, Lisbon, Portugal

[76] Mc Carthy P J and the ASDEX Upgrade Team 2012 "Identification of edge-localized moments of the current density profile in a tokamak equilibrium from external magnetic measurements", *Plasma Phys. Control. Fusion* **54**, 015010

[77] Ginzburg V L 1967 "The Propagation of Electromagnetic Waves in Plasmas", *Pregamon Press, Oxford*,

[78] Hutchinson I H 1992 "One-dimensional full-wave analysis of reflectometry sensitivity and correlations", *Plasma Phys. Control. Fusion* **34**, 1225

[79] Bragg W H, Bragg W L 1913 "The Reflection of X-rays by Crystals", *Proc R. Soc. Lond* **88**, 605

[80] Piliya A D, Popov A Yu 2002 "On the application of the reciprocity theorem to calculation of a microwave radiation signal in inhomogeneous hot magnetized plasma", *Plasma Phys. Control. Fusion* **44**, 467

[81] Gusakov E Z, Leclert G, Boucherv I, Heuraux S, Hacquin S, Colin M, Bulanin V V, Petrov A V, Yakovlev B O, Clairet F and Zou X L 2002 "Small-angle scattering and spatial resolution of fluctuation reflectometry: comparison of 2D analytical theory with numerical calculations", *Plasma Phys. Control. Fusion* **44**, 1565

[82] Born M 1926 "Quantenmechanik der Stoßvorgänge", *Zeitschrift für Physik* **38**, 803

[83] Leclert G, Heuraux S, Gusakov E Z, Popov A Yu, Boucher I and Vermare L 2006 "Full-wave test of the radial correlation reflectometry analytical theory in linear and nonlinear regimes", *Plasma Phys. Control. Fusion* **48**, 1389

[84] Gusakov E Z, Yakovlev B O 2002 "Two-dimensional linear theory of radial correlation reflectometry diagnostics", *Plasma Phys. Control. Fusion* **44**, 2525

[85] Gusakov E Z and Popov A Yu 2002 "Non-linear theory of fluctuation reflectometry", *Nucl. Fusion* **44**, p.2327–2337

[86] Kosolapova N 2012 "Reconstruction of microturbulence wave number spectra from radial correlation reflectometry data", *PhD thesis*, Institute Jean Lamour, Nancy

[87] Richards M A, Scheer J A, Holm W A 2013 "Principles of Modern Radar", *Scitech publishing*

[88] Laviron C, Donne A J H, Manso M E, Sanchez J 1996 "Reflectometry techniques for density profile measurements on fusion plasmas", *Plasma Phys. Control. Fusion* **38**, 905

[89] Clairet F, Bottereau C, Chareau J M, Sabot R 2001 "Edge density profile measurements by X-mode reflectometry on Tore Supra", *Plasma Phys. Control. Fusion* **43**, 429441

[90] Hornung G 2013 "Study of plasma turbulence by ultrafast sweeping reflectometry on the Tore Supra tokamak", *PhD thesis*, Aix-Marseille Universite, Cadarache, France

[91] Nazikian R, Kramer G J and Valeo E 2001 "A tutorial on the basic principles of microwave reflectometry applied to fluctuation measurements in fusion plasmas", *Phys. Plasmas* **8**, 1840

[92] Conway G D, Poli E, Happel T and the ASDEX Upgrade Team 2010 "Interaction of Mean and Oscillating Plasma Flows Across Confinement Mode Transitions", *Plasma and Fusion Research* **5**, S2005

[93] Happel T, Conway G D, Hennequin P, Honore C, Giacalone J C, Simon P, Stroth U, Vermare L and the ASDEX Upgrade Team 2013 "The optimized steerable W-band Doppler reflectometer on ASDEX Upgrade: possibilities and issues", *Proc. 11th Intnl. Reflectometry Workshop -IRW11 (Palaiseau)*

[94] Conway G D, Schirmer J, Klenge S, Suttrop W, Holzhauer E, and the ASDEX Upgrade Team 2004 "Plasma rotation profile measurements using Doppler reflectometry", *Plasma Phys. Control. Fusion* **46**, 951

[95] Rhodes T L, Peebels W A, Doyle E J 1992 "The UCLA frequency tunable correlation reflectometer system on DIII-D", *Phys. Plasmas* **9**, 1.1464544

[96] Rhodes T L, Leboeuf J N, Sydora R D, Groebner R J, Doyle E J, McKee G R, Peebles W A, Rettig C L, Zeng L and Wang G 2002 "Comparison of turbulence measurements from DIII-D low-mode and high-performance plasmas to turbulence simulations and models", *Rev. Sci. Instrum.* **63**, 1.1143655

[97] Conway G D, Vayakis G, Fessey J A and Bartlett D V 1999 "A reflectometer for fluctuation and correlation studies on the Joint European Torus tokamak", *Rev. Sci. Instrum.* **70**, 1063

[98] Hornung G, Clairet F, Falchetto G L, Sabot R, Arnichand H and Vermare L 2013 "Turbulence correlation properties measured with ultrafast sweeping reflectometry on Tore Supra", *Plasma Phys. Control. Fusion* **55**, 125013

[99] Krämer-Flecken A and Soldatov S 2011 "On the possibility to use Correlation Reflectometry for determination of safety factor at TEXTOR", *Proc. 10th Int. Reflectometry Workshop -IRW12 (Jülich)*

[100] Prisiazhniuk D, Krämer-Flecken A, Conway G D, Happel T, Lebschy A, Manz P, Nikolaeva V, Stroth U and the ASDEX Upgrade Team 2017 "Magnetic field pitch angle and perpendicular velocity measurements from multi-point timedelay estimation of poloidal correlation reflectometry", *Plasma Phys. Control. Fusion* **59**, 025013

[101] Cripwell P, Costley A E and Fukuda T 1992 "Correlation reflectometry measurements at JET", *Proc. IAEA Tech. Com. Meeting (Abingdon, UK)*, page 168–176

[102] Conway G D, Vayakis G and Bartlett D V 1997 "Reflectometer fluctuation and correlation studies on JET", *Proc. 3th Intnl. Reflectometry Workshop -IRW3 (Madrid)*

[103] Vershkov V A, Dreval V V and Soldatov S V 1999 "A three-wave heterodyne correlation reflectometer developed in the T-10 tokamak", *Rev. Sci. Instrum.* **70**, 1700

[104] Vershkov V A, Soldatov S V, Shelukhin D A, and Chistiakov V V 2000 "Experimental investigation of ion-temperature-gradient-like turbulence characteristics in T-10 core plasmas with toroidal and poloidal correlation reflectometry", *Nucl. Fusion* **39**, 318

[105] Vershkov V A, Shelukhin D A, Soldatov S V, Urazbaev A O, Grashin S A, Eliseev L G, Melnikov A V and the T-10 team 2005 "Summary of experimental core turbulence characteristics in ohmic and electron cyclotron resonance heated discharges in T-10 tokamak plasmas", *Nucl. Fusion* **45**, S203–226

[106] Krämer-Flecken A, Dreval A, Soldatov S, Rogister A, Vershkov V and the TEXTOR-team 2004 "Turbulence studies with means of reflectometry at TEXTOR", *Nucl. Fusion* **44**, 1143–1157

[107] Krämer-Flecken A, Soldatov S, Vowinkel B and Muller P 2010 "Correlation reflectometry at TEXTOR", *Rev. Sci. Instrum.* **81**, 113502

[108] Qu H, Zhang T, Han X, Wen F, Zhang S, Kong D, Wang Y M, Gao Y, Huang C, Cai J and Gao X 2015 "Radial and poloidal correlation reflectometry on Experimental Advanced Superconducting Tokamak", *Rev. Sci. Instrum.* **86**, 083503

[109] Qu H, Zhang T, Han X, Xiang H M, Wen F, Geng K N, Wang Y M, Gao Y, Gao X and Zhang S 2016 "Multi-channel poloidal correlation reflectometry on experimental advanced superconducting tokamak", *Rev. Sci. Instrum.* **87**, 10.1063

[110] Gusakov E Z and Popov A Yu 2005 "Measurements localization in Poloidal Correlation Reflectometry", *Proc. 7th Intnl. Reflectometry Workshop -IRW7 (Garching)*

[111] Gusakov E Z and Popov A Yu 2005 "Measurements localization in Poloidal Correlation Reflectometry", *Nucl. Fusion* **46**, S289

[112] Popov A Yu 2015 "The theory of propagation and transformation of microwave beams in inhomogeneous turbulent plasma", *Habilitation thesis*, Ioffe institute, Saint-Petersburg

[113] Heike Laqua 1995 "Dynamic microwave speckles and their application to contactless velocimetry of vehicles", *Meas. Sci. Technol.* **6**, 4–10

[114] C L Holloway, R J Doviak, S A Cohn, R J Lataitis and J S Van Baelen 1997 "Cross correlations and cross spectra for spaced antenna wind profilers", *Radio Science* **32**, p967

[115] Soldatov S, Krämer-Flecken A and Zorenko O 2011 "Low noise Ka-band hopping reflectometer based on Yttrium iron garnet sources at TEXTOR", *Rev. Sci. Instrum.* **82**, 033513

[116] Orfanidis S J 2014 "Electromagnetic Waves and Antennas", *Online Book, retrieved January 2014* http://www.ece.rutgers.edu/ orfanidi/ewa/

[117] Birkenmeier G, Cavedon M, Conway G.D, Manz P, Stroth U, Fischer R, Fuchert G, Happel T, Laggner F.M, Maraschek M, Medvedeva A, Nikolaeva V, Prisiazhniuk D, Pütterich T, Ryter F, Shao L.M, Willensdorfer M, Wolfrum M, Zohm H and the ASDEX Upgrade Team 2016 "Magnetic structure and frequency scaling of limit-cycle oscillations close to L- to H-mode transitions", *Nucl. Fusion* **56**, 1

[118] Bendat J M, Kim Y C and Powers E J 1982 "Random Data: Analysis and Measurement Procedures", *New York: Wiley Interscience*

[119] G.I. Taylor 1937 "The Spectrum of Turbulence", *Proc. R. Soc. London* Ser. A **164**, 476

[120] Belmonte A, Martin B and Goldburg W.I 2000 "Experimental study of Taylor's hypothesis in a turbulent soap film", *Phys. fluids* **12**, 835

[121] Briggs B H, Phillips G J and Shinn D H 1950 "The Analysis of Observations on Spaced Receivers of the Fading of Radio Signals", *Proc. Phys. Soc. Instrum.* **63**, 106

[122] Guo-Wei He and Jin-Bai Zhang 2006 "Elliptic model for space-time correlations in turbulent shear flows", *Physical Review* **73**, 055303

[123] Xin Zhao and Guo-Wei He 2009 "Space-time correlations of fluctuating velocities in turbulent shear flows", *Physical Review* **79**, 046316

[124] GuoWei He, Guodong Jin and Yue Yang 2016 "Space-time correlations and dynamic coupling in turbulent flows", *Ann. Rev. of Fl. Mech.* **49**, p.51–71

[125] Conway G D and Elliott J A 1987 "Digital signal processing techniques for plasma dispersion curve measurements", *J. Phys. E: Sci. Instrum.* **20**, 1341

[126] Poli E, Peeters A G and Pereverzev G V 2001 "TORBEAM, a beam tracing code for electron-cyclotron waves in tokamak plasmas", *Comput. Phys. Commun.* **136**, 90

[127] Wolfgang Sachse and Yih-Hsing Pao 1977 "On the determination of phase and group velocities of dispersive waves in solids", *Journ. of Appl. Phys.* **49**, 4320

[128] Lin Y, Nazikian R, Irby J H and Marmar E S 2001 "Plasma curvature effects on microwave reflectometry fluctuation measurements", *Plasma Phys. Control. Fusion* **43**, p.L1

[129] S Soldatov, A Krämer-Flecken, C N Klimov et al 2009 "Investigation of the poloidal spectral resolution of O-mode reflectometry with two-dimensional full-wave modeling", *Fusion Engineering and Design* **84**, p.64

[130] Bulanin V V, Yafanov M V 2006 "Spatial and Spectral Resolution of the Plasma Doppler Reflectometry", *Plasma Diagn.* **32**, 41

[131] Bortolon A, Camenen Y, Karpushov A N, Duval B P, Andrebe Y, L Federspiel and Sauter O 2012 "Indirect measurement of poloidal rotation using inboard outboard asymmetry of toroidal rotation and comparison with neoclassical predictions", *Nucl. Fusion* **53**, 023002

[132] Sauter P, Pütterich T, Ryter F, Viezzer E, Wolfrum E, Conway G D, Fischer R, Kurzan B, McDermott R M, Rathgeber S K and the ASDEX Upgrade Team 2012 "L- to H-mode transitions at low density in ASDEX Upgrade", *Nucl. Fusion* **52**, 012001

[133] Ryter F, Cavedon M, Happel T, McDermott R M, Viezzer E, Conway G D, Fischer R, Kurzan B, Pütterich T, Tardini G, Willensdorfer M and the ASDEX Upgrade Team 2016 "L-H transition physics in hydrogen and deuterium: key role of the edge radial electric field and ion heat flux", *Plasma Phys. Control. Fusion* **58**, 014007

[134] Scott B.D 2005 "Free-energy conservation in local gyrofluid models", *Phys. Plasmas* **12**, 102307

[135] Conway G.D, Scott B, Schirmer J, Reich M, Kendl A and the ASDEX Upgrade Team 2005 "Direct measurement of zonal flows and geodesic acoustic mode oscillations in ASDEX Upgrade using Doppler reflectometry", *Plasma Phys. Control. Fusion* **47**, 1165–1185

[136] Simon. P, Conway G D, Stroth U, Biancalani A, Palermo F and the ASDEX Upgrade Team 2016 "Comparison of experiment and models of geodesic acoustic mode frequency and amplitude geometric scaling in ASDEX Upgrade", *Plasma Phys. Control. Fusion* **58**, 045029

[137] Simon. P 2017 "Investigation of geodesic acoustic mode flow oscillations using Doppler reflectometry in ASDEX Upgrade", *PhD thesis*, Universität Stuttgart, Germany

[138] Knapp C and Carter G 1976 "The generalized correlation method for estimation of time delay", *Acoustics, Speech Signal Proc. IEEE Trans.* **24**, 320–327

[139] Nagashima Y, Itoh K, Itoh S-I, Fujisawa A, Yagi M, Hoshino K, Shinohara K, Ejiri A, Takase Y, Ido T, Uehara K, Miura Y and the JFT-2M group 2007 "In search of zonal flows by using direct density fluctuation measurements", *Plasma Phys. Control. Fusion* **49**, 1611–1625

[140] Dunne M G, McCarthy P J, Wolfrum E, Fischer R, Fiannone L, Burckhart A and the ASDEX Upgrade Team 2012 "Measurement of neoclassically predicted edge current density at ASDEX Upgrade", *Nucl. Fusion* **52**, 123014

[141] Strumberger E, Gunter S, Schwarz E, Tichmann C and the ASDEX Upgrade Team 2008 "Fast particle losses due to NTMs and magnetic field ripple", *New J. Phys.* **10**, 023017

[142] Silva A *et al.* 1999, *Rev. Sci. Instrum.* **70**, 1072

[143] Cupido L, Graca S, Conway G.D, Manso M, Serra F and the ASDEX Upgrade Team 2006 "Frequency hopping millimeter-wave reflectometry in ASDEX upgrade", *Rev. Sci. Instrum.* **77**, 10E915

[144] da Graça S C 2009 "MHD and fast particle mode studies using fast frequency hopping reflectometers on the ASDEX Upgrade tokamak", *PhD thesis*, Universidade Técnica de Lisboa

[145] Ryter F and H mode database working group 1996 "H mode power threshold database for ITER", *Nucl. Fusion* **36**, 1217

[146] Draper N and Smith H 1998 "Applied Regression Analyses", *Wiley-Interscience*

[147] Na D.H, Na Yong-Su, Lee S.G, Angioni C, Yang S.M, Kim H.S, Hahm T.S, Ko W.H, Jhang H, Lee W.J and KSTAR Team 2016 "Observation of the intrinsic rotation in KSTAR Ohmic L-mode plasmas", *Nucl. Fusion* **56**, 036011

[148] Rice J.E, Duvall B.P, Reinke M.L, Podpaly Y.A, Bortolon A, Churchill R.M, Cziegler I, Diamond P.H, Dominguez A, Ennever P.C, Fiore C.L, Granetz R.S, Greenwald M.J, Hubbard A.E, Hughes J.W, Irby J.H, Ma Y, Marmar E.S, McDermott R.M, Porkolab M, Tsujii N and Wolfe S.M 2011 "Observations of core toroidal rotation reversals in Alcator C-Mod ohmic L-mode plasmas", *Nucl. Fusion* **51**, 083005

[149] Shimomura Y, Suzuki N, Sugihara M, Tsuda T, Odajima K, Tsunematsu T 1987 "Empirical Scaling of Energy Confinement Time of L-Mode and Optimized Mode and Some Consideration of Reactor Core Plasma in Tokamak", *Nucl. Fusion* Report JAERIM-85-080

[150] Ryter F, Angioni C, Peeters A. G, Leuterer F, Fahrbach H.U, Suttrop W and ASDEX Upgrade Team 2005 "Experimental Study of Trapped-Electron-Mode Properties in Tokamaks: Threshold and Stabilization by Collisions", *Phys. Rev. Lett.* **95**, 085001

[151] Angioni C, Camenen Y, Casson F.J, Fable E, McDermott R.M, Peeters A.G, and Rice J.E 2012 "Off-diagonal particle and toroidal momentum transport: a survey of experimental, theoretical and modelling aspects", *Nucl. Fusion* **52**, 114003

[152] Camenen Y, Peeters A.G, Angioni C, Casson F.J, Hornsby W.A, Snodin A.P, and Strintzi D 2009 "Impact of the background toroidal rotation on particle and heat turbulent transport in tokamak plasmas", *Phys. Plasmas* **16**, 012503

[153] Lebschy A, McDermott R.M, Angioni C, Geiger B, Cavedon M, Conway G.D, Dux R, Fable E, Happel T, Kappatou A, Medvedeva A, Pütterich T, Prisiazhniuk D, Ryter F, Stroth U, Viezzer E and the ASDEX Upgrade Team 2016, *43th EPS Conference on Plasma Physics*, Leuven, Belgium

[154] Lebshcy A 2017 "Characterization of the core poloidal flow at ASDEX Upgrade", *PhD thesis*, Technical University Munich, Germany

[155] Arnichand H, Sabot R, Hacquin S, Krämer-Flecken A, Garbet X, Citrin J, Bourdelle C, Hornung G, Bernardo J, Bottereau C, Clairet F, Falchetto G, Giacalone J.C and the Tore Supra team 2014 "Quasi-coherent modes and electron-driven turbulence", *Nucl. Fusion* **54**, 123017

[156] Zhong W L, Shi1 Z B, Yang Z J, Xiao G L, Yang Z C, Zhang B Y, Shi P W, Du H R, Pan X M, Zhou R B, Wan L H, Zou X L, Xu M, Duan X R, Yong Liu, Zhuang G 2016 "Experimental observation of turbulence transition and a critical gradient threshold for trapped electron mode in tokamak plasmas", *Phys. Plasmas* **23**, 060702

[157] Arnichand H, Citrin J, Hacquin S, Sabot R, Krämer-Flecken A, Garbet X, Bourdelle C, Bottereau C, Clairet F, Giacalone J.C, Guimaraes-Filho Z.O, Guirlet R, Hornung G, Lebschy A, Lotte P, Maget P, Medvedeva A, Molina D, Nikolaeva V, Prisiazhniuk D, the Tore Supra and the ASDEX Upgrade teams 2015 "Identification of trapped electron modes in frequency fluctuation spectra", *Nucl. Fusion* **58**, 014037

[158] Hacquin S, Citrin J, Arnichand H, Sabot R, Bourdelle C, Garbet X and the Tore Supra Team 2015 "Reflectometry simulations using gyrokinetic code data or study of quasi coherent modes 12th Int. Reflctometry Workshop", *Proc. 12th Int. Reflectometry Workshop -IRW12 (Jülich)*

[159] Hacquin S, Citrin J, Arnichand H, Sabot R, Bourdelle C, Garbet X, Krämer-Flecken A and Tore Supra Team 2016 "Simulation of core turbulence measurement in Tore Supra ohmic regimes", *Phys. Plasmas* **23**, 092303

[160] Banon Navarro A, Teaca B, Jenko F, Hammett G W, Happel T, and the ASDEX Upgrade Team 2014 "Applications of large eddy simulation methods to gyrokinetic turbulence", *Phys. Plasmas* **21**, 032304

[161] Sauter O, Angioni C and Lin-Liu Y R 1999 "Neoclassical conductivity and bootstrap current formulas for general axisymmetric equilibria and arbitrary collisionality regime", *Phys. Plasmas* **6**, 2834

[162] Wolf R C 2002 "Internal transport barriers in tokamak plasmas", *Plasma Phys. Control. Fusion* **45**, R1–R91

[163] Buttery R J, Gunter S, Giruzzi G, Hendert T C, Howell D, Huysmans G, La Haye R J, Maraschek M, Reimerdes H, Sauter O, Warrick C D, Wilson H R, Zohm H 2000 "Neoclassical tearing modes", *Plasma Phys. Control. Fusion* **42**, B61–B73

[164] Tudisco O, Silva A, Ceccuzzi S, D'Arcangelo O, Rocchi G, Fuenfgelder H, Bobkov V, Cavazzana R, Conway G D, Friesen J, Gonçalves B, Mancini A, Meneses L, Noterdaeme J M, Siegl G, Simonetto A, Tsujii N, Tuccillo A A, Vierle T, Zammuto A, the ASDEX Upgrade and FTU Teams 2014 "A Multichannel Reflectometer for edge Density Profile Measurements at the ICRF Antenna in ASDEX Upgrade", *AIP Conf. Proc.* **1580**, 566

[165] Aguiam D E, Silva A, Bobkov V, Carvalho P J, Carvalho P F, Cavazzana R, Conway G D, D'Arcangelo O, Fattorini L, Faugel H, Fernandes A, Fünfgelder H, Gonçalves B, Guimarais L, De Masi G, Meneses L, Noterdaeme J M, Pereira R C, Rocchi G, Santos J M, Tuccillo A A, Tudisco O 2016 "Implementation of the new multichannel X-mode edge density profile reflectometer for the ICRF antenna on ASDEX Upgrade", *Rev. Sci. Instrum.* **87**, 11E722

[166] Johnson R C 1993 "Antenna Engineering Handbook", *McGraw Hill*

[167] Manz P, Lauber P, Nikolaeva V.E, Happel T, Ryter F, Birkenmeier G, Bogomolov A, Conway G.D, Manso M.E, Maraschek M, Prisiazhniuk D, Viezzer E and the ASDEX Upgrade Team 2015 "Geodesic oscillations and the weakly coherent mode in the I-mode of ASDEX Upgrade", *Nucl. Fusion* **55**, 083004

[168] Happel T, Manz P, Ryter F, Hennequin P, Hetzenecker A, Conway G.D, Guimarais L, Honore C, Stroth U, Viezzer E and the ASDEX Upgrade Team 2016 "Turbulence intermittency linked to the weakly coherent mode in ASDEX Upgrade I-mode plasmas", *Nucl. Fusion* **56**, 064004

List of publications

Papers:

[1] Prisiazhniuk D, Krämer-Flecken A, Conway G D, Happel T, Lebschy A, Manz P, Nikolaeva V, Stroth U and the ASDEX Upgrade Team 2017 "Magnetic field pitch angle and perpendicular velocity measurements from multi-point timedelay estimation of poloidal correlation reflectometry", *Plasma Phys. Control. Fusion* **59**, 025013

[2] Prisiazhniuk D, Krämer-Flecken A, Conway G D, Stroth U and the ASDEX Upgrade Team 2017 "Turbulence correlation measurements in the L-mode of ASDEX Upgrade using poloidal correlation reflectometry", *Plasma Phys. Control. Fusion*, (in preparation)

[3] Manz P, Happel T, Ryter F, Bernert M, Birkenmeier G, Conway G D, Dunne M, Guimarais L, Hennequin P, Hetzenecker A, Honore C, Lauber P, Maraschek M, Nikolaeva V E, Prisiazhniuk D, Stroth U, Viezzer E and the ASDEX Upgrade Team 2017 "Turbulence characteristics of the I-mode confinement regime in ASDEX Upgrade" *Nucl. Fusion*, *Nucl. Fusion* **57**, 086022

[4] Lebschy A, McDermott R M, Angioni C, Geiger B, Prisiazhniuk D, Cavedon M, Conway G D, Dux R, Dunne M G, Kappatou A, Pütterich T, Stroth U, Viezzer E and the ASDEX Upgrade Team 2017 "Measurement of the complete core plasma flow across the LOC-SOC transition at the ASDEX Upgrade" *Nucl. Fusion*, (submitted)

[5] Birkenmeier G, Cavedon M, Conway G.D, Manz P, Stroth U, Fischer R, Fuchert G, Happel T, Laggner F.M, Maraschek M, Medvedeva A, Nikolaeva V, Prisiazhniuk D, Pütterich T, Ryter F, Shao L.M, Willensdorfer M, Wolfrum M, Zohm H and the ASDEX Upgrade Team 2016 "Magnetic structure and frequency scaling of limit-cycle oscillations close to L- to H-mode transitions", *Nucl. Fusion* **56**, 1

[6] Manz P, Lauber P, Nikolaeva V.E, Happel T, Ryter F, Birkenmeier G, Bogomolov A, Conway G.D, Manso M.E, Maraschek M, Prisiazhniuk D, Viezzer E and the ASDEX Upgrade Team 2015 "Geodesic oscillations and the weakly coherent mode in the I-mode of ASDEX Upgrade", *Nucl. Fusion* **55**, 083004

[7] Yashin A Yu, Bulanin V V, Gusev V K, Khromov N A, Kurskiev G S, Patrov M I, Petrov A V, Petrov M A, Petrov Yu V, Prisyazhnyuk D V, Tolstyakov S Yu 2015 "Multi-diagnostic approach to geodesic acoustic mode study", *Journal of Instrumentation* **10**, P10023

[8] Arnichand H, Citrin J, Hacquin S, Sabot R, Krämer-Flecken A, Garbet X, Bourdelle C, Bottereau C, Clairet F, Giacalone J.C, Guimaraes-Filho Z.O, Guirlet R, Hornung G, Lebschy A, Lotte P, Maget P, Medvedeva A, Molina D, Nikolaeva V, Prisiazhniuk D, the Tore Supra and the ASDEX Upgrade teams 2015 "Identification of trapped electron modes in frequency fluctuation spectra", *Nucl. Fusion* **58**, 014037

[9] Stroth U, Bañón Navarro A, Conway G D, Görler T, Happel T, Hennequin P, Lechte C, Manz P, Simon P, Biancalani A, Blanco E, Bottereau C, Clairet F, Coda S, Eibert T, Estrada T, Fasoli A, Guimarais L, Gürcan Ö, Huang Z, Jenko F, Kasparek W, Koenen C, Krämer-Flecken A, Manso M E, Medvedeva A, Molina D, Nikolaeva, Plaum V, Porte L, Prisiazhniuk D, Ribeiro T, Scott B D, Siart U, Storelli A, Vermare L, Wolf S 2015 "Experimental turbulence studies for gyro-kinetic code validation using advanced microwave diagnostics", *Nucl. Fusion* **55**, 083027

[10] Zohm H et al. 2015 "Recent ASDEX Upgrade research in support of ITER and DEMO", *Nucl. Fusion* **55**, 104010

[11] Yashin A Yu, Bulanin V V, Gusev V K, Khromov N A, Kurskiev G S, Minaev V B, Patrov M I, Petrov A V, Petrov Yu V, Prisyazhnyuk D V, Sakharov N V, Shchegolev P B, Tolstyakov S Yu, Varfolomeev V I, Wagner F 2014 "Geodesic acoustic mode observations in the Globus-M spherical tokamak", *Nucl. Fusion* **54**, 114015

[12] Bulanin V V, Wagner F, Varfolomeev V I, Gusev V K, Kurskiev G S, Minaev V B, Patrov M I, Petrov A V, Petrov Yu V, Prisyazhnyuk D V, Sakharov N V, Tolstyakov S Yu, Khromov N A, Shchegolev P B, Yashin A Yu 2014 "Observation of geodesic acoustic modes in the Globus-M spherical Tokamak", *Technical Physics Letters* **40**, 375-377

Conference proceedings:

[1] Prisiazhniuk D, Manz P, Conway G D, Krämer-Flecken A, Stroth U and the ASDEX Upgrade Team 2017, "Measurement of the turbulent phase velocity in the L-mode edge of ASDEX Upgrade and comparison with GEMR simulation", *44th EPS Conference on Plasma Physics (Belfast)*, (submitted)

[2] Krämer-Flecken A, Fuchert G, Grulke O, Hirsch M, Prisiazhniuk D, Velasco J L, Windisch T 2017, "Rotation and properties of plasma turbulence in W7-X measured by a PCR-system", *Proc. 13th Intnl. Reflectometry Workshop -IRW12 (Daejeon)*, (submitted)

[3] Freethy S J, Conway G D, Creely A, Goerler T, Happel T, Hennequin P, Pinzon J, Prisiazhniuk D, Stroth U, White A E and the ASDEX Upgrade Team 2017, "Validation studies of ion-scale GENE simulations in L-mode plasmas at ASDEX Upgrade", *44th EPS Conference on Plasma Physics (Belfast)*, (submitted)

[4] Prisiazhniuk D, Krämer-Flecken A, Conway G D, Happel T, Manz P, Angioni C, Stroth U, and the ASDEX Upgrade Team 2016, "Characterization of the turbulence during LOC-SOC transition using Poloidal Correlation Reflectometry at ASDEX Upgrade", *43th EPS Conference on Plasma Physics (Leuven)*

[5] Lebschy A, McDermott R.M, Angioni C, Geiger B, Cavedon M, Conway G.D, Dux R, Fable E, Happel T, Kappatou A, Medvedeva A, Pütterich T, Prisiazhniuk D, Ryter F, Stroth U, Viezzer E and the ASDEX Upgrade Team 2016 "Measurement of the E×B velocity across the LOC-SOC transition", *43th EPS Conference on Plasma Physics (Leuven)*

[6] Prisiazhniuk D, Krämer-Flecken A, Conway G D, Happel T, Manz P, Simon P, Stroth U, and the ASDEX Upgrade Team 2015, "Application of poloidal correlation reflectometry to study turbulence at ASDEX Upgrade", *Proc. 12th Intnl. Reflectometry Workshop -IRW12 (Jülich)*

[7] Birkenmeier G, Cavedon M, Conway G D, Manz P, Fuchert G, Laggner F.M, Happel T, Medvedeva A, Nikolaeva V, Prisiazhniuk D, Shao L M, Maraschek M, Pütterich T, Ryter F, Willensdorfer M, Wolfrum E, Stroth Y, Zohm H and the ASDEX Upgrade Team 2015, "Characterisation of Pulsations Close to The L-H Transition in AUG", *42th EPS Conference on Plasma Physics (Lisbon)*

[8] Bulanin V V, Gusev V K, Khromov N A, Kurskiev G S, Petrov A V, Petrov Yu V, Prisyazhnyuk D V, Sakharov N V, Tolstyakov S Yu, Yashin A Yu 2012, "Filament structures in the Globus-M tokamak", *39th EPS Conference & 16th Int. Congress on Plasma Physics (Stockholm)*

[9] Bulanin V V, Gusev V K, Kurskiev G S, Petrov A V, Prisyazhnyuk D V, Tolstyakov S Yu, Varfolomeev V I, Yashin A Yu 2011, "Doppler reflectometry application for filament structure study on the Globus-M tokamak", *Proc. 10th Intnl. Reflectometry Workshop - IRW11 (Padova)*

A Antenna geometry and power distribution

In figure A.1 the geometry of a single horn antenna with square aperture is shown. The dimensions of antenna in the plane perpendicular to the figure are the same. The far field radiation pattern of the horn antenna is calculated from the distribution of the field over the aperture of the antenna [116, 166]. The fundamental mode of propagation TE_{10} is considered, which has the electric field E perpendicular to the figure plane. The electric field at the aperture is given by

$$E(x,y) = E_0 \cos(\frac{\pi y}{2Y_a}) \exp\left\{ik_0 R_a \left(\sqrt{1+\frac{y^2}{R_a^2}} + \sqrt{1+\frac{x^2}{R_a^2}}\right)\right\}, \qquad \text{(A.1)}$$

where x and y are coordinates along the E- and H-planes of the antenna mouth respectively. The half length of the antenna mouth $Y_a = 23.5$ mm and the curvature radius of the horn antenna $R_a = 57.15$ mm are used. The calculated radiation intensity

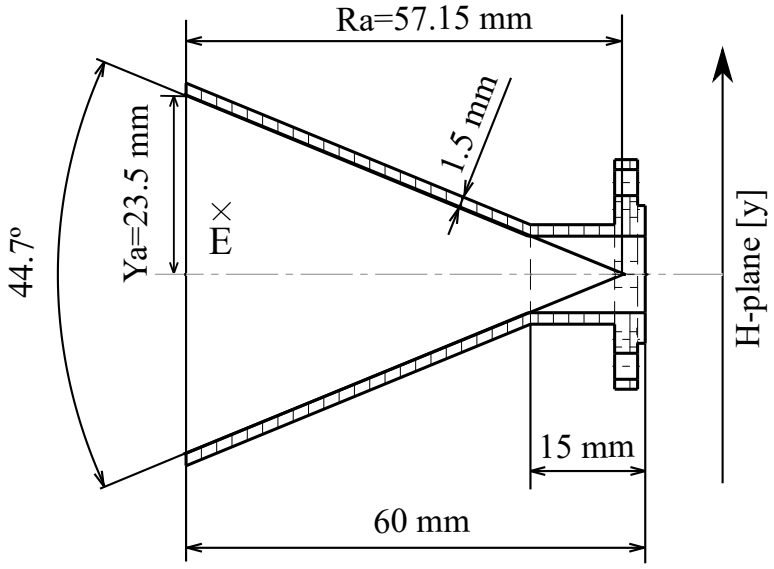

Figure A.1: Sketch of the horn antenna used at AUG.

$I(\theta) = r^2 |E|^2$ for three frequencies 24, 37 and 60 GHz in both the H and E-planes are shown in figure A.2. The half power beam width $\Delta\theta_{3dB}$ varies from 16° to 33° (see

Frequency	$\Delta\theta_{3db}$ E-plane	$\Delta\theta_{3db}$ H-plane
24 GHz	16.2°	20.2°
37 GHz	31.05°	18.9°
60 GHz	32.6°	22.06°

Table A.1: The θ_{3db} beam width for different frequencies.

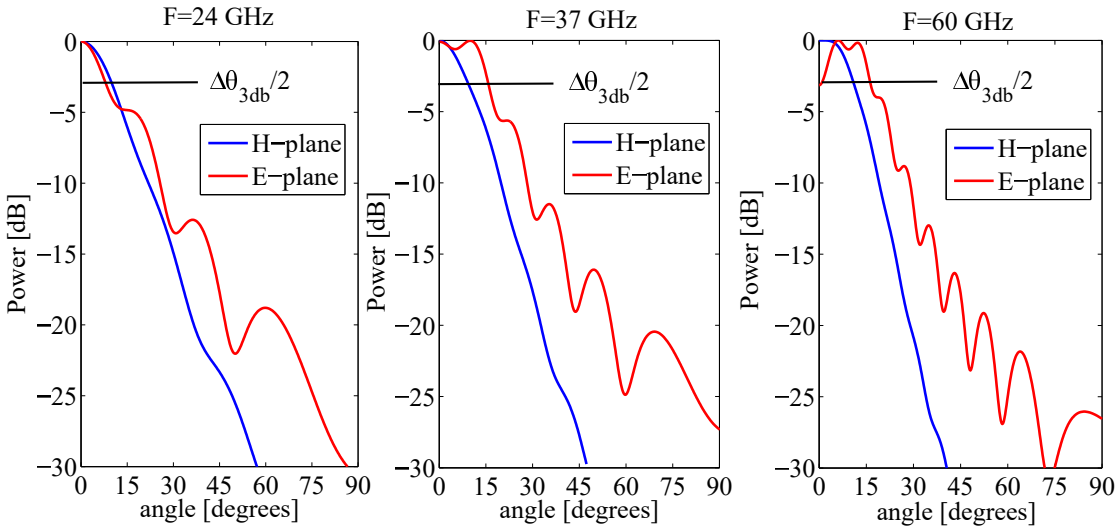

Figure A.2: 24, 37 and 60 GHz antenna radiation patterns in the H- and E- planes.

table A.1). The $\Delta\theta_{3dB}$ are different in the E- and H-planes.

B The synthetic CCF in Born approximation

In this section the effect of the finite detection volume size l_s on the measured cross-correlation function ρ_{XY}, the poloidal correlation length l_θ and the decorrelation time τ_d is investigated in case of linear regime of reflectometry. The synthetic signals for antenna B and C in the presence of turbulent density fluctuations is calculated using the Born approximation (see equation 4.11), i.e. by taking the convolution of density fluctuations $\delta n(r,\theta,t)$ with weighting functions $W_j(r,\theta)$ from equation 4.12 (here the index j stands either for B or C antenna). The density fluctuations are assumed to have a Gaussian shape in both poloidal and radial directions

$$\delta n(r,\theta,t) = \sum_{k_r}\sum_{m} \exp\left(-\frac{k_r^2 l_r^2}{8} - \frac{m^2 l_\theta^2}{8 r_c^2}\right) \cos(k_r r + \psi_{k_r}) \cos(m\theta + \omega_\theta t + \psi_m). \quad \text{(B.1)}$$

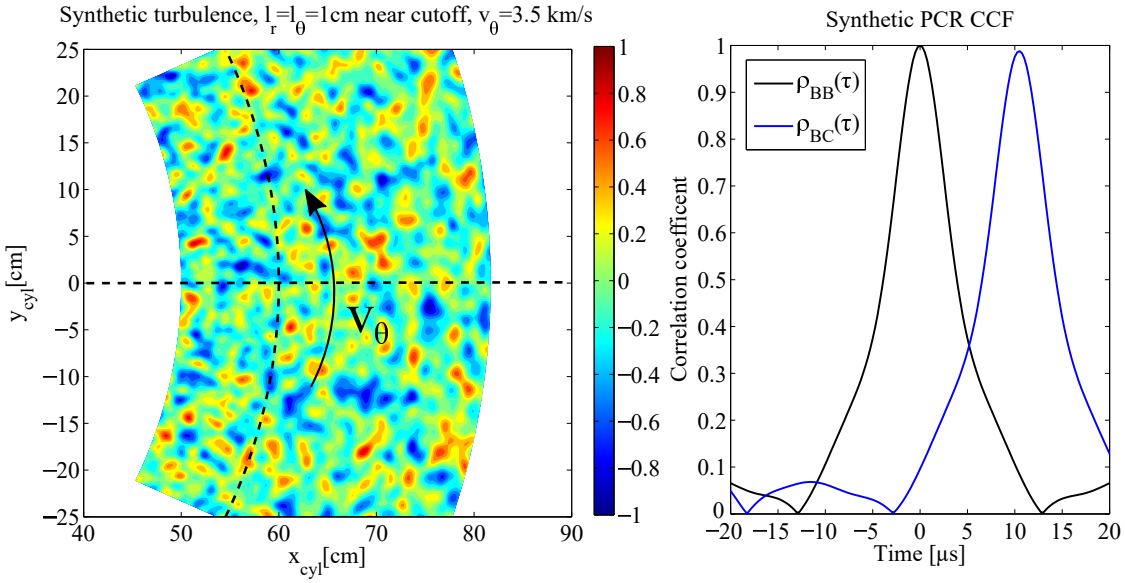

Figure B.1: a) Example of a synthetic density fluctuation snapshot used in the simulations. b) Corresponding autocorrelation (black) and cross-correlation (blue) function of calculated PCR signal.

Here l_r and l_θ are the radial and poloidal correlation lengths at the cut-off position r_c and ψ is a random phase of different turbulent modes[1]. A snapshot of density fluctuations with $l_r = l_\theta = 1$ cm in front of the cut-off layer (dotted line) is shown in figure B.1a. This density fluctuations was rotated with constant angular velocity $\omega_\theta = v_\theta / r$. It is important to note that such a model does not include the decorrelation of the turbulent eddies during the propagation (i.e. purely propagation of synthetic turbulent density fluctuations is considered only).

An example of simulated auto-correlation function (ACF) ρ_{BB} of antenna B (black) and cross-correlation function (CCF) ρ_{BC} between antenna B and C (blue) are shown in figure B.1b. The synthetic density fluctuations propagate with a velocity v_θ=3.5 km/s along the cut-off in the poloidal direction. As expected, ρ_{BC} exhibits a time delay due to the propagation. It is worthwhile to note that ρ_{BC} shows a slightly reduced peak (although the decorrelation time of the density fluctuations is infinity). This can be explained by different weighting functions $W(r, \theta)$ for antenna B and C. However, the reduction amounts to 2–3% only which is smaller than experimental decay and,

[1] In such a representation the radial correlation length of δn is independent from the radius, but the poloidal correlation length has a radial dependence. However, close to the cut-off layer r_c (which can be selected) the poloidal correlation length equals l_θ.

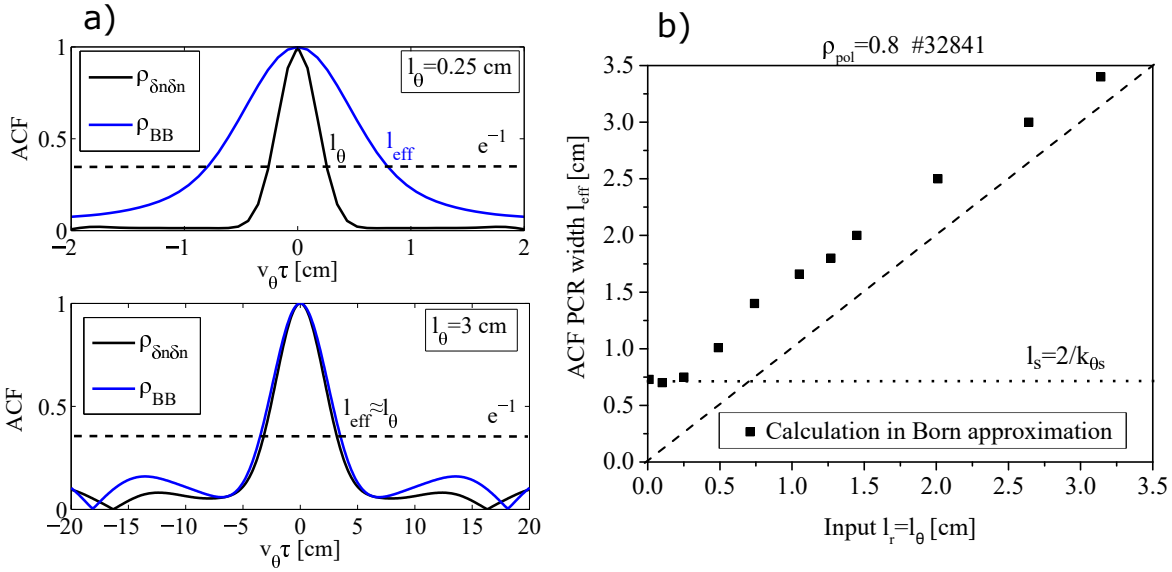

Figure B.2: a) Comparison of simulated ACF from PCR ρ_{BB} with ACF of the input density fluctuations $\rho_{\delta n \delta n}$ for two poloidal correlation lengths. Note that scale of the x-axis differs. b) The effective correlation length l_{eff} obtained by PCR versus input turbulent correlation length.

therefore, can be neglected.

The synthetic ρ_{BB} is investigated for different input correlation lengths. Figure B.2a shows a comparison of simulated ρ_{BB} by PCR (blue lines) with the ACF of the input density fluctuations $\rho_{\delta n \delta n}$ (black lines) for two poloidal correlation lengths, 0.25 and 3 cm. As in experiment the time was normalized with respect to the poloidal velocity v_θ in front of the cut-off layer (the same for both cases). The input radial correlation length is assumed to be equal to the poloidal correlation length, i.e $l_r = l_\theta$. For large correlation length $l_\theta = 3$ cm a good agreement is observed, however, for $l_\theta = 0.25$ cm the ACF of PCR is significantly wider. This can be explained by the finite detection volume size l_s of the PCR. The dependence of effective correlation length l_{eff} at e^{-1} level on the input poloidal correlation length l_θ is shown in figure B.2b. It can be concluded that:

1. When $l_\theta \gtrsim l_s/2$ a nearly linear dependence of l_{eff} with l_θ is observed.

2. When $l_\theta < l_s$ than l_{eff} is significantly larger than l_θ.

Note that the finite detection volume size l_s depends on the probing frequency and the radial position and can be roughly estimated as $l_s = 2/k_s$, where k_s is the sensitivity wavenumber at the e^{-1} level (see section 6.4.2).

Acknowledgments

It is clear that completion of an experimental thesis in three year period of time would not have been possible without the support and contribution of a large number of people. At this stage, I would like to thank everybody.

First of all, I would like to express my deepest gratitude to my academic supervisor Prof. Dr. Ulrich Stroth, who gave me an opportunity to take on this fascinating and interesting project. His great experience in plasma turbulence and the unique ability to see important details allowed me to be focused and gave me the great source of motivation to finish my thesis.

This thesis would not have been possible without the contribution of Dr. Andreas Krämer-Flecken and Dr. Garrard Conway who were my advisors. Their excellent expertise in microwave technology helped me to find solutions for many tasks. Each of their comments left a solid footprint on every page of this thesis. Besides, I would like to thank them for the time they spent reading my thesis.

I would like to thank my reflectometry and turbulence groups. Our regular meetings were an important element of the thesis. A big part of the experimental findings was a result of the discussions with Dr. Tim Happel, Dr. Peter Manz, Dr. Pascale Hennequin and Dr. Gregor Birkenmeier. My grateful thanks are also extended to Dr. Mike Dunne for his support with CLISTE equilibrium reconstruction code and to Dr. Emanuele Poli for the new version of TORBEAM code. Thanks to Alex Lebshy and Dr. Rachael McDermott for the CXRS measurements. My permanent discussions (and complains) with Anna Medvedeva were very much appreciated.

I would like to thank Johannes Friesen and Daniel Grossman for their help with installation of a new poloidal correlation reflectometry diagnostic; Gerald Sellmair, Horst Eixenberger, Andreas Hauptner for their help with electronic circuits; Helmut Blank, Roland Merkel, Karl Berhler for their support with programming and maintenance of the computers.

Our regular office discussions with Marco Cavedon, Alex Lebshy, Anna Medvedeva, Florian Lagner, Ivan Paradela Perez and Ulrike Plank are also greatly acknowledged. In particular, I would like to thank Marco Cavedon, Alex Lebshy, Peter Manz, Diogo

Aguiam and Simon Freethy for their help with improving of the content in several chapters.

I would also like to thank Dr. Viktor Bulanin, who was my supervisor during the master thesis and who brought me to the fascinating microwave world. He also gave me support for the microwave code used in this thesis for full wave simulation of microwave propagation.

I would not have finished my thesis without inspiration from the Alps mountain surrounding Bavaria. I would like to thank Oleksandra Kulyk, Dmytro Meshcheriakov, Fedor Baklanov, Anton Bogomolov, Didier Vezinet, Valentina Nikolaeva for all nice hiking tours we have made together; Serhiy Mochalskyy, Katya Zemlynaya for regular preparation of mountain skiing; Denis Kalupin, Dmitrii Moseev for cross-country skiing; Christina Kirichenko and Oleg Pronin for wonderful bike trips. I would also like to thank two of my friends from Saint Petersburg Egor Selunin and Anton Kobelev.

I am greatly thankful to my mom and dad for their support despite the big distance between us. I am very happy to have two older brothers Alexander and Ivan Prisiazhniuk. Their ability to enjoy each moment of life gave me great motivation for the work. I would like to thank everyone from my big family spreading from Orenburg in Russia across Moscow and Saint Petersburg and up to Goslar in Germany.

Finally, I would like to mention my girlfriend Oleksandra Kulyk, the person who helped me a lot with being in the right mood every day of my life. Our regular trips and nice funny moments give me great inspiration for my life and future.